# Thèse de Doctorat

présentée à

L'Université de Lille 1 – Sciences et Technologies
Insitut d'Électronique, de Microélectronique et de Nanotechnologies (IEMN)
UMR CNRS 8520

pour l'obtention du diplôme de doctorat
Discipline: Micro- et nanotechnologies, acoustique et télécommunication

par

Philipp Latzel

ayant pour titre

## High efficiency THz photomixers based on indium metallic wafer bonding

**Soutenue le 19 mai 2014 devant le jury composé de:**

| | | |
|---|---|---|
| **Président:** | Jean-Louis COUTAZ | IMEP-LAHC, Université de Savoie |
| **Directeur de thèse:** | Jean-François LAMPIN | IEMN |
| **Rapporteurs:** | Juliette MANGENEY | Lab. Pierre Aigrain, ENS Paris |
| | Roland TEISSIER | IES, Université Montpellier 2 |
| **Examinateurs:** | Frédéric VAN DIJK | III-V lab, Palaiseau |
| | Jean-Pierre VILCOT | IEMN |
| | Xavier WALLART | IEMN |
| | Emilien PEYTAVIT | IEMN |
| **Invités:** | Mohammed ZAKNOUNE | IEMN |
| | Guillaume DUCOURNAU | IEMN |

# Abstract

The THz region of the electromagnetic spectrum is still largely unexploited, mostly due to the lack of efficient, powerful, tunable, and compact sources of THz radiation. On the other hand, many applications exist in this frequency range, such as gas spectroscopy, wireless communication with high data rates, imaging, and quality control. Optoelectronic sources are promising as they are compact, widely tunable, and operate at room temperature. However, they are limited in output power due to thermal failure at high photocurrents.

In this thesis, low temperature wafer bonding employing indium is investigated as a method to transfer photomixers to substrates with higher thermal conductivity, improving the thermal properties while minimizing diffusion effects during the bonding process. Wafer bonding based on the indium–gold system is shown to be suitable for the fabrication of THz photomixers.

Due to the abundance of cheap and compact lasers and optical components available at 1.55 $\mu$m wavelength, the attention is focused on photomixers working at this telecom wavelength. As a first application of the developed bonding process, photoconductors based on Fe implanted InGaAs are investigated. However, the dark resistivity of the obtained layers is too low for use in photoconductors. In a next step, uni-traveling-carrier photodiodes transferred to silicon substrate are designed and fabricated. Highly efficient THz generation reaching 692 $\mu$W at 300 GHz has been achieved by these devices, making them ideal sources for mobile THz systems.

# Résumé

La région THz du spectre électromagnétique reste toujours peu exploité, en grande partie dû au manque de sources efficaces, puissantes, accordables, et compactes. En même temps, de nombreuses applications existent dans cette région de fréquences, comme la spectroscopie de molécules de gaz, la communication sans fil à haut débit, et l'imagerie. Les sources optoélectroniques sont prometteurs grâce à leurs petites dimensions, leur accordabilité, et leur fonctionnement à température ambiante. Cependant elles sont limitées en puissance de sortie à cause de destruction thermique à hauts photocourants.

Dans cette thèse, le collage de substrats à basse température utilisant l'In est étudié comme méthode permettant le transfert de photomélangeurs sur des substrats de conductivité thermique plus élevée, améliorant les propriétés thermiques et minimisant la diffusion pendant le collage. Il est montré que le collage basé sur le système In–Au est approprié pour la fabrication de photomélangeurs THz.

Dû à l'abondance de lasers compacts et composants optiques disponibles à 1.55 $\mu$m, l'attention est focalisée aux photomélangeurs fonctionnant à cette longueur d'onde télécom. Comme première application du processus de report développé, des photoconducteurs basés sur l'InGaAs implanté Fe sont explorés. Cependant la resistivité d'obscurité des couches obtenues reste trop faible pour leur emploi comme photoconducteurs. Ensuite des photodiodes à transport unipolaire transferées sur substrat Si sont fabriquées. Une génération THz très efficace est démontrée. A 300 GHz, une puissance de 692 $\mu$W est obtenue, faisant des photodiodes développées des sources idéales pour des systèmes mobiles THz.

# Acknowledgements

The work leading to this thesis has been carried out within the "Mitepho" Marie Curie initial training network, and has received funding from the European Union's seventh framework programme (FP7/2007-2013) under grant agreement n° 238393.

I would like to thank Jean-Louis Coutaz for having presided over the jury, and also for organizing and finding the perfect place for the first Mitepho summer school. It provided a great opportunity to get to know the other members of the network.

Juliette Mangeney and Roland Teissier have read the manuscript and written a report in a very short time, for which I am very grateful. Their corrections and suggestions helped to improve this thesis. I would also like to thank Frédéric van Dijk and Jean-Pierre Vilcot for having accepted to participate in the jury.

I would like to thank the members of the Epiphy group, especially Xavier Wallart for sharing his knowledge regarding epitaxy and semiconductors in general and for participating in the jury, and Christophe Coinon for the epitaxial growth and for help with the Hall effect measurements.

I would like to thank Mathias Vanwolleghem for the good mood and freshness he brought to the group, and for organising and installing various simulation software packages on *lorentz* and *maxwell*.

It was always a pleasure to talk to Guillaume Ducournau, and his explanations regarding his wireless data transmission experiments were much appreciated. I would also like to thank him for his help with the diode characterization, for being part of the jury, and for giving me the opportunity to continue working on the UTC photodiodes.

I would like to thank Emilien Peytavit for initiating me to clean room fabrication, showing me his processes for wafer bonding and transmission line fabrication on $SiO_2$, and for his support throughout this thesis, both regarding design and fabrication of photomixers.

Mohammed Zaknoune has started to supervise the cleanroom fabrication only in the last year of this thesis, but has had a huge impact on the results with his vast amount of experience. His always good mood and his never ending optimism made working with him very pleasant and were very helpful during the more stressful times in the cleanroom.

Discussions with Jean-François Lampin were always very enlightening. I have especially enjoyed laboratory work with him, during which I learned a lot thanks to his enormous amount of knowledge and his detailed and extremely well explained answers to just about any question.

Device fabrication in the clean room was only possible with the help of many people. In particular, I would like to thank the metallization team of André, Annie, and Guillaume for having fulfilled many special requests, and for having kept the machines up and running, especially the Indium evaporation chamber, which demanded special attention more than once. François, Marc, and Yves were very helpful with e-beam lithography, letting me use whichever e-beam writer was working and always helping out in case of problems. Pascal did the same for the substrate bonding machine and the lithography room, and Christiane for the chemistry room and the ion milling machine. Laurent performed the Fe implantation and sample annealing, while David made many FIB cuts on the bonded samples.

I am also grateful for the opportunity to work with Etienne, Damien, and Sylvie in the characterization lab, for their help with the measurements using the infrared camera and the photodiode characterization in the J-band.

Alexandre Beck initiated me to the fabrication of photodiodes, and his very clean, proper and thoughtful way of working in the clean room has been something I have been trying to imitate. The help of Antoine Pagiès during the photodiode characterization was much appreciated.

I should mention several people who have made working in the IEMN more pleasant: Ben and Thomas were always helpful, especially in the beginning when everything was new for me in Lille. It was always nice to talk to Alex Niceboy, Nadine, Hind, Chong, Cyrille, Philipp avec "e", Yann, and Alex Bontemps, and the three years would not have been the same without Lebanon's greatest basketball player, Salim, who told me so much about his country.

I have always greatly enjoyed our international dinners with the usual suspects Di, Weiwei, Karen, Ewa, Jenya, and Fabio. The mood and the food were always excellent; the Chinese and Mexican dishes in particular were exciting to taste.

I have been very lucky to share the office with someone like Fabio Pavanello. Coming from a theoretical biophysics background and not very firm in semiconductor physics, he helped me a lot to get started faster. Thanks to countless discussions regarding any type of physics, programming, and simulation, and thanks to his creativity and many ideas, he had by far the biggest influence on this thesis. Our tandem ride in San Francisco will not be forgotten, and I am proud to be able to call him a good friend.

This thesis would not have been possible without the unconditional support of my parents throughout my life. I also want to thank my uncle Georg for his continuous support, he would have been proud to have this thesis in his hands.

The most special thanks go to Anke, who in her inimitable way did everything to help me during the sometimes difficult times during the last couple of years. I want to thank her for listening when I needed to talk, for talking when I needed motivation, for going for a walk when I needed air, for letting me enjoy acrobatics and biking with her, and for supporting me in countless other ways. Without her, my life would not be the same.

# Introduction

The generation of electromagnetic waves in the THz frequency range (100 GHz – 10 THz) is still an area in development. At lower frequencies, electronic sources such as Gunn diodes, high-electron mobility transistors, and amplifiers provide high output powers. However, high frequency operation of electronic devices above 100 GHz is challenging, because the short time constants necessary require short transit times and small capacitances, which can only be achieved by smaller area devices. The fabrication and cooling of such devices becomes more and more challenging for higher frequencies. At frequencies above the so called "THz gap", optical sources perform well. However, the photon energies in the THz region are comparable with the thermal energy at room temperature, making the design of stable transitions with several meV energy difference for lasers difficult.

An interesting alternative to a purely electronic or purely optic approach is the optoelectronic generation of THz radiation. The difference frequency of two laser lines can be obtained by down-conversion in a photomixer, which can be used for THz generation by suitably choosing the laser frequencies. The most employed THz photomixers today are short lifetime photoconductors and uni-traveling-carrier photodiodes.

The wide bandwidth and spectral purity of photomixers makes them suitable for gas spectroscopy and identification, for example to identify pollutants in the atmosphere. Astronomical observatories composed of antenna arrays can benefit from photomixers as a technology enabling the low-loss distribution over large distances of the local oscillator (LO) signal via optical fiber, where conversion to the LO frequency by photomixing is performed directly at the antenna. The large bandwidth of photomixers is also interesting for wireless communication systems with very high data rates.

In view of potentially widespread application of photomixers, this thesis focuses on the development of high efficiency and high output power photomixers. The first chapter gives an introduction to photomixers and the state of the art, as well as an overview of other THz sources.

In order to obtain efficient absorption of the laser signal, a vertical photomixer configuration with a metallic mirror is chosen. Low temperature wafer bonding is used to transfer the pho-

tomixers to a high thermal conductivity substrate, to lower the operating temperature and possibly increase the output power before thermal failure. Development and optimization of the indium based bonding process and thermal characterization of the resulting bonds are subject of chapter 2.

In chapter 3, the feasibility of a vertical photoconductor working at 1.55 $\mu$m wavelength based on Fe implanted InGaAs is investigated.

Finally, two configurations for high efficiency uni-traveling-carrier photodiodes are presented in the last chapter. The first is based on a double collector design, while the second uses a semitransparent top contact for front-side illuminated photodiodes transferred to silicon substrate using the developed metallic wafer bonding process.

# Contents

**Introduction** **vii**

**1 Photomixers as optoelectronic THz sources** **1**

1.1 Optoelectronic generation of THz radiation . . . 1

1.1.1 Difference frequency in the THz range from two cw lasers . . . 2

1.1.2 Photoconductors as THz photomixers . . . 3

1.1.3 UTC photodiodes as THz photomixers . . . 11

1.1.4 Comparison of THz photomixer structures and state of the art . . . 15

1.2 Brief survey of THz generation by electronic and optical sources . . . 18

1.2.1 Frequency multipliers and electronic fundamental oscillators . . . 18

1.2.2 Vacuum electronic devices . . . 19

1.2.3 THz sources based on non-linear optics . . . 20

1.2.4 Quantum cascade lasers . . . 21

1.2.5 Molecular gas lasers . . . 22

1.3 Summary . . . 23

**Bibliography** **25**

**2 Low temperature wafer bonding based on indium metallic layer** **31**

2.1 Low temperature wafer bonding . . . 31

2.1.1 Wafer bonding process . . . 32

2.1.2 Thermocompression bonding . . . 36

2.1.3 Au–In Solid-liquid interdiffusion bonding . . . 39

2.1.4 Optical properties of the bonding layer . . . 47

2.1.5 Etching of the bonding layer . . . 49

2.2 Thermal characterization of bonded LTG-GaAs layers . . . 54

2.2.1 Sample preparation and measurement setup . . . 54

2.2.2 Measurement of the thermal conductance . . . 55

2.2.3 Simulation of the thermal conductivities . . . 58

2.2.4 Influence of the substrate conductivity on photoconductor output power 63
2.3 Summary . . . . . . . . . . . . . . . . . . . . . . . . . . . . . . . . . . . 65

**Bibliography 67**

**3 Materials for photoconductors operating at wavelengths above 1 µm 69**
3.1 Short carrier lifetime materials for photoconductors at wavelengths above 1 µm 69
3.1.1 InGaAs-based materials for THz photoconductors . . . . . . . . . . . 69
3.1.2 Other materials for THz photoconductors . . . . . . . . . . . . . . . 74
3.1.3 Summary . . . . . . . . . . . . . . . . . . . . . . . . . . . . . . . . 76
3.2 Fe-implanted InGaAs as material for a vertical photoconductor . . . . . . . . 77
3.2.1 Determination of the layer thickness . . . . . . . . . . . . . . . . . . 78
3.2.2 Determination of ion implantation parameters . . . . . . . . . . . . . 83
3.2.3 Charge carrier lifetime measurements . . . . . . . . . . . . . . . . . . 86
3.2.4 Hall effect measurements . . . . . . . . . . . . . . . . . . . . . . . . 91
3.3 Summary . . . . . . . . . . . . . . . . . . . . . . . . . . . . . . . . . . . 95

**Bibliography 97**

**4 UTC photodiodes with efficient light absorption 103**
4.1 Double collector UTC photodiodes . . . . . . . . . . . . . . . . . . . . . . 103
4.1.1 Design of double collector UTC photodiodes . . . . . . . . . . . . . . 104
4.1.2 Fabrication of double collector UTC photodiodes . . . . . . . . . . . 106
4.2 High efficiency UTC-PDs flip-chip wafer bonded to Si substrate . . . . . . . 111
4.2.1 Design of UTC photodiodes transferred to Si substrate . . . . . . . . 112
4.2.2 Device fabrication . . . . . . . . . . . . . . . . . . . . . . . . . . . . 118
4.2.3 Photodiode characterization . . . . . . . . . . . . . . . . . . . . . . . 121
4.2.4 Comparison with the state of the art and outlook . . . . . . . . . . . 132
4.3 Summary . . . . . . . . . . . . . . . . . . . . . . . . . . . . . . . . . . . 136

**Bibliography 137**

**Conclusion and perspectives 140**

# 1 Photomixers as optoelectronic THz sources

The superposition of two optical signals at different frequencies generates a beating note, which was first observed experimentally by Forrester *et al.* in 1955 from the beating of two Zeeman lines [1]. In 1993, photomixing has been revived by Brown *et al.* [2], who demonstrated photomixing in a short lifetime semiconductor using two lasers to generate the beating signal, and radiation of the signal into free space by an antenna. Another major contribution to photomixers was the invention of the uni-traveling-carrier photodiode by Ishibashi *et al.* [3] in 1997. Since then, the output power of photomixers has been improved steadily, which enabled more and more applications.

In this chapter, photomixers are presented, with photoconductors being introduced first, followed by uni-traveling-carrier photodiodes. An overview of the state of the art and a brief survey of other sources is also given.

## 1.1 Optoelectronic generation of THz radiation

THz radiation can be generated by an optoelectronic approach, where photons from one or more lasers create electron-hole pairs in a semiconductor device, which in turn create an electrical current. For continuous-wave (cw) generation of THz frequencies, two cw lasers with angular frequencies $\omega_1$ and $\omega_2$ are superposed spatially on the photomixer. A signal with the beat frequency of the two lasers, $\omega_\mathrm{B} = |\omega_1 - \omega_2|$, is then generated in the photomixer and can be radiated by a connected antenna.

The most widely used photomixers today are photoconductors, which are based on a bulk semiconductor with short charge carrier lifetime, and uni-traveling-carrier photodiodes (UTC-PD), which can be viewed as an evolution of p-i-n–diodes optimized for high speed operation. Photoconductors are usually preferred for high frequency generation above 1 THz, while UTC-PDs have higher output power at lower frequencies, which decreases more

rapidly at higher frequencies. Photoconductors are also preferred in the time domain, where THz pulses are generated by excitation of the photoconductor with a pulsed laser, and can also be used as THz detectors.

The output power of photomixers is reduced at high frequencies, because the devices do not relax to their initial state fast enough. In continuous wave (cw) operation, ideally an alternating current $I(t) = I_0(1 + \cos(\omega_\mathrm{B} t))$ is generated. At high frequencies, several effects cause a reduction of the amplitude of the alternating part of the current.

In the following, the process of THz generation in photomixers and the implications on their design is presented in more detail, and different types of photomixers are compared.

### 1.1.1 Difference frequency in the THz range from two cw lasers

For photomixing, two cw lasers with the same polarization and of angular frequencies $\omega_1$ and $\omega_2$ are superposed spatially. Assuming the direction of propagation of the lasers is along the $z$-axis, the electric field of one laser can be written as

$$\vec{E}_i(z,t) = E_i \cos(\omega_i t - k_i z + \phi_i)\vec{e}_z.$$

The energy flux density of the superposition of the two fields, assuming without loss of generality $\omega_1 > \omega_2$, is:

$$\begin{aligned} \left|\vec{S}(z,t)\right| &= \left|\vec{E}(z,t) \times \vec{H}(z,t)\right| = y_0 \vec{E}^2(z,t) = y_0 \left(\vec{E}_1(z,t) + \vec{E}_2(z,t)\right)^2 = \\ &= y_0 E_1^2 \cos^2(\omega_1 t - k_1 z + \phi_1) + \\ &\quad\; y_0 E_2^2 \cos^2(\omega_2 t - k_2 z + \phi_2) + \\ &\quad\; y_0 E_1 E_2 \cos\left((\omega_1 + \omega_2)t - (k_1 + k_2)z + \phi_1 + \phi_2\right) + \\ &\quad\; y_0 E_1 E_2 \cos\left((\omega_1 - \omega_2)t - (k_1 - k_2)z + \phi_1 - \phi_2\right) \end{aligned}$$

where $y_0 = \sqrt{\varepsilon_0/\mu_0}$ is the admittance of free space.

In photomixing experiments, the laser frequencies $\omega_1$ and $\omega_2$, as well as the sum frequency $\omega_1 + \omega_2$ are far above the cutoff frequency of the photomixer, and only the time averages of their contributions are detected. The difference frequency $\omega_\mathrm{B} = \omega_1 - \omega_2$ is chosen small enough for the photomixer to follow. The energy flux density detected by the photomixer is therefore

$$\left|\vec{S}(z,t)\right| = \frac{y_0}{2}(E_1^2 + E_2^2) + y_0 E_1 E_2 \cos\left((\omega_1 - \omega_2)t - (k_1 - k_2)z + \phi_1 - \phi_2\right). \tag{1.1}$$

The detected energy flux density is composed of a dc part, which is the sum of the laser intensities, and a modulated part, proportional to $y_0 E_1 E_2$. By writing $E_1 = \alpha E_2$, the ratio of modulated to dc intensities becomes $2\alpha/(\alpha^2 + 1)$. It reaches its maximum value of 1 for $E_1 = E_2$. As will be shown in the next sections, the dc part results in a corresponding dc current in the photomixer, which in turn contributes to the heating of the device and its destruction. The usually preferred condition for experiments is therefore $E_1 = E_2$.

The frequency $\omega_{\mathrm{B}} = \omega_1 - \omega_2$ of the modulation of the energy flux density is the difference frequency of the two lasers. If at least one of the lasers is tunable, $\omega_{\mathrm{B}}$ can be tuned also. As the laser frequencies are much higher than $\omega_{\mathrm{B}}$, only a small relative tuning range of the laser is sufficient for the photomixer's output signal to be widely tunable. In practice, the tuning range is limited by the frequency limitation of the photomixer.

The phase noise is also given by the phase stability of the lasers. In order to reduce noise and frequency shift in photomixers, dual frequency lasers have been developed, in which both laser modes share the same cavity. Noise produced from changes in the cavity length then affects both modes equally, and the noise of the beating signal is reduced.

### 1.1.2 Photoconductors as THz photomixers

The basic principle of a photoconductor is the generation of free charge carriers in a semiconductor by absorption of photons with energies above the bandgap of the semiconductor. The free charge carriers increase the electrical conductivity of the semiconductor, effectively allowing the modulation of the electrical resistance by the intensity of impinging light. By applying a bias to the photoconductor, an alternating current is created.

The first generation of free space cw THz waves up to 3.8 THz by photomixing of two lasers has been demonstrated by Brown *et al.* [4] in 1995. The photoconductor was based on low-temperature-grown GaAs (LTG-GaAs). Interdigitated electrodes and a self-complementary large band spiral antenna were patterned on the LTG-GaAs, see figure 1.1. The device is illuminated on the electrodes in the center of the spiral antenna. Due to the large permittivity of GaAs, most of the THz radiation is radiated into the substrate. A hyperhemispherical silicon lens on the backside of the substrate was used for more efficient outcoupling of the radiation into free space.

The basic design of LTG-GaAs photomixers with interdigitated electrodes, spiral antenna, and silicon lens is still used for high-frequency photomixers because of the large dark resistivity and short lifetime of LTG-GaAs, the small capacitance per device area of the

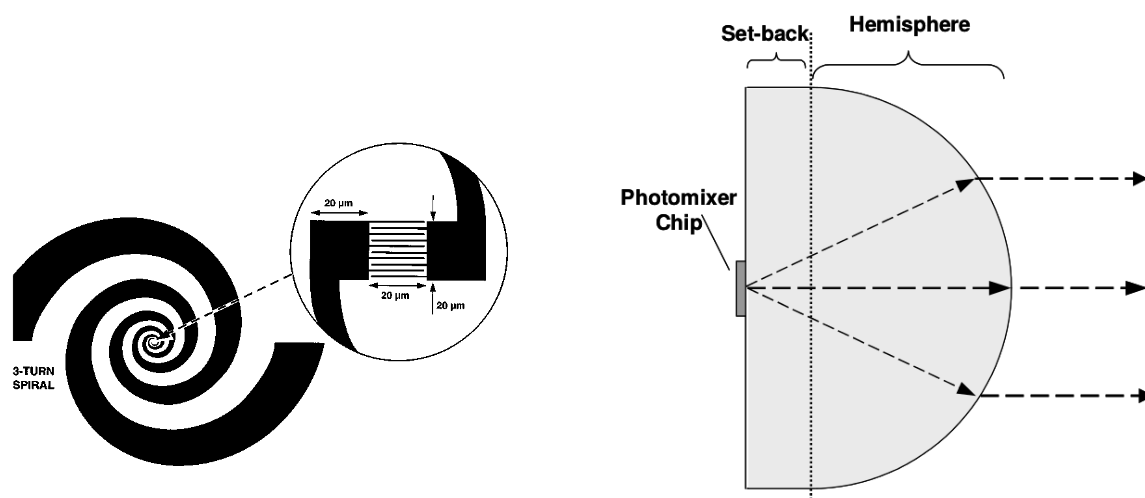


Figure 1.1: Planar photoconductor configuration. Left image: spiral antenna and interdigitated electrodes [4]. Right image: outcoupling of THz waves by a Si-lens [5].

interdigitated finger electrodes, the wideband character of antenna and silicon lens and the ease of fabrication.

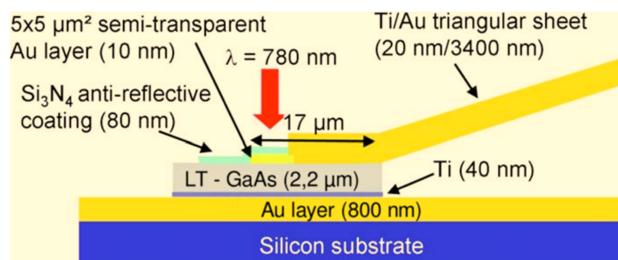


Figure 1.2: Vertical photoconductor configuration [6].

A vertical configuration of the photoconductor is shown in figure 1.2. By using a resonant Fabry-Pérot cavity for light absorption, higher responsivities and higher output powers than planar photoconductors have been obtained around 300 GHz [7, 8, 9]. The improved output power is due to better matching to the load circuit, and higher thermal conductance. However, the capacitance per device area is higher than that of interdigitated finger electrodes, and the corresponding cutoff is at lower frequencies.

#### Current generation in photoconductors

In the following, the process of current generation in photoconductors is presented in more detail. A simple model of the photoconductor (figure 1.3) is employed to simplify the

mathematical expressions without affecting the main results. The equations are only shown for electrons, however the same equations also hold for holes.

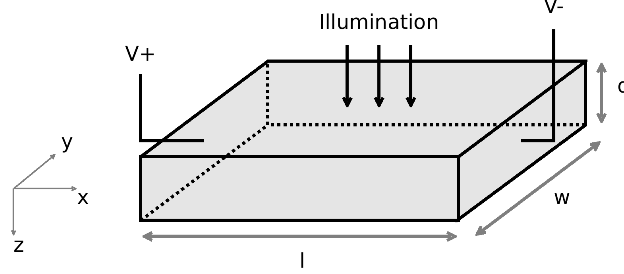


Figure 1.3: Simplified photoconductor model used in the analysis of the device.

When the beating light of two lasers with an energy flux density according to formula 1.1 impinges on such a photoconductor, a fraction $(1-R)$ enters the semiconductor, where $R$ is the reflectance.

In the semiconductor, light is absorbed according to the Beer-Lambert law, and the intensity of the light beam is given by $I(t,z) = I_0(t)(1-R)e^{-\alpha z}$, where $\alpha$ is the absorption coefficient. $I_0(t)$ is the intensity at the surface of the semiconductor $(z=0)$ before reflection, $I_0(t) = \left|\vec{S}(z=0,t)\right|$. If the incident laser power $P_{\text{opt}}(t)$ is distributed evenly over the photoconductor area $A$, then $I_0(t) = P_{\text{opt}}(t)/A$.

The density of electron-hole pairs created by light absorption is

$$\begin{aligned} g(z,t) &= -\frac{1}{h\nu}\frac{\partial I(z)}{\partial z} = \frac{1}{h\nu}\alpha I_0(t)(1-R)e^{-\alpha z} = \\ &= \frac{y_0\alpha(1-R)e^{-\alpha z}}{h\nu}\left(\frac{E_1^2+E_2^2}{2} + E_1E_2\cos\left((\omega_1-\omega_2)t + \phi_1 - \phi_2\right)\right), \end{aligned} \tag{1.2}$$

where $h\nu$ is the energy of one photon, $\nu = \omega/2\pi$ being the frequency of the laser light.

Let $n$ denote the photogenerated electron concentration in the semiconductor, that is, not including the equilibrium density without illumination, $n_{\text{dark}}$. Then $n$ is given by the following equation:

$$\dot{n}(\vec{r},t) = g(\vec{r},t) - n/\tau + 1/e\vec{\nabla}\vec{J}(\vec{r},t), \tag{1.3}$$

where $g(\vec{r},t)$ denotes the generation rate due to absorption of photons, $n/\tau$ is the reduction of free charge carriers due to trapping and recombination, with $\tau$ the lifetime in the material. $\vec{J} = \vec{J}_{\text{diff}} + \vec{J}_{\text{drift}}$ is the current density, composed of diffusion and drift currents: $\vec{J}_{\text{diff}} = -eD\vec{\nabla}n$ and $\vec{J}_{\text{drift}} = ne\vec{v} = ne\mu\vec{E}$, where $\vec{E}$ is the electric field.

The diffusion current is negligible compared to the carrier trapping due to the short lifetime of the photoconductor material in the order of $\tau \approx 1\,\mathrm{ps}$: In a standard planar photomixer, absorption of light follows the Beer-Lambert-law, and the free electron density can be approximated by $n(z) = n_0 e^{-\alpha z}$. The diffusion current then becomes $J_{\mathrm{diff}} = -D\partial^2/\partial z^2 n = D\alpha^2 n$. The typical absorption length in LTG-GaAs is $\alpha \approx 10^4/\mathrm{cm}$ [10]. The diffusion constant $D = k_{\mathrm{B}}T\mu/e \approx 26\,\mathrm{cm}^2\,\mathrm{s}^{-1}$ at room temperature, assuming a mobility of $\mu \approx 1000\,\mathrm{cm}^2\,\mathrm{V}^{-1}\,\mathrm{s}^{-1}$, which is an upper limit for the mobility in LTG-GaAs [2]. The diffusion contribution to $\dot{n}$ is then $D\Delta n \approx n \cdot 3 \cdot 10^9/\mathrm{s}$ and is much smaller than the trapping rate, $n/\tau \approx n \cdot 1 \cdot 10^{12}/\mathrm{s}$, and can be neglected.

In the absence of currents or at small electric fields, where the contribution of the drift current $J_{\mathrm{drift}}$ to $\dot{n}$ can be neglected, equation 1.3 can be solved analytically. Assuming that the generation rate due to photon absorption is of the form $g(\vec{r}, t) = A(\vec{r})\sin(\omega_{\mathrm{B}}t) + B(\vec{r})$, where the values of $A$ and $B$ depend on the illumination and the device geometry, equation 1.3 becomes

$$\dot{n}(\vec{r}, t) + n(\vec{r}, t)/\tau = A(\vec{r})\sin(\omega_{\mathrm{B}}t) + B(\vec{r}). \tag{1.4}$$

The general solution to equation 1.4 is

$$n = \frac{A\tau(\sin(\omega_{\mathrm{B}}t) - \omega_{\mathrm{B}}\tau\cos(\omega_{\mathrm{B}}t))}{1 + \omega_{\mathrm{B}}^2\tau^2} + B\tau + C_1 e^{-t/\tau}. \tag{1.5}$$

The integration constant $C_1$ appears in an exponentially declining term and depends on the initial conditions. It is omitted in the further analysis. Using the identity $\sin(\omega_{\mathrm{B}}t - \arctan(\omega_{\mathrm{B}}\tau)) = \frac{\sin(\omega_{\mathrm{B}}t) - \omega_{\mathrm{B}}\tau\cos(\omega_{\mathrm{B}}t)}{\sqrt{1+\omega_{\mathrm{B}}^2\tau^2}}$, equation 1.5 can be written as

$$n = \frac{A\tau}{\sqrt{1 + \omega_{\mathrm{B}}^2\tau^2}}\sin(\omega_{\mathrm{B}}t - \arctan(\omega_{\mathrm{B}}\tau)) + B\tau. \tag{1.6}$$

$A$ and $B$ are given from equation 1.2: $A = \frac{y_0 E_1 E_2 \alpha(1-R)e^{-\alpha z}}{h\nu}$ and $B = \frac{y_0(E_1^2+E_2^2)\alpha(1-R)e^{-\alpha z}}{2h\nu}$. The case of maximal modulation of the beating signal, $E_1 = E_2$, results in $A = B$.

The photogenerated charge carriers move towards the electrodes along the electric field lines. In general, the transit time $\tau_{\mathrm{tr}}$ of a charge carrier moving from one electrode to the other depends on the position at which the charge carrier was created due to different path lengths and field strengths. In vertical photoconductors and the simple model analyzed here, this is not the case and $\tau_{\mathrm{tr}} = l/v = l/\mu E$, assuming that the saturation velocity is not reached. For the planar interdigitated finger structure, the path of charge carriers can be approximated by a half ellipse, which is detailed for example in [5]. The ratio of lifetime and transit time

is also known as the photoconductive gain, $\gamma = \tau/\tau_{\mathrm{tr}}$. It can be thought of as the number of electrons delivered to the electrode for each photon absorbed.

The current generated by the photoconductor is given by the flux of charge carriers at the electrodes. For the simplified model, the current density is $j = nev$ and the current becomes

$$\begin{aligned} I &= \int_0^w \mathrm{d}y \int_0^d \mathrm{d}z\, j = evw \int_0^d \mathrm{d}z\, n(z) = \\ &= \frac{e\mu E w y_0 (1-R)(1-e^{-\alpha d})\tau}{h\nu} \left( (E_1^2 + E_2^2)/2 + \frac{E_1 E_2 \sin(\omega_\mathrm{B} t - \arctan(\omega_\mathrm{B}\tau))}{\sqrt{1+\omega_\mathrm{B}^2\tau^2}} \right) \end{aligned} \tag{1.7}$$

By defining $\xi = 2E_1E_2/(E_1^2 + E_2^2)$ and $\eta_{\mathrm{opt}} = (1-R)(1-e^{-\alpha d})$, and recalling $P_{\mathrm{opt}} = AI_0 = wly_0(E_1^2 + E_2^2)/2$, equation 1.7 can be written as

$$I = \frac{e}{h\nu}\gamma\eta_{\mathrm{opt}}P_{\mathrm{opt}} \left( 1 + \xi \frac{\sin(\omega_\mathrm{B} t - \arctan(\omega_\mathrm{B}\tau))}{\sqrt{1+\omega_\mathrm{B}^2\tau^2}} \right). \tag{1.8}$$

The responsivity $R$ of a photomixer is defined as $R = \overline{I}/P_{\mathrm{opt}}$. From equation 1.8, $R \leq e/h\nu$. The term $e/h\nu$ is approximately 1.25 A/W for a laser wavelength of 1.55 $\mu$m, and $\approx$ 0.63 A/W at 780 nm. Photomixers working at longer wavelengths can ideally be more efficient due to the higher number of photons impinging on the photomixer at the same optical power.

### Circuit effects

The current generated by a photoconductor in the absence of a load resistance has been calculated in the previous section (equation 1.8). However, in order to generate THz radiation, an antenna, presenting a radiation resistance $R_\mathrm{L}$, is needed. For on-wafer measurements, the load is given by the transmission line and instrument input impedances, which is typically 50 $\Omega$ and is of the same order of magnitude as broadband antennas [4]. The THz power dissipated in the load then depends also on impedance and capacitance of the photoconductor.

For the analysis of the electric circuit, it is helpful to calculate the conductance of the photoconductor. Dividing equation 1.8 by the bias voltage $V$ yields

$$G(t) = I/V = \frac{\tau}{\tau_{\mathrm{tr}}V}\frac{e}{h\nu}\eta_{\mathrm{opt}}P_{\mathrm{opt}} \left( 1 + \xi \frac{\sin(\omega_\mathrm{B} t - \arctan(\omega_\mathrm{B}\tau))}{\sqrt{1+\omega_\mathrm{B}^2\tau^2}} \right) = G_0 + G_1 \sin(\omega_\mathrm{B} t - \phi), \tag{1.9}$$

where $G_0$ is average conductance and $G_1 = G_0\xi/\sqrt{1+\omega_\mathrm{B}^2\tau^2}$ is the amplitude of the modu-

lated conductance. For small electric fields $E = V/l$, the transit time $\tau_{\rm tr} = l/v = l/\mu E$ is proportional to $1/E$ and the conductance $G$ is independent of $V$. For high bias voltages the electron velocity and therefore the conductance saturates. This saturation typically occurs at higher fields for holes than for electrons because of their lower mobility.

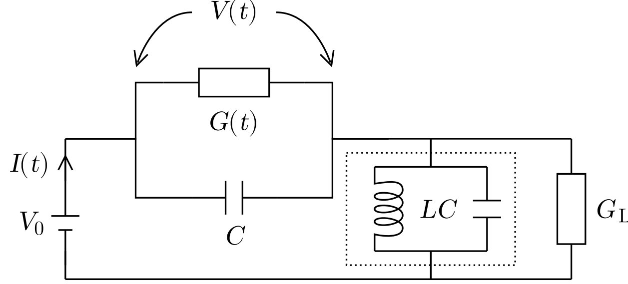


Figure 1.4: Biased photoconductor with load resistance. The resonant circuit in the dashed box filters all harmonics [11].

A circuit diagram with the biased photoconductor and a load is shown in figure 1.4. Without the $LC$ resonator, the total conductance of the circuit becomes $G_{\rm tot} = \frac{G_{\rm L}(G_0+G_1\sin(\omega_{\rm B}t)+i\omega_{\rm B}C)}{G_{\rm L}+G_0+G_1\sin(\omega_{\rm B}t)+i\omega_{\rm B}C}$ and higher harmonics are generated. To simplify the analysis, only the first order is considered, which corresponds to adding an ideal $LC$ resonator with resonance frequency $\omega_{\rm B}/2\pi$ to the circuit [11].

With the $LC$ resonator in the circuit, the voltage $V(t)$ at the photoconductor is of the form $V(t) = V_0 + V_1\sin(\omega_{\rm B}t)$ [11]. The current $I(t)$ then becomes:

$$I(t) = V(t)G(t) = (V_0+V_1\sin(\omega_{\rm B}t))(G_0+i\omega_{\rm B}C+G_1\sin(\omega_{\rm B}t)) = I_0+I_1\sin(\omega_{\rm B}t)+I_2\sin(2\omega_{\rm B}t) \tag{1.10}$$

where $I_0 = V_0(G_0+i\omega_{\rm B}C)+V_1G_1/2$ and $I_1 = V_0G_1+V_1(G_0+i\omega_{\rm B}C)$ and $I_2 = V_1G_1/2$. The ac amplitude of the voltage, $V_1$, is found from the loop equation at frequency $\omega_{\rm B}$ and is [11]:

$$V_1 = -V_0\frac{G_1}{G_0+i\omega_{\rm B}C+G_{\rm L}}.$$

The signal power (modulated at frequency $\omega_{\rm B}$) in the load is

$$\begin{aligned} P_{\rm L} &= \frac{1}{2}R_{\rm L}I_1^2 = \frac{1}{2}V_0^2\frac{G_1^2G_{\rm L}}{|G_0+G_{\rm L}+i\omega_{\rm B}C|^2} = \\ &= \frac{1}{2}R_{\rm L}V_0^2G_0^2\xi^2\frac{1}{1+\omega_{\rm B}^2\tau^2}\frac{1}{\left(1+\frac{R_{\rm L}}{R_0}\right)^2+(\omega_{\rm B}R_{\rm L}C)^2} \end{aligned} \tag{1.11}$$

Two cut-off frequencies determine the frequency dependence of the photoconductor output

power: the charge carrier lifetime $\tau$ with the 3 dB-frequency $f_\tau = 1/2\pi\tau$ and the $RC$ cutoff at $f_{\mathrm{RC}} = 1/2\pi R_{\mathrm{L}}C$. It is interesting to note that $f_{\mathrm{RC}}$ is slightly shifted to higher frequencies when $R_{\mathrm{L}}$ is not negligible compared with $R_0$. At high beating frequencies above both cutoff frequencies, the output power $P_{\mathrm{L}}$ becomes proportional to $\omega_{\mathrm{B}}^{-4}$, or 12 dB per octave.

For planar interdigitated finger GaAs photoconductors, the internal resistance $R_0$ is much larger than the antenna resistance $R_{\mathrm{L}}$, which is several 10 Ω for broadband antennas. Equation 1.11 then reduces to

$$P_{\mathrm{L}} = \frac{1}{2} R_{\mathrm{L}} I_{\mathrm{dc}}^2 \xi^2 \frac{1}{1+\omega_{\mathrm{B}}^2\tau^2} \frac{1}{1+(\omega_{\mathrm{B}} R_{\mathrm{L}} C)^2}, \tag{1.12}$$

where $I_{\mathrm{dc}} = V_0 G_0$. The frequency dependence of the output power of photoconductors with different cut-off frequencies is shown in figure 1.5.

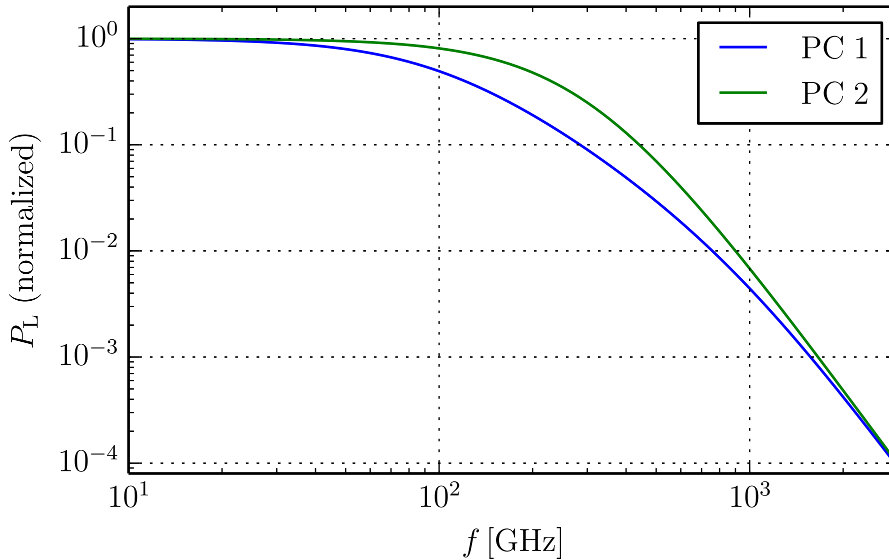


Figure 1.5: Frequency dependence of photoconductor (PC) output power according to equation 1.12. Photoconductor 1 has cut-off frequencies of $f_{\mathrm{RC}} = 100$ GHz and $f_\tau = 900$ GHz. Photoconductor 2 has both cut-off frequencies at 300 GHz. Note that in both cases $f_\tau f_{\mathrm{RC}} = (300\,\mathrm{GHz})^2$, and both photoconductors therefore have the same output power at high frequencies. At intermediate frequencies, the highest output power is obtained for $f_\tau = f_{\mathrm{RC}}$.

#### Maximization of photoconductor output power

One of the main limitations of current THz photomixers is their limited output power. It is therefore interesting to maximize the signal power $P_{\mathrm{L}}$ in equation 1.11.

From equation 1.11 it might appear that a long lifetime $\tau$ would be preferable, as the output power is proportional to $\tau^2$ at low frequencies ($G_0 \propto \tau$) and independent of $\tau$ at high frequencies. However, a long lifetime also increases the dc photocurrent, which contributes to the heating and destruction of the photoconductor. For a given frequency $\omega_\mathrm{B}$, there is an optimal lifetime $\tau$ giving the optimal trade-off between photoconductive gain, frequency roll-off, and dc current. The optimum values for the lifetime at different frequencies $\omega_\mathrm{B}$ have been calculated by Brown for planar interdigitated fingers photoconductors and are close to $\tau \approx 1/\omega_\mathrm{B}$ [5].

The output power is also dependent on the impedance matching between load and photoconductor. Maximizing $P_\mathrm{L}$ in equation 1.11 yields $G_\mathrm{L} = \sqrt{G_0^2 + \omega_\mathrm{B}^2 C^2}$, or, at low frequencies, $G_\mathrm{L} = G_0$. However, this does not take into account the power dissipated in the photoconductor. The total input power from the voltage source in figure 1.4 is [11]

$$P_\mathrm{in} = i_0 V_0 = V_0^2 \left| G_0 + i\omega_\mathrm{B} C - \frac{G_1^2}{2(G_0 + i\omega_\mathrm{B} C + G_\mathrm{L})} \right| .$$

The electrical power dissipated in the photoconductor is $P_\mathrm{in} - P_\mathrm{L}$, and the impedance matching condition which should be satisfied is to maximize the output power per dissipated power in the photoconductor, that is to maximize $\frac{P_\mathrm{L}}{P_\mathrm{in} - P_\mathrm{L}}$. When neglecting the capacitance term, this condition yields

$$G_\mathrm{L} = \sqrt{G_0^2 - \frac{G_1^2}{2}} = G_0 \sqrt{1 - \frac{\xi^2}{2\sqrt{1 + \omega_\mathrm{B}^2 \tau^2}}}.$$

At optimal modulation of the laser signal ($\xi = 1$), this becomes $G_\mathrm{L} = G_0/\sqrt{2}$ at dc, and $G_\mathrm{L} = G_0$ at high frequencies. For these two matching conditions, the electrical efficiency $\eta_\mathrm{el} = P_\mathrm{L}/P_\mathrm{in}$ at dc is $\eta_\mathrm{el} = 1/6 \approx 16.7\%$ for $G_\mathrm{L} = G_0$, and $\eta_\mathrm{el} = 3 - 2\sqrt{2} \approx 17.2\%$ for $G_\mathrm{L} = G_0/\sqrt{2}$.

Better impedance matching is the main advantage of vertical photoconductors over the conventional planar structure. The resonant absorption of light in the Fabry-Pérot cavity results in a higher density of photogenerated charge carriers. In combination with the shorter transit time $\tau_\mathrm{tr}$, this results in a higher conductance $G_0$ of the photoconductor, and a better matching to the low resistance antenna. A conductance $G_0 \approx 1/238\,\Omega$ has been measured by Peytavit *et al.* [9] for a 6 $\mu$m diameter vertical photoconductor based on a 280 nm thick LTG-GaAs layer. 350 $\mu$W output power at 305 GHz have been achieved in a broadband configuration. The conductance $G_0$ was approximately 40 times higher than that of planar photoconductors, and the output power was improved by a factor of about 100.

### 1.1.3 UTC photodiodes as THz photomixers

#### p-n and p-i-n photodiodes

A different type of semiconductor device that can be used as photodetectors are p-n-junctions. Electrons and holes photogenerated in the depletion region of a p-n-junction are accelerated towards the electrodes by the built-in potential, giving rise to a photocurrent. However, p-n-homojunctions with constant doping in the p and n regions are not very efficient photodiodes. At high doping concentrations, the depletion region in which carrier transport is efficient (drift) becomes narrow, and only a small portion of the incoming light can be absorbed in or close to the depletion region. Lower doping concentrations increase the depletion region width, but also make the formation of low resistance Ohmic contacts more difficult.

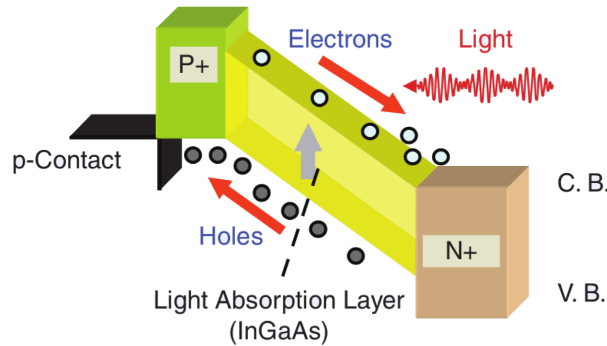


Figure 1.6: Schematic band diagram of a p-i-n photodiode [12].

The main problems of p-n-junctions for photodetectors can be overcome by adding an intrinsic layer between the p and n regions. A schematic band diagram of such a p-i-n diode is shown in figure 1.6. The p-i-n diode allows high doping concentrations for low resistance Ohmic contacts, independent from the width $w$ of the intrinsic layer. The intrinsic layer thickness $w$ is an important design parameter: it should be large enough to absorb most of the impinging radiation and to reduce the capacitance of the device, but it should be as small as possible to reduce the transit time of the charge carriers.

Minority carriers that are generated in the doped regions are subject to diffusion. Only after diffusing into the intrinsic region are they accelerated efficiently by the electric field. The doped regions of p-i-n diodes are therefore often fabricated from a material with larger bandgap than the photon energy at the intended wavelength of utilization. Light absorption and photogeneration of charge carriers then only takes place in the intrinsic region, where the charge carriers are separated efficiently by the electric field and move with drift velocity.

The frequency response of p-i-n-photodiodes has a $RC$-roll-off similar to photoconductors. Recombination of photogenerated charge carriers is negligible, and the transit time determines the frequency response instead of the life-time as is the case in photoconductors. The frequency dependence of the output power is given by [13]:

$$P_{\mathrm{RF}}(f) = P_{\mathrm{RF}}(0) \frac{1}{1 + (f/f_{\mathrm{tr}})^2} \frac{1}{1 + (2\pi f RC)^2}$$

where the transit time cut-off frequency $f_{\mathrm{tr}}$ is given by [13]

$$f_{\mathrm{tr}} \approx \frac{3.5\overline{v}}{2\pi w}$$

with $\overline{v}$ the averaged electron and hole saturation velocities:

$$\frac{1}{\overline{v}^4} = \frac{1}{2}\left(\frac{1}{v_e^4} + \frac{1}{v_h^4}\right)$$

The capacitance of a p-i-n diode with area $A$ can be approximated by $C = \varepsilon A/w$. The $RC$ cut-off frequency is then

$$f_{\mathrm{RC}} \approx \frac{w}{2\pi R \varepsilon A}$$

and is proportional to $w$, whereas the $f_{\mathrm{tr}}$ is proportional to $1/w$. In order to achieve high bandwidth devices, $w$ has to be small (several 100 nm), and the device area has to be reduced accordingly to keep the capacitance small (10 $\mu\mathrm{m}^2$ to 100 $\mu\mathrm{m}^2$). Bandwidths of 110 GHz have been reached by using an absorption layer $w = 200$ nm and a device area of 3 $\mu$m $\times$ 3 $\mu$m [14].

The main limitation of p-i-n diodes is their saturation at high injected optical powers. The slow drift velocity of holes leads to the accumulation of space charges, which screen the applied bias field. Higher drift velocities of holes could be reached by increasing the bias, but this would also lead to higher Joule losses from hole and electron currents, and to the heating and ultimately destruction of the device.

### UTC photodiodes

In order to overcome the problems associated with the slow hole drift velocity, the uni-traveling-carrier (UTC) photodiode has been developed by Ishibashi *et al.* [3]. In UTC photodiodes, two different regions are used for absorption and transport of charge carriers. The absorption region is p-doped and close to the anode of the diode, see the schematic band diagram in figure 1.7. Photogenerated holes as majority carriers then respond with the dielectric relaxation time $\tau_{\mathrm{R}} = \varepsilon/\sigma = \varepsilon/q\mu_{\mathrm{h}} p_0$, where $p_0$ is the doping concentration in

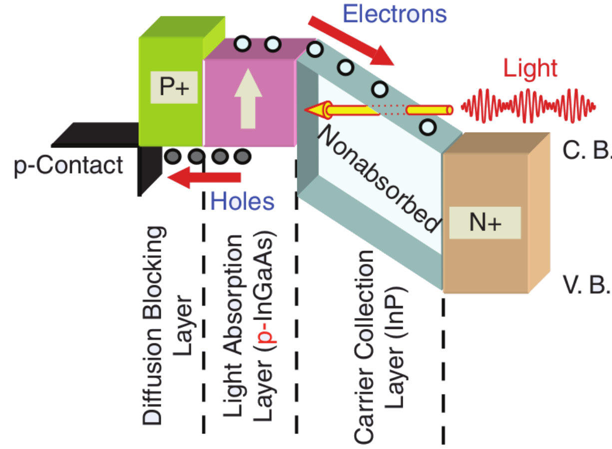


Figure 1.7: Schematic band diagram of a UTC photodiode [12].

the absorption region [3]. For $p_0 = 1 \cdot 10^{18}/\mathrm{cm}^3$, $1/\tau_\mathrm{R} \approx 30\,\mathrm{THz}$ [3], which is much faster than the electron response.

Electrons which are photogenerated in the absorption region are subject to diffusion. A diffusion blocking layer prevents them from diffusing into the anode contact. Once electrons diffuse into the transport layer, they are subject to drift transport towards the cathode.

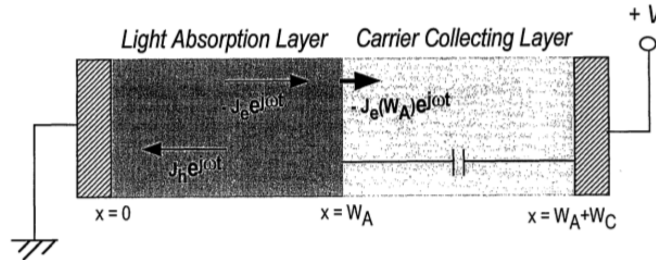


Figure 1.8: Model of a UTC photodiode [3].

Ishibashi *et al.* have analyzed the response of the UTC photodiode using the model shown in figure 1.8. The current density in a UTC photodiode is the sum of electron and hole current densities and of the displacement current, integrated over the diode thickness $W$ [3]:

$$J_\mathrm{tot} = \frac{1}{W} \int_0^W \left( J_\mathrm{e} + J_\mathrm{h} + \varepsilon \frac{\partial E}{\partial t} \right) \mathrm{d}x. \qquad (1.13)$$

When short circuited, the integrated displacement current is zero. Assuming that the hole

current in the transport layer is zero, the total current can be written as

$$J_{\mathrm{tot}} = \frac{1}{W}\int_0^{W_\mathrm{A}} (J_\mathrm{e} + J_\mathrm{h})\,\mathrm{d}x + \frac{1}{W}\int_{W_\mathrm{A}}^{W_\mathrm{C}} J_\mathrm{e}\mathrm{d}x \tag{1.14}$$

with $W_\mathrm{A}$ and $W_\mathrm{C}$ the absorption and transport (collection) layer thicknesses. The current densities $J_\mathrm{e}$ and $J_\mathrm{h}$ are calculated from the carrier dynamics and the Poisson equation:

$$\frac{\partial n}{\partial t} = G - \frac{n}{\tau} + \frac{1}{q}\frac{\partial J_\mathrm{e}}{\partial x} = G - \frac{n}{\tau} + \frac{\partial}{\partial x}\left(\mu_\mathrm{e} n(E_0 + E) + D_\mathrm{e}\frac{\partial n}{\partial x}\right) \tag{1.15}$$

$$\frac{\partial p}{\partial t} = G - \frac{p}{\tau} + \frac{1}{q}\frac{\partial J_\mathrm{h}}{\partial x} = G - \frac{p}{\tau} - \frac{\partial}{\partial x}\left(\mu_\mathrm{h}(p + p_0)E - D_\mathrm{h}\frac{\partial p}{\partial x}\right) \tag{1.16}$$

$$\frac{\partial E}{\partial x} = \frac{q}{\varepsilon}(p - n) \tag{1.17}$$

where $p$ and $n$ are the photogenerated charge carriers, $p_0$ is the background hole density in the absorption layer, $G$ is the carrier generation rate and $\tau$ is the recombination lifetime in the absorption layer, $E$ is the electric field induced by the photogenerated carriers. $E_0$ is a quasi field acting on the electrons in the absorption layer, which is included in the design of the epitaxy to improve the frequency response of the device.

It can be shown that the modulated current density generated by a UTC photodiode according to this model is [3]:

$$J_{\mathrm{ac}} = -qGW_\mathrm{A}\frac{1}{1 + i\omega_\mathrm{B}\tau_\mathrm{a}}\frac{\sin(\omega_\mathrm{B}\tau_{\mathrm{tr}}/2)}{\omega_\mathrm{B}\tau_{\mathrm{tr}}/2}\frac{1}{1 + i\omega_\mathrm{B}\tau_{\mathrm{RC}}}e^{-i\omega_\mathrm{B}\tau_{\mathrm{tr}}/2} \tag{1.18}$$

and the output power is

$$P_{\mathrm{RF}} = \frac{1}{2}R_\mathrm{L}\left|J_{\mathrm{ac}}A\right|^2, \tag{1.19}$$

where $A$ is the area of the device.

Without a quasi-field in the absorption layer, the electron transport is determined by diffusion. In that case,

$$\tau_\mathrm{a} \approx \frac{W_\mathrm{A}}{v_{\mathrm{th}}} + \frac{W_\mathrm{A}^2}{2D},$$

with $v_{\mathrm{th}} = \sqrt{2kT/\pi m^*}$ the thermionic emission velocity, approximately equal to $v_{\mathrm{th}} \approx 1 \cdot 10^7\,\mathrm{cm/s}$ in $\mathrm{In_{0.53}Ga_{0.47}As}$ [3, 15]. The response speed is limited by $v_{\mathrm{th}}$, and $\tau_\mathrm{a} \approx 2.37\,\mathrm{ps}$ for an absorption layer width $W_\mathrm{A} = 150\,\mathrm{nm}$ and assuming a mobility $\mu = 5000\,\mathrm{cm^2\,V^{-1}\,s^{-1}}$. The response speed of the diode is in this case limited by the electron diffusion in the absorption layer, with a 3 dB frequency of 67 GHz.

A quasi-field in the absorption layer can improve the frequency response by adding a drift to the electron diffusion. The quasi field is included during epitaxial growth either through a composition gradient or a doping gradient in the absorption layer. Feiginov has shown that when the drift velocity $v_\mathrm{d} > v_\mathrm{th}$, the associated time constant can be approximated by $\tau_\mathrm{a} \approx \frac{W_\mathrm{A}}{v_\mathrm{d}}$ [15]. The drift velocity can exceed $2 \cdot 10^7$ cm/s, in which case the 3 dB cutoff frequency is increased to 212 GHz for the same 150 nm wide absorption region. The faster electron transport in the absorption layer due to the built-in quasi-field is also important to reduce the carrier density and improve the response of the device in the high injection regime [3].

The electron transit time across the transport layer is given by $\tau_\mathrm{tr}$. An advantage of the UTC diodes over p-i-n diodes is that only electrons cross the transport layer, and therefore $\tau_\mathrm{tr} \approx \frac{W_\mathrm{C}}{v_\mathrm{d}}$ is shorter than for p-i-n diodes with an intrinsic region of the same width. Also, because of their high mobility, electrons reach saturation velocity already at relatively low electric field strengths ($<$ 100 kV/cm). A reverse bias in the order of $-1$ V is sufficient for efficient operation of UTC photodiodes with $\sim$100 nm wide transport layers. Moreover, velocity overshoot plays an important role in the transport layer, further decreasing $\tau_\mathrm{tr}$. The overshoot electron velocity in an InP transport layer can reach $4 \cdot 10^7$ cm/s [3].

The 3 dB-frequency associated with $\tau_\mathrm{tr}$ is determined by $\frac{\sin(x)}{x} = \sqrt{0.5}$ with $x = \omega_\mathrm{B}\tau_\mathrm{tr}/2$ (from equation 1.18). The approximate solution is $x \approx 1.39156$, and the 3 dB frequency $f_\mathrm{tr} \approx 0.4429/\tau_\mathrm{tr}$. For a transport region $W_\mathrm{C} = 200$ nm with velocity overshoot $v_\mathrm{d} = 4 \cdot 10^7$ cm/s, $f_\mathrm{tr} \approx 886$ GHz. Ballistic transport across the transport layer is also possible [16]. It is especially interesting for high-frequency operation above 1 THz, while at lower frequencies drift transport is preferable, because higher bias fields can be applied in that case [15].

### 1.1.4 Comparison of THz photomixer structures and state of the art

As THz photomixers are limited in output power, probably the most important characteristic in most applications is the maximum output power achievable. However, several other figures of merit are useful in evaluating a specific device structure and to compare various aspects between photomixers which can have been designed quite differently.

One figure of merit which is not directly related to the THz output power, is the device responsivity $R = I_\mathrm{dc}/P_\mathrm{opt}$, which shows how efficiently the laser signal is transformed into photocurrent. One advantage of the responsivity is that it is very easy to measure, as the dc photocurrent can be measured with a simple current meter and illumination by a single laser is sufficient. This is also the reason why the responsivity is usually the quantity that

is maximized practically when aligning the laser beam with respect to the photomixer in experiments.

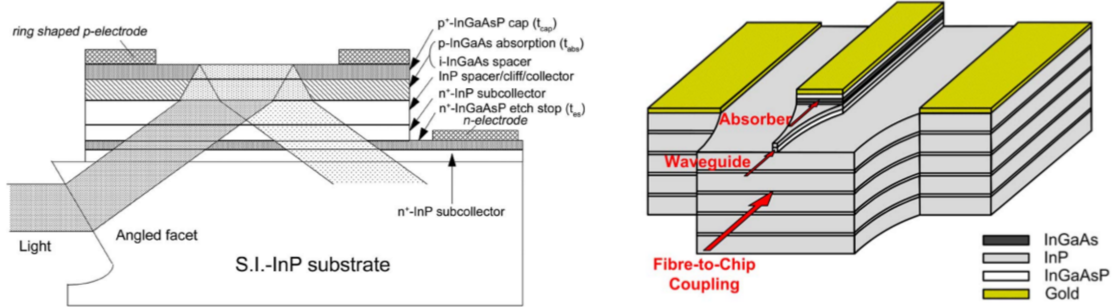


Figure 1.9: Side-illuminated UTC photodiodes. Left: Illumination through refracting facet [17]. Right: Waveguide-fed traveling-wave UTC [18].

The responsivity in planar interdigitated finger photomixers is relatively low (0.005 A/W [10]) due to the small photoconductive gain. In the vertical configuration, the responsivity can be improved thanks to efficient absorption in the LTG-GaAs layer and the higher photoconductive gain due to the lower transit time in the thin active layer. Values above 0.1 A/W have been achieved [7]. In UTC photodiodes, the responsivity is dependent on the thickness of the absorption region. A high responsivity from vertically illuminated photodiodes can be achieved with thick absorption layers, but at the cost of a lower cut-off frequency (0.55 A/W with a 600 nm absorbing region with 3 dB frequency of 30 GHz [19]). For devices working at 300 GHz and above, side illuminated devices (figure 1.9) reach responsivities above 0.2 A/W [20]. A large fraction of light is also absorbed in waveguide-fed traveling-wave structures (figure 1.9), reaching more than 0.5 A/W [18].

A figure of merit which is directly related to the output power is the total efficiency of the photomixer, $\eta_{\mathrm{tot}} = P_{\mathrm{RF}}/(P_{\mathrm{opt}} + P_{\mathrm{el}})$, where $P_{\mathrm{el}}$ is the electrical power supplied by the voltage source. As the output power of photomixers is strongly frequency dependent, the efficiency depends on the frequency as well. The optical efficiency, $\eta_{\mathrm{opt}} = P_{\mathrm{RF}}/P_{\mathrm{opt}}$ is also often specified, as it characterizes how efficiently an optical signal is down-converted into an RF signal, ignoring the electrical power which is not the limiting factor in most practical applications. The total and optical efficiencies of photomixers today are below 1% at 300 GHz, but have been improved significantly in the last years, together with the responsivity, by more efficient coupling of the optical power into the photomixer.

According to equations 1.12 and 1.19, the output power is proportional to the square of the optical power. The efficiencies $\eta_{\mathrm{tot}}$ and $\eta_{\mathrm{opt}}$ therefore tend to be higher at large laser powers. In order to compare pulsed and cw operation of photomixers, the figure of merit

| Device | $P_{RF}$ [$\mu$W] | $R$ [A/W] | $\eta_{opt}$ [%] | $\eta_{tot}$ [%] | $S$ [1/W] |
|---|---|---|---|---|---|
| UCL TW-UTC (300 GHz) [18] | > 110 | 0.31 | *0.28* | *0.13* | *0.069* |
| IEMN UTC (300 GHz) [23] | 400 | 0.046 | 0.2 | 0.18 | *0.01* |
| IEMN vertical PC (288 GHz) [24] | 650 | | 0.29 | 0.24 | 0.0128 |
| NCU NB-UTC (325 GHz) [25] | 661 | 0.015 | *0.062* | *0.06* | *0.00058* |
| NTT UTC module (300 GHz) [26] | 1200 | 0.17 | *0.51* | *0.31* | *0.022* |
| IEMN vertical PC (252 GHz) [27] | 1800 | 0.14 | *0.53* | *0.41* | *0.035* |

Table 1.1: Figures of merit of photomixers around 300 GHz. The devices in the upper part of the table are broadband, while devices in the lower part have been optimized for a narrow frequency region. Entries in italics are not given directly in the publication, but have been calculated from the data given. The broadband photoconductor is an improved version of the device presented in [9]. TW-UTC: traveling-wave UTC, NB-UTC: near-ballistic UTC, PC: photoconductor.

$S = P_{RF}/P_{opt}^2$ has been proposed [21], which avoids a strong bias towards pulsed operation as would be the case when comparing $\eta_{opt}$ due to the high peak powers of pulsed laser excitation. Due to the quadratic dependence of this figure of merit on the optical power, it is especially high for devices with efficient light coupling. Record THz figures of merit have been reported for wave-guide fed traveling wave UTC photodiodes, reaching $1\,W^{-1}$ at 110 GHz [22] and $0.003\,W^{-1}$ at 1.02 THz [18].

Listed in Table 1.1 are the figures of merit of reported photomixers working around 300 GHz. The highest reported output powers were measured using on-wafer probes. From an antenna integrated broadband device, 300 $\mu$W have been obtained by Ito *et al.*, but no information about the optical powers used was given [28].

On the high-frequency end of the photomixer spectrum, interdigitated finger photoconductors are still the preferred devices because of their low capacitance. However, the improvements of interdigitated finger photoconductors since the pioneering works by Brown have not been as impressive as the improvements of UTC-PDs, and the frequency up to which UTC-PDs reach higher output powers than photoconductors has been increased steadily. At 1 THz, several UTC designs have achieved more than 1 $\mu$W output power in a broadband configuration, ranging from 2.9 $\mu$W from a single edge-illuminated UTC PD [20] to 5 $\mu$W for traveling-wave (TW) UTCs [18]. Integration with resonant antennas produced 10.9 $\mu$W at 1.04 THz [29], and 24 $\mu$W at 914 GHz in TW UTCs [22].

However, above 2 THz, the planar LTG-GaAs photoconductor is still unsurpassed due to its low capacitance: difference frequencies up to 5 THz have been measured from cw operation

of a planar LTG-GaAs based photomixer with 0.5 fF capacitance in 1995 [30]. The highest reported frequency generated by a UTC photodiode is 2.5 THz, and has only been achieved recently [31].

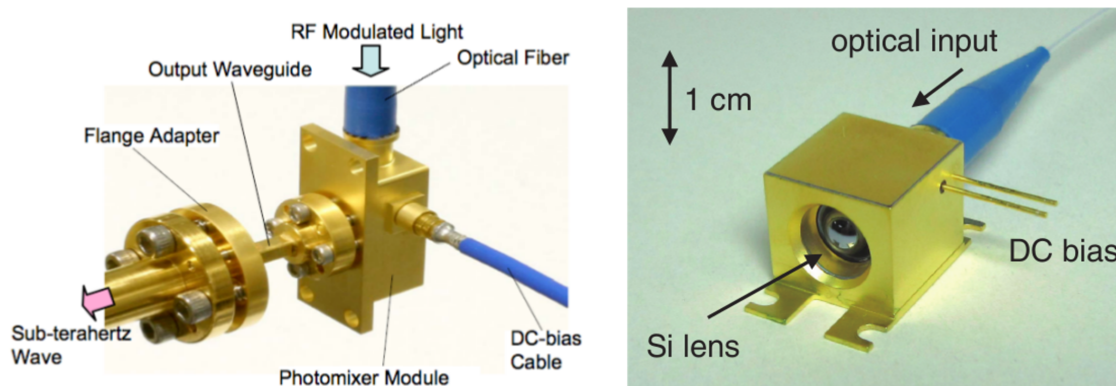


Figure 1.10: Packaged UTC photodiodes integrated with rectangular waveguide (left, [32]) and antenna and silicon lens (right, [20]).

Packaging of photomixers is necessary for applications in a less well controlled environment than the laboratory and helpful for integration in larger systems. UTC photodiodes with high output power and responsivity after packaging have mainly been reported by researchers from NTT. Waveguide-integrated devices have been presented in different frequency bands, such as the F-band (90-140 GHz) [33] and J-band (220-325 GHz, figure 1.10) [32, 26]. Antenna-integrated devices packaged with silicon lens, optical fiber, and bias connectors have also been produced by NTT, see figure 1.10 [20]. These modules show that the widespread use of UTC photodiodes in applications such as high data rate communication systems can be expected in the near future.

## 1.2 Brief survey of THz generation by electronic and optical sources

In this section, a short overview of THz sources other than photomixers is given.

### 1.2.1 Frequency multipliers and electronic fundamental oscillators

Electronic sources based on transistors work well at the lower end of the THz region (100 GHz). In order to obtain higher frequency output from electronic sources, frequency

multipliers based on Schottky diodes are employed. The frequency multipliers use the non-linear *I–V* and *C–V* characteristic of the schottky diodes to generate higher harmonics of the input frequency. A filter is used to extract one of the generated harmonics. Several such frequency multipliers can be chained together, and output powers above 1 mW in the range of 840 to 900 GHz have been reported from a source based on an electronic amplifier in the W band (75 to 110 GHz) connected to two frequency triplers [34]. A frequency multiplier chain with an additional doubler has led to the generation of frequencies in the range of 1.55 to 1.75 THz with peak output power of 100 $\mu$W, albeit at 120 K operating temperature [35]. The frequency tunability of electronic sources (10% – 15% [36]) is limited and far below that of broadband photomixers.

In recent years, the $f_{\max}$ of high electron mobility transistors (HEMT) has been increased above 1 THz [37], making amplifiers in the THz region possible. Fundamental oscillators in the range from 200 to 400 GHz based on HEMTs or heterojunction bipolar transistors (HBTs) have been reported in 2007 [38, 39].

### 1.2.2 Vacuum electronic devices

Even though the importance of vacuum electronics declined with the development of solid state electronic devices, vacuum electronic devices (VEDs) continued to evolve continuously, see figure 1.11. Today, VEDs offer high powers at frequencies extending well into the THz region (figure 1.11). The most widely used vacuum tube based devices in the THz region are backward-wave oscillators (BWOs), free electron lasers, and gyrotrons.

In backward-wave oscillators, an electron beam passes a slow-wave structure with periodic geometry, which serves as a frequency filter. The electrons generate an electromagnetic wave with group velocity opposed to the direction of propagation of the electrons. The electromagnetic wave is extracted near the cathode generating the electrons. The output frequency of BWOs is somewhat tunable ($\sim$ 30%) by changing the electron acceleration voltage. THz BWOs are useful as source for imaging applications because of their good wave-front quality and high output power for a cw source ($\sim$ 15 mW around 600 GHz) [41].

Free electron lasers (FELs) are sources based on a relativistic beam of electrons, which passes a wiggler, a periodic arrangement of magnets generating a magnetic field perpendicular to the direction of propagation of the electrons, and causing the electrons to emit synchroton radiation. It has first been used by Motz *et al.* using the Stanford linear accelerator in 1953 [42]. The synchrotron radiation of different electrons becomes coherent if the FEL is pumped by a laser or if the synchrotron radiation itself reaches sufficient intensity. Electrons

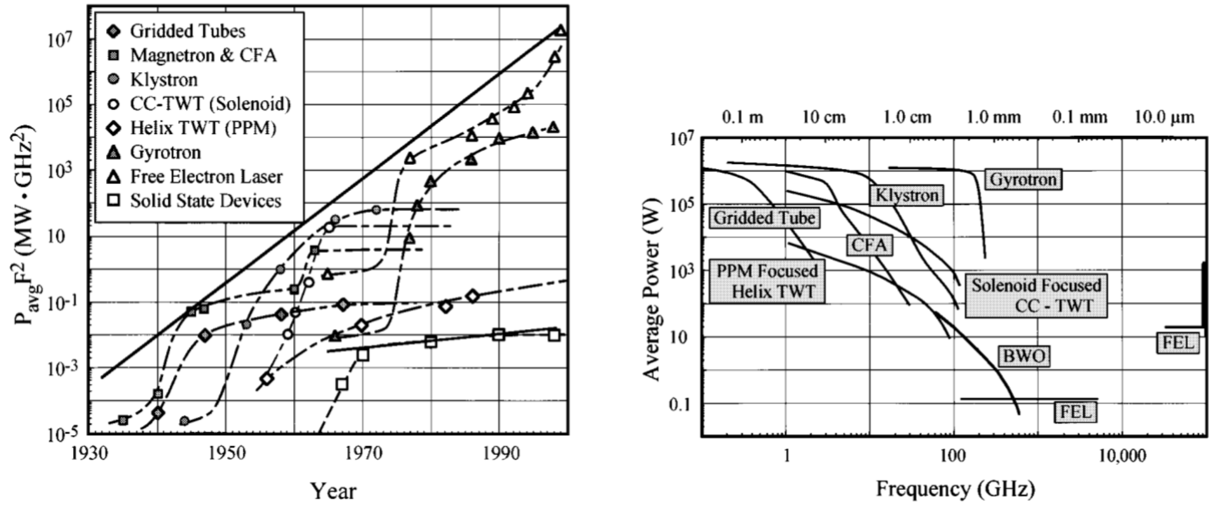


Figure 1.11: Left: Evolution of the $P_{\mathrm{RF}}f^2$ product of vacuum electronic devices (VEDs) over the years. Right: Frequency of operation of different VEDs. From [40].

then bunch together, and emit coherent laser radiation. The frequency of the FEL can be tuned by changing the energy of the electron beam, and FELs can radiate in the whole THz frequency band, and up to the X-ray region. Due to their size and cost, with an accelerator line needed to generate the relativistic electron beam, FELs are limited to the laboratory environment. The main application of THz FELs is in material characterization and spectroscopy for biomedical research [43].

Gyrotrons are capable of generating high powers of electromagnetic radiation from an electron beam in a strong magnetic field ($\sim$ 10 T), which causes gyrating movement of the electrons and associated emission of electromagnetic radiation. Focused radiation from gyrotrons can achieve power densities of $10^6\,\mathrm{W\,cm^{-2}}$, which is useful for material processing such as surface hardening, drying, and joining of dissimilar materials [44]. Gyrotrons are also used for electron spin resonance spectroscopy [45]. In the THz range, more than 1 kW cw output power at 300 GHz have been demonstrated [46], and devices operating at 1 THz with pulses of 50 $\mu$s duration and 1.5 kW power have been reported [47]. As with the other vacuum electronic devices, gyrotrons are bulky and require strong magnetic fields, which limits their application in mobile systems.

## 1.2.3 THz sources based on non-linear optics

The generation of the difference frequency of two lasers in photomixers is based on the fact that the current in the photomixer depends on the square of the electric field of the lasers

(equation 1.1). A similar nonlinearity occurs in the polarization of certain crystals. The polarization vector in the material can be approximated as [48]:

$$\vec{P} = \varepsilon_0 \chi^{(1)} \vec{E} + \varepsilon_0 \chi^{(2)} \vec{E}\vec{E} + \varepsilon_0 \chi^{(3)} \vec{E}\vec{E}\vec{E} + \dots$$

The second order non-linearity (the $\chi^{(2)}$-term) can be used for the generation of sum and difference frequencies. As the laser signal traverses the crystal, it creates a THz wave. For efficient THz generation, phase matching between THz wave and optical wave is necessary, so that the THz waves generated at different positions in the crystal interfere constructively. Also, a large second order susceptibility $\chi^{(2)}$ is preferable, which is the case in non-centrosymmetric crystals like GaAs, ZnTe, or $LiNbO_3$ [49]. Difference frequency mixing in the THz region by non-linear optical processes was first demonstrated in 1965 using a quartz crystal inside the cavity of a ruby laser [50].

In order to increase the effective length of constructive interference, crystals with periodic inversion of the $\chi^{(2)}$ nonlinear coefficient are used. The phase mismatch between optical and THz wave in one region due to imperfect matching is reduced in the subsequent inversely polarized region. This technique is also called quasi-phase-matching [51].

As the second order non-linear processes depend on the square of the electric field, pulsed lasers are usually employed for THz generation. However, continuous wave THz generation has been demonstrated by placing a nonlinear crystal in the cavity of a dual color vertical external cavity surface emitting laser. The generated frequency could be tuned between 1.85 and 1.9 THz by turning an etalon in the cavity. An output power of 2 mW has been measured at 1.9 THz with a pump power of 500 W [52].

The maximum efficiency of nonlinear optics based THz emitters is limited by the Manley-Rowe relations: No more than one THz photon can be generated per pump photon, and the energy of the THz photon is much smaller than the optical pump photon. Cascaded emitters, in which the idler photon is recycled to generate another THz photon, have been presented to potentially increase the efficiency above the Manley-Rowe limitation [53, 54].

### 1.2.4 Quantum cascade lasers

The idea of using electron transitions between subbands in two-dimensional quantum wells to achieve lasing was first proposed by Karzarinov *et al.* in 1971 [55]. The principle of operation of quantum cascade lasers (QCLs) is based on radiative intersubband transitions of electrons, which generate THz photons. One electron traversing the device undergoes several such transitions, generating several photons in the process. The careful design of the

band structure of a QCL is crucial (figure 1.12), and the permitted tolerance of the epitaxial structures is very small. The first demonstration of a quantum cascade laser (QCL) based on these ideas was in 1994 by Faist *et al.* at a frequency of 75 THz [56].

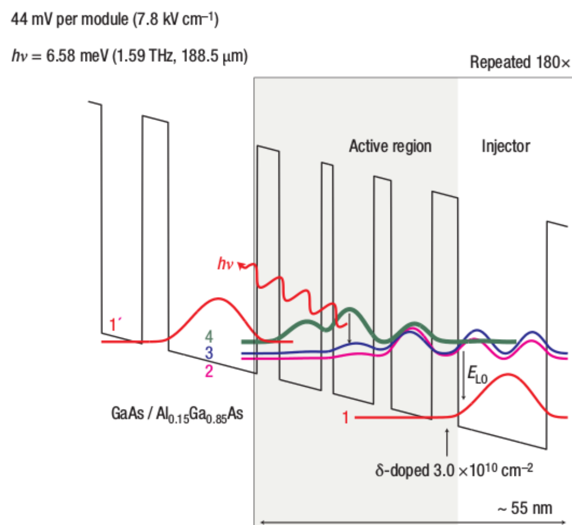


Figure 1.12: Calculated bandstructure of a quantum cascade laser. The electron in band 4 (green) emits a photon to relax into band 3 (blue), followed by nonradiative relaxation from band 3 to band 1. From [57].

The development of QCLs in the terahertz region proved difficult, with the first success by Köhler *et al.* reported in 2002 [58] at 4.4 THz. The main advantage of QCLs as THz sources is their high cw output power at high frequencies, reaching more than 10 mW at 2 THz and above. However, cooling is necessary for QCL operation, with the operation above the temperature of liquid nitrogen being a major development [59]. As the lasing frequency of QCLs is defined by the band structure, the tuning range is very limited.

### 1.2.5 Molecular gas lasers

Many gas molecules show absorption lines in their transmission spectrum in the THz frequency range. These absorption frequencies are related to energy differences of vibrational and rotational states of the molecules. In molecular lasers, a population inversion between two such states is created by optical pumping or by electric discharge. Lasing then occurs at the corresponding characteristic frequency.

The first emission from a molecular gas laser in the THz range has been observed by Crocker *et al.* in 1963 [60], when pulsed electrical discharges were used to attain population inversion in water vapor. Shortly afterwards, lasing from different molecular gases such as

HCN, $CH_3CN$, and $C_2H_5CN$ was generated [61], and cw operation of an $H_2O$ laser was reported [62]. A further major development was the optical pumping of the molecular gas laser using a $CO_2$ laser instead of the pumping by electrical discharge in 1970 [63]. More than 1 W cw power was reported in 1987 from an optically pumped laser at 2.524 THz [64].

While very high output powers can be generated by molecular gas lasers, powerful pump lasers or electrical sources are needed for their operation. Moreover, the lasing wavelength is given by the energy of the transition in the molecule, and the tuning range is very limited ($\sim$ 10 MHz [65]). Their generally large size further limits their range of applications.

## 1.3 Summary

In this chapter, THz photomixers have been presented in detail, and an overview of other sources of THz radiation has been given. While photomixers are not the sources with the highest output power in the THz region, they combine a unique fast and continuous tunability from dc up to several THz with high spectral purity determined mostly by the lasers. Photomixers are therefore the source of choice for high resolution spectroscopy in the THz range, and also as emitters for THz communication systems. Their small size, room temperature operation and lower power consumption than many other THz sources make them suitable for mobile applications and in industry.

# Bibliography


[1] A. Forrester, R. Gudmundsen, P. Johnson, *Photoelectric Mixing of Incoherent Light*, Physical Review **99**, 1691 (1955)

[2] E. R. Brown, F. W. Smith, K. A. McIntosh, *Coherent millimeter-wave generation by heterodyne conversion in low-temperature-grown GaAs photoconductors*, J. Appl. Phys. **73**, 1480 (1993)

[3] T. Ishibashi, S. Kodama, N. Shimizu, T. Furuta, *High-speed response of Uni-Traveling-Carrier photodiodes*, Jpn. J. Appl. Phys. **36**, 6263 (1997)

[4] E. R. Brown, K. A. McIntosh, K. B. Nichols, C. L. Dennis, *Photomixing up to 3.8 THz in low-temperature-grown GaAs*, Appl. Phys. Lett. **66**, 285 (1995)

[5] E. R. Brown, *Terahertz Sensing Technology, vol.1: electronic devices and advanced systems technology*, chapter THz Generation by Photomixing in Ultrafast Photoconductors (World scientific, 2003)

[6] E. Peytavit, J.-F. Lampin, F. Hindle, C. Yang, G. Mouret, *Wide-band continuous-wave terahertz source with a vertically integrated photomixer*, Appl. Phys. Lett. **95**, 161102 (2009)

[7] E. Peytavit, C. Coinon, J.-F. Lampin, *A metal-metal Fabry-Pérot cavity photoconductor for efficient GaAs terahertz photomixers*, Journal of Applied Physics **109**, 016101 (2011)

[8] E. Peytavit, C. Coinon, J.-F. Lampin, *Low-Temperature-Grown GaAs Photoconductor with High Dynamic Responsivity in the Millimeter Wave Range*, Appl. Phys. Express **4**, 104101 (2011)

[9] E. Peytavit, S. Lepilliet, F. Hindle, C. Coinon, T. Akalin, G. Ducournau, G. Mouret, J.-F. Lampin, *Milliwatt-level output power in the sub-terahertz range generated by photomixing in a GaAs photoconductor*, Appl. Phys. Lett. **99**, 223508 (2011)

[10] E. R. Brown, *A photoconductive model for superior GaAs THz photomixers*, Appl. Phys. Lett. **75**, 769 (1999)

[11] P. D. Coleman, R. C. Eden, J. N. Weaver, *Mixing and Detection of coherent light in a bulk photoconductor*, IEEE Transactions on Electron Devices 488–497 (1964)

[12] T. Nagatsuma, *Generating Millimeter and Terahertz waves*, IEEE microwave magazine **10**, 64 (2009)

[13] K. Kato, *Ultrawide-band/high-frequency Photodetectors*, IEE Transactions on microwave theory and techniques **47**, 1265 (1999)

[14] Y. Wey, K. Giboney, J. Bowers, M. Rodwell, P. Silvestre, P. Thiagarajan, G. Robinson, *110-GHz GaInAs/InP double heterostructure p-i-n photodetectors*, Journal of lightwave technology **13**, 1490 (1995)

[15] M. Feiginov, *Analysis of limitations of terahertz p-i-n uni-traveling-carrier photodiodes*, Journal of applied physics **102**, 084510 (2007)

[16] J. Shi, Y. Wu, C. WU, P. Chiu, C. Hong, *High-speed, high-responsivity, and high-power performance of near-ballistic uni-traveling-carrier photodiode at 1.55-μm wavelength*, IEEE Photonics Technology Letters **17**, 1929 (2005)

[17] Y. Muramoto, H. Fukano, T. Furuta, *A Polarization-Independent Refracting-Fact Uni-Traveling-Carrier Photodiode With High Efficiency and Large Bandwidth*, Journal of lightwave technology **24**, 3830 (2006)

[18] E. Rouvalis, C. C. Renaud, D. Moodie, M. Robertson, A. J. Seeds, *Continuous wave Terahertz Generation from Ultra-fast InP-based Photodiodes*, IEEE Transactions on microwave theory and techniques **60**, 509 (2012)

[19] M. Chtioui, A. Enard, D. Carpentier, S. Bernard, B. Rousseau, F. Lelarge, F. Pommereau, M. Achouche, *High-Performance Uni-Traveling-Carrier Photodiodes With a New Collector Design*, IEEE Photonics Technology Letters **20**, 1163 (2008)

[20] H. Ito, T. Yoshimatsu, H. Yamamoto, T. Ishibashi, *Widely Frequency Tunable Terahertz-Wave Emitter Integrating Uni-Traveling-Carrier Photodiode and Extended Bowtie Antenna*, Applied physics express **6**, 064101 (2013)

[21] E. Michael, *Travelling-wave photonic mixers for increased continuous-wave power beyond 1 THz*, Semiconductor Science and Technology **20**, S164 (2005)

[22] E. Rouvalis, C. C. Renaud, D. Moodie, M. Robertson, A. J. Seeds, *Traveling-wave Uni-traveling carrier photodiodes for continuous wave THz generation*, Optics Express **18**, 11105 (2010)

[23] F. Pavanello, *Uni-travelling carrier photodiodes and metal mesh filters based on sub-wavelength apertures for THz applications*, PhD thesis, Université Lille 1 (2013)

[24] E. Peytavit, *private communication*

[25] J-W Shi, J-M Wun, F-W Lin, J. Bowers, *Ultra-Fast (325GHz) near-ballistic uni-traveling-carrier photodiodes with high sub-THz output power under a 50 Ω load*, in *IEEE Photonics Conference* (2013)

[26] H. Song, K. Ajito, Y. Muramoto, A. Wakatsuki, T. Nagatsuma, N. Kukutsu, *Uni-Travelling-Carrier photodiode module generating 300 GHz power greater than 1 mW*, IEEE Microwave and Wireless Components Letters **22**, 363 (2012)

[27] E. Peytavit, P. Latzel, F. Pavanello, G. Ducournau, J.-F. Lampin, *CW Source Based on Photomixing With Output Power Reaching 1.8 mW at 250 GHz*, IEEE electron device letters **34**, 1277 (2013)

[28] H. Ito, T. Nagatsuma, *High-speed and high-output-power unitraveling-carrier photodiodes*, in *Active and passive optical components for WDM Communications III* (2003)

[29] H. Ito, F. Nakajima, T. Furuta, T. Ishibashi, *Continuous THz-wave generation using antenna-integrated uni-travelling-carrier photodiodes*, Semicond. Sci. Technol. **20**, S191 (2005)

[30] K. A. McIntosh, E. R. Brown, K. B. Nichols, O. B. McMahon, W. F. DiNatale, T. M. Lyszczarz, *Terahertz photomixing with diode lasers in low-temperature-grown GaAs*, Applied Physics Letters **67**, 3844 (1995)

[31] T. Ishibashi, Y. Muramoto, T. Yoshimatsu, H. Ito, *Continuous THz wave generation by photodiodes up to 2.5 THz*, in *Infrared, Millimeter, and Terahertz Waves (IRMMW-THz)* (2013)

[32] A. Wakatsuki, T. Furuta, Y. Muramoto, T. Yoshimatsu, H. Ito, *High-power and Broad-band Sub-terahertz wave generation using a J-band photomixer module with rectangular-waveguide output port*, in *IRMMW-THz 2008* (2008)

[33] H. Ito, T. Ito, Y. Muramoto, T. Furuta, T. Ishibashi, *Rectangular Waveguide Output Unitraveling-Carrier Photodiode Module for High-power Photonic Millimeter-Wave Generation in the F-band*, Journal of lightwave technology **21**, 3456 (2003)

[34] A. Maestrini, J. Ward, J. Gill, C. Lee, B. Thomas, R. Lin, G. Chattopadhyay, I. Mehdi, *A frequency-multiplied source with more than 1 mW of power across the 840-900-GHz band*, IEEE Transactions on Microwave Theory and Techniques **58**, 1925 (2010)

[35] A. Maestrini, J. Ward, H. Javadi, C. Tripon-Canseliet, J. Gill, G. Chattopadhyay, E. Schlecht, I. Mehdi, *Local oscillator chain for 1.55 to 1.75 THz with 100 μW peak power*, IEEE Microwave and Wireless Components Letters **15**, 871 (2005)

[36] G. Chattopadhyay, *Technology, Capabilities, and Performance of low power Terahertz sources*, IEEE Transactions on Terahertz Science and Technology **1**, 33 (2011)

[37] R. Lai, X. Mei, W. Deal, W. Yoshida, Y. Kim, P. Liu, J. Lee, J. Uyeda, V. Radisic, M. Lange, T. Gaier, L. Samoska, *Sub 50 nm InP HEMT Device with Fmax greater than 1THz*, in *International Electron Devices Meeting* (2007)

[38] V. Radisic, X. Mei, W. Deal, W. Yoshida, P. Liu, J. Uyeda, M. Barsky, L. Samoska, A. Fung, T. Gaier, R. Lai, *Demonstration of Submillimeter wave fundamental oscillators using 35nm InP HEMT technology*, IEEE Microwave and Wireless Components Letters **17**, 223 (2007)

[39] V. Radisic, D. Sawdai, D. Scott, W. Deal, L. Dang, D. Li, J. Chen, A. Fung, L. Samoska, T. Gaier, R. Lai, *Demonstration of a 311 GHz fundamental oscillator using InP HBT technology*, IEEE Transactions on Microwave Theory and Techniques **55**, 2329 (2007)

[40] R. Parker, R. Abrams, B. Danly, B. Levush, *Vacuum Electronics*, IEEE Transactions on Microwave Theory and Techniques **50**, 835 (2002)

[41] A. Dobroiu, M. Yamashita, Y. Ohshima, Y. Morita, C. Otani, K. Kawase, *Terahertz imaging system based on a backward-wave oscillator*, Applied Optics **43**, 5637 (2004)

[42] H. Motz, W. Thon, R. Whitehurst, *Experiments on radiation by fast electron beams*, Journal of Applied Physics **24**, 826 (1953)

[43] Y. Jeong, G. Kazakevitch, H. Cha, S. Park, P. Lee, J. Mun, *A compact THz free electron laser at KAERI*, in *IRMMW-THz 2006* (2006)

[44] A. Kumar, N. Kumar, U. Singh, V. Vyas, A. Sinha, *RF behavior and cavity design for 0.3 THz, 4 kW gyrotron for material processing application*, Infrared Physics and Technology **55**, 337 (2012)

[45] K. Felch, B. Danly, H. Jory, K. Kreischer, W. Lawson, B. Levush, R. Temkin, *Characteristics and Applications of Fast-Wave Gyrodevices*, Proceedings of the IEEE **87**, 752 (1999)

[46] T. Idehara, H. Tsuchiya, L. Agusu, H. Mori, H. Murase, T. Saito, I. Ogawa, S. Mitsudo, *The 1 THz Gyrotron at Fukui University*, in *IRMMW-THz 2007* (2007)

[47] M. Glyavin, A. Luchinin, G. Golubiatnikov, *Generation of 1.5 kW, 1THz coherent radiation from a gyrotron with a pulsed magnetic field*, Physical Review Letters **100**, 015101 (2008)

[48] J. L. Coutaz, et al., *Optoléctronique térahertz* (EDP Sciences, 2008)

[49] F. Blanchard, G. Sharma, L. Razzari, X. Ropagnol, H. Bandulet, F. Vidal, R. Morandotti, J. Kieffer, T. Ozaki, H. Tiedje, H. Haugen, M. Reid, F. Hegmann, *Generation of Intense Terahertz Radiation via Optical Methods*, IEEE Journal of selected topics in quantum electronics **17**, 5 (2011)

[50] F. Zernike, P. Berman, *Generation of far infrared as a difference frequency*, Physical Review Letters **15**, 999 (1965)

[51] K. Vodopyanov, *Ooptical THz-wave generation with periodically-inverted GaAs*, Laser and Photon. Rev. **2**, 11 (2008)

[52] M. Scheller, J. Yarborough, J. Moloney, M. Fallahi, M. Koch, S. Koch, *Room temperature continuous wave milliwatt terahertz source*, Optics Express **18**, 27112 (2010)

[53] M. Cronin-Golomb, *Cascaded nonlinear difference-frequency generation of enhanced terahertz wave production*, Optics Letters **29**, 2046 (2004)

[54] A. Stepanov, A. Mel'nikov, V. Kompanets, S. Chekalin, *Spectral Modification of Femtosecond laser pulses in the process of highly efficient generation of terahertz radiation via optical rectification*, JETP Letters **85**, 227 (2007)

[55] R. Kazarinov, R. Suris, *Possibility of the amplification of electromagnetic waves in a semiconductor with a superlattice*, Soviet Physics - Semiconductors **5**, 707 (1971)

[56] J. Faist, F. Capasso, D. Sivco, C. Sirtori, A. Hutchinson, A. Cho, *Quantum Cascade Laser*, Science **264**, 553 (1994)

[57] M. Tonouchi, *Cutting-edge terahertz technology*, nature photonics **1**, 97 (2007)

[58] R. Köhler, A. Tredicucci, F. Beltram, H. Beere, E. Linfield, A. Davies, D. Ritchie, Iotti, F. Rossi, *Terahertz semiconductor-heterostructure laser*, Nature **417**, 156 (2002)

[59] S. Kumar, B. S. Williams, S. Kohen, Q. Hu, J. L. Reno, *Continuous-wave operation of terahertz quantum-cascade lasers above liquid-nitrogen temperature*, Appl. Phys. Lett. **84**, 2494 (2004)

[60] A. Crocker, H. Gebbie, M. Kimmitt, L. Mathias, *Stimulated emission in the far infrared*, Nature **201**, 250 (1964)

[61] H. Gebbie, N. Stone, F. Findlay, *A stimulated emission source at 0.34 Millimetre wavelength*, Nature **202**, 685 (1964)

[62] W. Witterman, R. Bleekrode, *Pulsed and continuous molecular far infra-red gas laser*, Physics Letters **13**, 126 (1964)

[63] T. Chang, T. Bridges, *Laser action at 452, 496, and 541 $\mu m$ in optically pumped $CH_3F$*, Optics Communications **1**, 423 (1970)

[64] J. Farhoomand, H. Pickett, *Stable 1.25 watts CW far infrared laser radiation at the 119 μm methanol line*, International Journal of Infrared and Millimeter Waves **8**, 441 (1987)

[65] G. Dodel, *On the history of far-infrared (FIR) gas lasers: Thirty-five years of research and application*, Infrared Physics and Technology **40**, 127 (1999)

# 2 Low temperature wafer bonding based on indium metallic layer

The most widely used structures for THz photomixers are photoconductors based on LTG-GaAs and UTC photodiodes. Output powers of both types of devices are limited by thermal breakdown. The substrates used to grow the active layers, GaAs (46 W/K m) and InP (68 W/K m) do not reach the thermal conductivities of Si (148 W/K m), AlN (285 W/K m), SiC (400 W/K m), or Diamond ($\sim$1000 W/K m). Transferring active layers from their growth substrate to a high thermal conductivity substrate may improve the output powers available from photomixers. A low temperature process ($\leq$ 200 °C) is preferable to minimize stress due to differing thermal expansion coefficients of the substrates, and to avoid diffusion of metals into semiconductors as well as undesired annealing effects in photoconductors or diffusion of dopants in photodiodes.

Indium is a metal with low melting point of only 156 °C, making it an interesting candidate for metallic low temperature wafer bonding processes. In this chapter, its usability for wafer bondings as required for the fabrication of THz photomixers is investigated.

## 2.1 Low temperature wafer bonding

The active layers of most semiconductor devices, photoconductors and UTC photodiodes among them, are grown on a host substrate, for example by molecular beam epitaxy (MBE). The lattice constant of the host substrate defines which materials and which compositions can be grown without lattice mismatch. Growing lattice mismatched materials is possible within certain limits, but at the cost of more defects and higher strain in the grown layers. Therefore, the growth substrate has a big influence on the design of the layers of the device, and can not be chosen independently.

Wafer bonding allows to replace the host substrate used for epitaxial growth with a different substrate, for example a substrate with high thermal conductivity. The steps involved in

such a transfer of the epitaxial layers to a different substrate are sketched in figure 2.1. The layers required for the device are grown by MBE on a suitable substrate. An additional etch-stop layer is often needed between the substrate and the device layers. The desired new substrate and the epitaxial layers are metallized and the metal layers are brought into contact and bonded together under pressure and at elevated temperature. The original substrate is then removed by chemical wet etching. The etch stop layer protects the active layers during the etching process, and is subsequently removed in a different wet etch step.

The quality of the bonding influences the strength of the bond and the dissipation of heat from the device to the substrate. Moreover, the temperature of the bonding process must be suitable for the epitaxial layers, diffusion processes in the layers or annealing effects should usually be avoided. In some cases, the optical properties of the bonding layer are exploited for device illumination and the process must be designed accordingly [1].
In the following, low temperature indium-based wafer bonding processes and the properties of the resulting bonds are investigated.

### 2.1.1 Wafer bonding process

In order to avoid difficult wafer aligning, a smaller piece of the wafer to be transferred is bonded to a larger piece of the new host substrate: a quarter of a two inch wafer is bonded to a whole two inch wafer, and an eighth is bonded to a quarter.
The surfaces of the two wafers are cleaned in ultrasonics in an acetone bath, before being rinsed with isopropyl alcohol. The active layers are additionally deoxidized in diluted HCl (1:10 in water).
The metal layers are then deposited by evaporation or sputtering, and the substrates are brought into contact immediately after metallization in order to minimize oxidation. The smaller wafer is placed centered on the bigger wafer, with no further alignment. The two wafers are loaded into the bonding machine and the bonding process is started instantly.

A commercial bonding machine of type Süss SB6e is used for the wafer bonding. The bonding process is largely automated, and defined by recipes created using the included software. A recipe consists of several steps in which chamber pressure, bonding pressure, temperature and temperature ramps can be defined.

Before introduction of the bottom plate into the bonding machine, the wafers are placed on top of it, followed by a 500 $\mu$m thick graphite sheet and a 3 in diameter borosilicate disc. The borosilicate disc is about 4 mm thick and improves the pressure homogeneity on the bonded samples. The soft graphite sheet protects the edges and especially corners of the

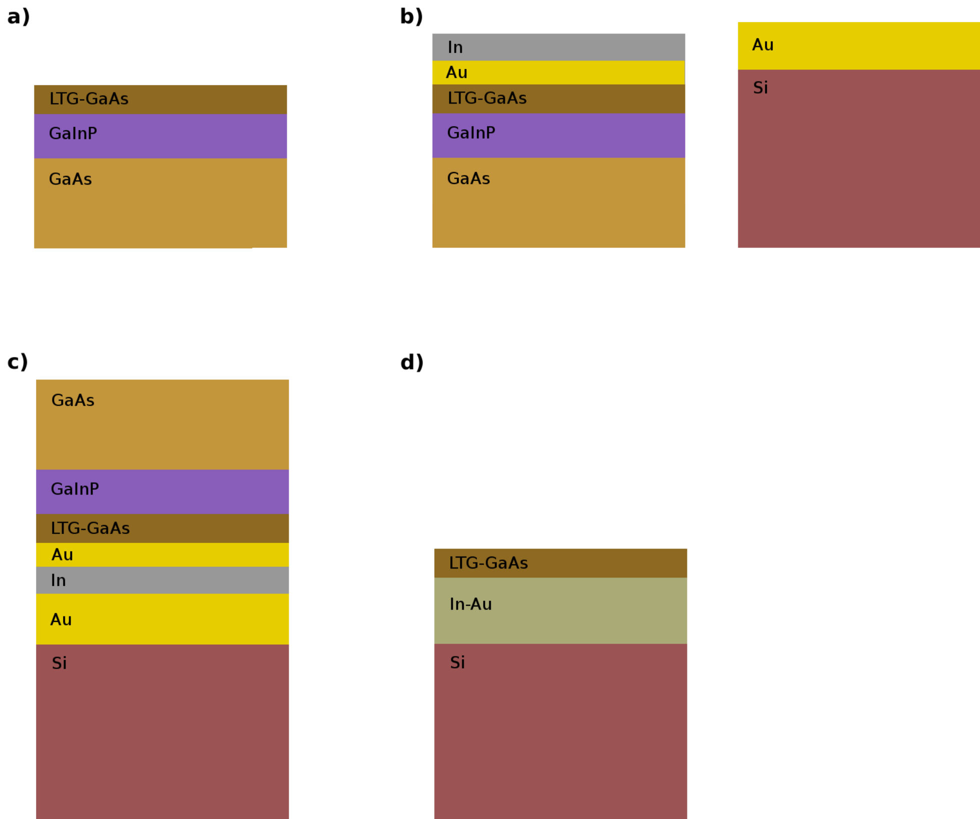


Figure 2.1: Schematic of the process used for the transfer of epitaxial layers. a) growth of a suitable etch stop layer (here GaInP) and the active layer(s) on the epitaxial substrate, b) metallization of the epitaxial layer and of the new host substrate, c) bonding between the metallic layers at controlled pressure and temperature, d) removal of epitaxial substrate and etch stop layer.

smaller wafer from excessive pressure and from breaking off.

The bottom plate with the wafer stack is loaded into the bonding machine and brought into "contact position". This is the position in which the top plate almost touches the top of the stack, without applying any pressure. As the contact position depends on the thickness of the stack, it is entered as a parameter in the bonding recipe.

Pressure is applied to the stack by increasing the air pressure inside a membrane which presses the top plate onto the stack, see figure 2.2. The membrane can expand up to 2 mm, maintaining a constant pressure even when the stack compresses or when the contact position was chosen too high.

The pressure indicated by the machine is the membrane pressure $p_{\mathrm{mem}}$, which is proportional to the bonding pressure $p_{\mathrm{bond}}$ experienced by the substrates. According to the manufacturer, the membrane has an area of $A_{\mathrm{mem}} = 222\,\mathrm{cm}^2$. The force of the top plate on the wafer stack

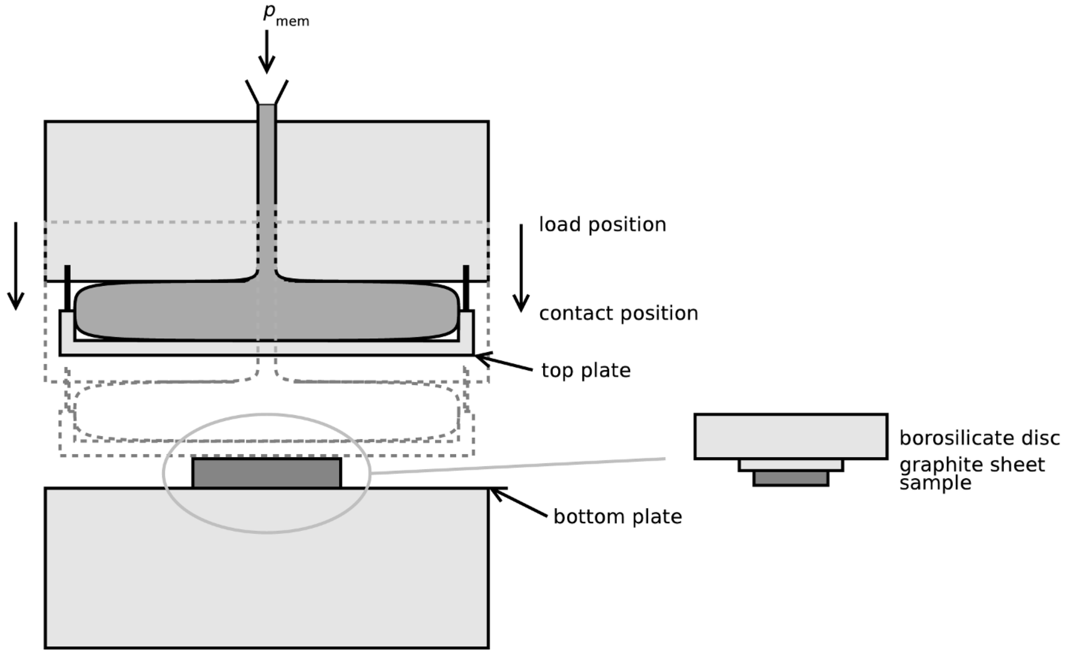


Figure 2.2: Schematic of the bonding machine. The sample is covered with a graphite sheet and a borosilicate disc is placed on top. The stack is entered into the machine while the top plate is in load position. The top plate is then lowered into contact position, where no pressure is exercised on the sample. The bonding pressure is regulated via the membrane pressure, $p_{\text{mem}}$.

is then $F = p_{\text{mem}} \cdot A_{\text{mem}}$, and the bonding pressure on the samples is $p_{\text{bond}} = F/A_{\text{sample}} = p_{\text{mem}} \cdot A_{\text{mem}}/A_{\text{sample}}$, where $A_{\text{sample}}$ is the area of the smaller of the two substrates. For a quarter of a 2 in wafer, $A_{\text{sample}} = 1\,\text{in}^2 \cdot \pi/4 \approx 5.07\,\text{cm}^2$, and a membrane pressure of $p_{\text{mem}} = 1000\,\text{mbar}$ corresponds to a bonding pressure of $p_{\text{bond}} \approx 4.39\,\text{MPa}$.

After introduction of the bond stack, the chamber is evacuated to $10^{-4}$ mbar. The top plate is brought into contact position, and pressure is applied by the membrane.

The heating step from ambient to the bonding temperature is defined as a temperature ramp taking 30 min, which is followed closely by the machine. The cool-down is much longer and limited by the cooling capabilities of the bonding machine. A long cool-down composed of several ramps is therefore employed. As can be seen in figure 2.3, cool-down is more efficient for the bottom plate; the top plate temperature does not follow exactly the desired ramp. The cool-down period is by far the longest step of the bonding process, taking more than 3 h of a total process time of approximately 6 h. After cool-down below 80 °C, the pressure is released, the chamber vented and the sample unloaded.

The original substrate is removed by a wet etching process. A GaAs substrate is removed in a mixture of $H_2O_2$:$H_2SO_4$:$H_2O$ with proportions 8:1:1. In order to improve the homogeneity

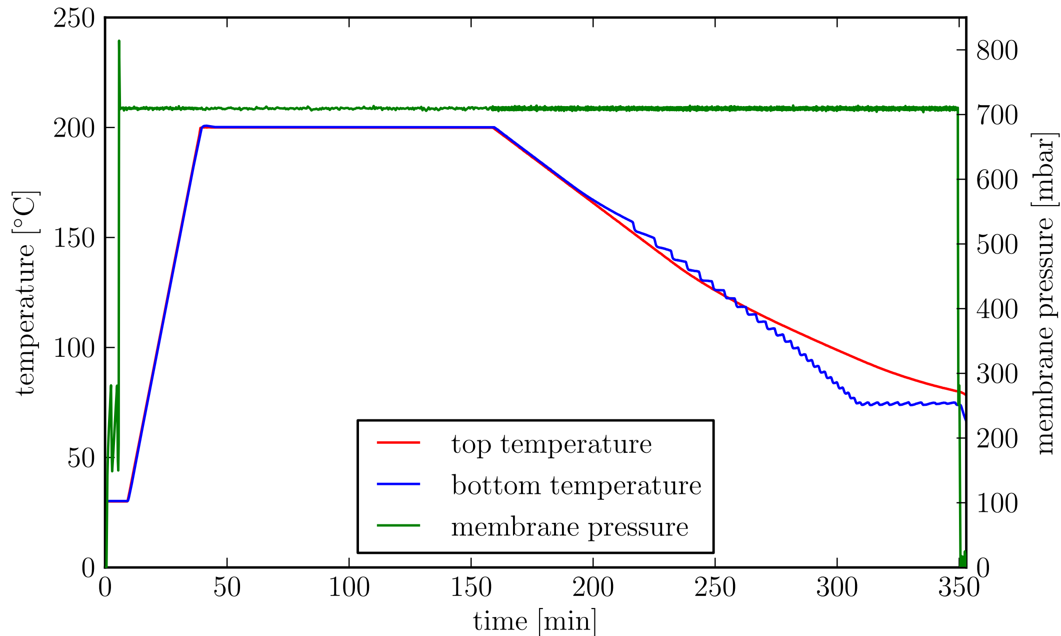


Figure 2.3: Temperature and pressure during a typical bonding process. This particular bond was formed at 200 °C during 2 h. The pressure indicated is the pressure in the membrane of the machine, it is proportional to the pressure on the sample. For an eighth of a 2 in-wafer, 700 mbar membrane pressure correspond to 6.1 MPa sample pressure.

of the etching process, the sample is mounted top-down on a rotating holder and dipped into the acid, while a magnetic stirrer mixes the acid.
A 450 $\mu$m thick GaAs substrate is etched in approximately 30 min. The etching is fastest in the center, but the borders are consistently less than 15 $\mu$m thick when the substrate is completely etched in the center. A 100 nm thick GaInP etch-stop layer is sufficient to protect the remaining layers until the GaAs substrate is completely removed everywhere. The etch stop layer is subsequently removed in HCl.

If the original substrate is InP, it is removed in HCl:$H_2O$ with proportions 2:1. In this case, the same type of agitation as used for GaAs has proven to be counterproductive, and resulted in an inhomogeneous etch with stripes of material left between regions of slow and fast etch. Instead, the sample is placed into the mixture without agitation. Etching of a typical 350 $\mu$m InP substrate takes approximately 90 min. Complete removal of the substrate does not necessarily start in the center, but usually starts at several disjoint regions separately. A suitable etch stop layer is $In_{0.53}Ga_{0.47}As$. However, before removal of the $In_{0.53}Ga_{0.47}As$ layer in $H_3PO_4$:$H_2O_2$:$H_2O$ (5:1:40), the interface between $In_{0.53}Ga_{0.47}As$ and InP is etched

non-selectively in $HIO_3$:$H_2O_2$:$H_2O$ (1:1:100).

In order to assess the quality of the bond, a cut is made with a focused ion beam (FIB), and the cross-section of the bond is observed by SEM. As sketched in figure 2.4, the observation by SEM is not perpendicular to the cross-section, and dimensions in height are compressed in the SEM image by a factor of $\cos\varphi$ for observation under an angle $\varphi$.

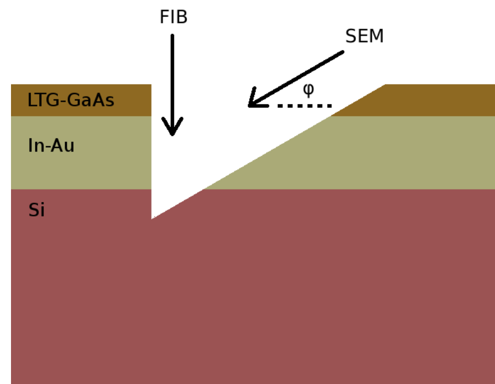


Figure 2.4: Schematic of the directions of focused ion beam (FIB) cut of the bonding layer perpendicular to the wafer surface and SEM observation under angle $\varphi$.

### 2.1.2 Thermocompression bonding

One often used method of bonding wafers is metal-metal thermocompression bonding [2, 3, 4, 5, 6]: Metal layers are deposited on both wafers to be bonded. The wafers are then brought into contact and bonding takes place at high pressure and elevated temperatures, but below the melting point of the metal. The high temperatures make the metal softer, and the pressure ensures intimate contact between the metal layers.

Gold is widely used for thermocompression bonds because of its softness and good chemical properties. Its chemical inertness makes oxidation between deposition of the metal and bonding less of a problem, and its resistance to acids makes later processing steps in the fabrication of devices possible.

A cross section of an Au–Au thermocompression bond between InP and Si is shown in figure 2.5. The bonding temperature was 200 °C and the pressure was 4.4 MPa. While part of the bonding layer is very uniform, voids between the two gold layers are visible occasionally. Also, the two initial gold layers can still clearly be distinguished, and the joint is visible along the whole cut. This shows that a bonding temperature of 200 °C is not high enough for very high quality Au–Au thermocompression bonding, but rather a compromise between

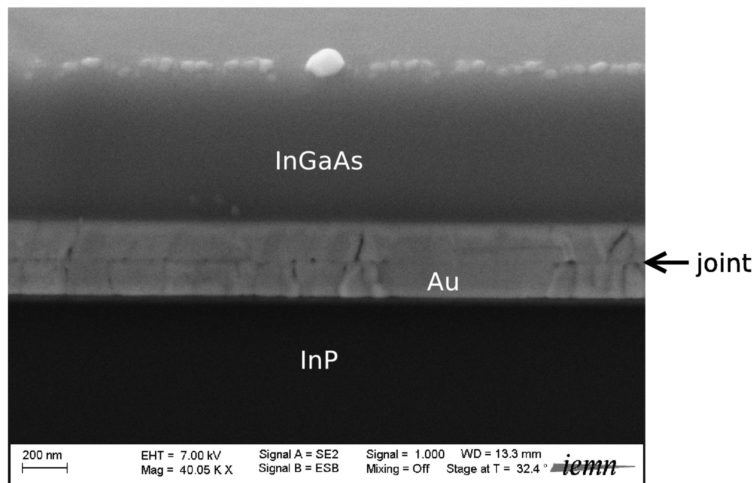


Figure 2.5: SEM image of FIB cut of Au–Au thermocompression bond between a Si substrate and a 1 $\mu$m thick epitaxial layer of $In_{0.53}Ga_{0.47}As$ on InP. Metallizations are 20 nm Ti and 200 nm Au on the Si substrate, and 200 nm Au on the InGaAs layer. Bonding was performed at 200 °C and 4.4 MPa for 90 min.

bonding quality and suppression of the undesired effects of higher temperature bonding. The clearly visible joint between the gold layers makes chemical wet etching of the bonding layer difficult, and adds a thermal resistance which reduces heat dissipation from the device to the substrate.

The problems associated with gold thermocompression bonding at low temperatures motivate the investigation of the possibility to replace gold by indium with its low melting point, softness, and good adhesive properties. As the melting point of indium is 156 °C, high quality thermocompression bonds can be expected below 150 °C. Figure 2.6 shows a schematic of the indium evaporation chamber. The indium crucible is surrounded by a metallic cylinder which is heated by high currents ($\sim$ 400 A). A glass plate is below the In crucible for thermal and electrical isolation. The evaporation rate is measured with a calibrated quartz crystal, whose eigenfrequency changes with the thickness (mass) of the layer evaporated on top of it. The evaporation rate depends on the heating current. When the desired evaporation rate is reached, the shutter is opened to start evaporation on the sample.

Figure 2.7 shows the cross section of an In–In thermocompression bond made at 100 °C and 6.1 MPa. Some large voids of several hundred nanometer length and tens of nanometers height are clearly visible. The voids are however not in the middle of the bonding layer, and the two initial indium layers or a joint between them can not be discerned. This means that the bonding itself is of high quality. As later bonding tests have shown, the amount of

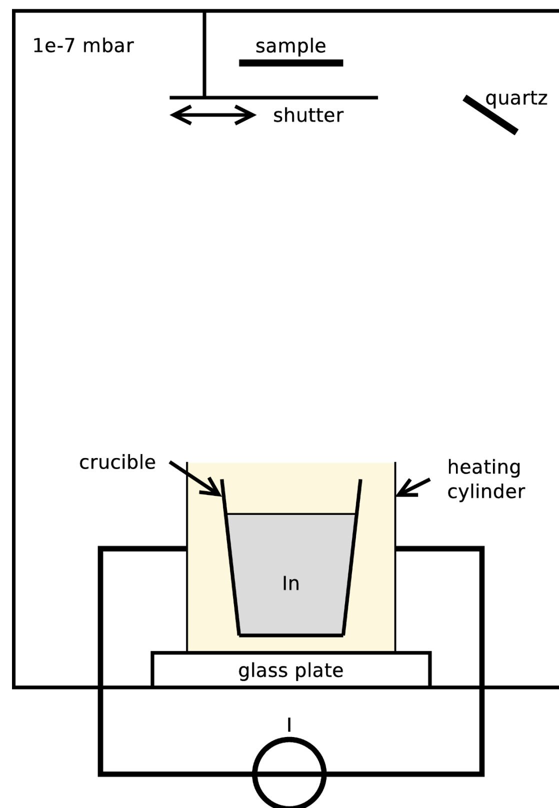


Figure 2.6: Schematic of the indium evaporation chamber.

voids can be reduced greatly by evaporating indium at higher rates. This would most likely have improved the quality of indium-indium thermocompression bonds.

Successful bonds between Si and GaAs substrates have been achieved at a wide range of temperatures, ranging from 120 °C down to only 30 °C. All of the samples showed voids in the bonding layer due to the low indium evaporation rate. However, all samples remained bonded and could not be separated mechanically using tweezers.

The transfer of an LTG-GaAs layer to a Si substrate by In-In thermocompression bonding using the process detailed in section 2.1.1 proved to be difficult: When removing the GaInP etch stop layer in HCl after bonding and after removal of the GaAs substrate, the indium bonding layer reacted violently with HCl under strong hydrogen production. Within a few seconds, the LTG-GaAs layer was lift-off from the Si substrate. The observed gas production was uniform across the whole LTG-GaAs layer, which indicates that the main process of the lift-off is HCl reacting with indium after passing through defects in the epitaxy, with only minor contributions by underetch starting from the borders of the LTG-GaAs layer. A protection layer between LTG-GaAs and indium layer might therefore have prevented the lift-off. However, this was not investigated further, as the attention was instead focused on

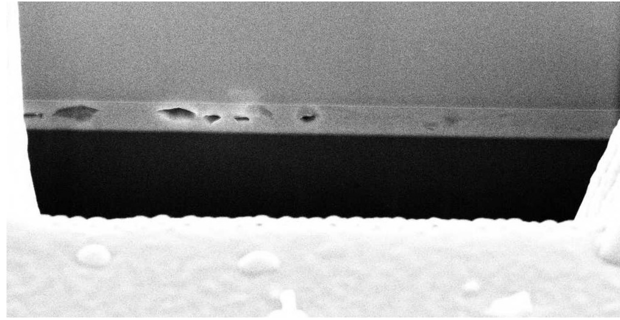

Figure 2.7: SEM image of FIB cut of In–In thermocompression bond. The metallization is 25 nm Cr and 400 nm In (2.7 $\mathrm{nm\,s^{-1}}$) on both the Si and the GaAs substrate. Bonding is performed at 100 °C and 6.1 MPa for 90 min.

indium-gold interdiffusion bonding.

In conclusion, indium-indium thermocompression bonds have been fabricated successfully. In contrast to gold-gold bonds, lower bonding temperatures are possible and the contact between the layers is better, with no joint visible in the indium bonds. Remaining voids in the bonding layer are due to low indium evaporation rates and could probably be considerably reduced with higher deposition rates.
However, two main drawbacks motivated the move to indium-gold interdiffusion bonding: the expected failure of the bond at temperatures above 157 °C due to the melting of the indium, which severely limits further processing steps of the transferred layer, and the high reactivity of indium with various acids, which additionally limits the available post-bonding processing steps.

### 2.1.3 Au–In Solid-liquid interdiffusion bonding

Indium-gold solid liquid interdiffusion (SLID) bonding is a low temperature bonding technique which can produce joints that are stable up to much higher temperatures than the temperature at which bonding took place. It was first proposed by Bernstein in 1966 [7].
In SLID bonding, two different materials are used to create the bond. One of the substrates to be bonded is covered by material L, which has a low melting point, while the other substrate is covered by a material with higher melting point, denoted H. Bonding takes place between the melting points of L and H. During bonding, the material L melts, wets the whole surface, and diffuses into material H. An intermetallic between L and H is formed, which can have a higher melting point than L. This type of bonding is very interesting for semiconductor joining, because subsequent steps in the fabrication process are not limited by the bonding temperature.

Interesting low-melting point metals include indium (156.6 °C), and tin (232 °C). Potential candidates for the high-melting point metals are gold, silver, and copper. The In–Au system has been chosen for further investigation, because of the low melting point of indium and the better resistance to oxidation of gold as compared to silver and copper.

#### Determination of the relative layer thicknesses

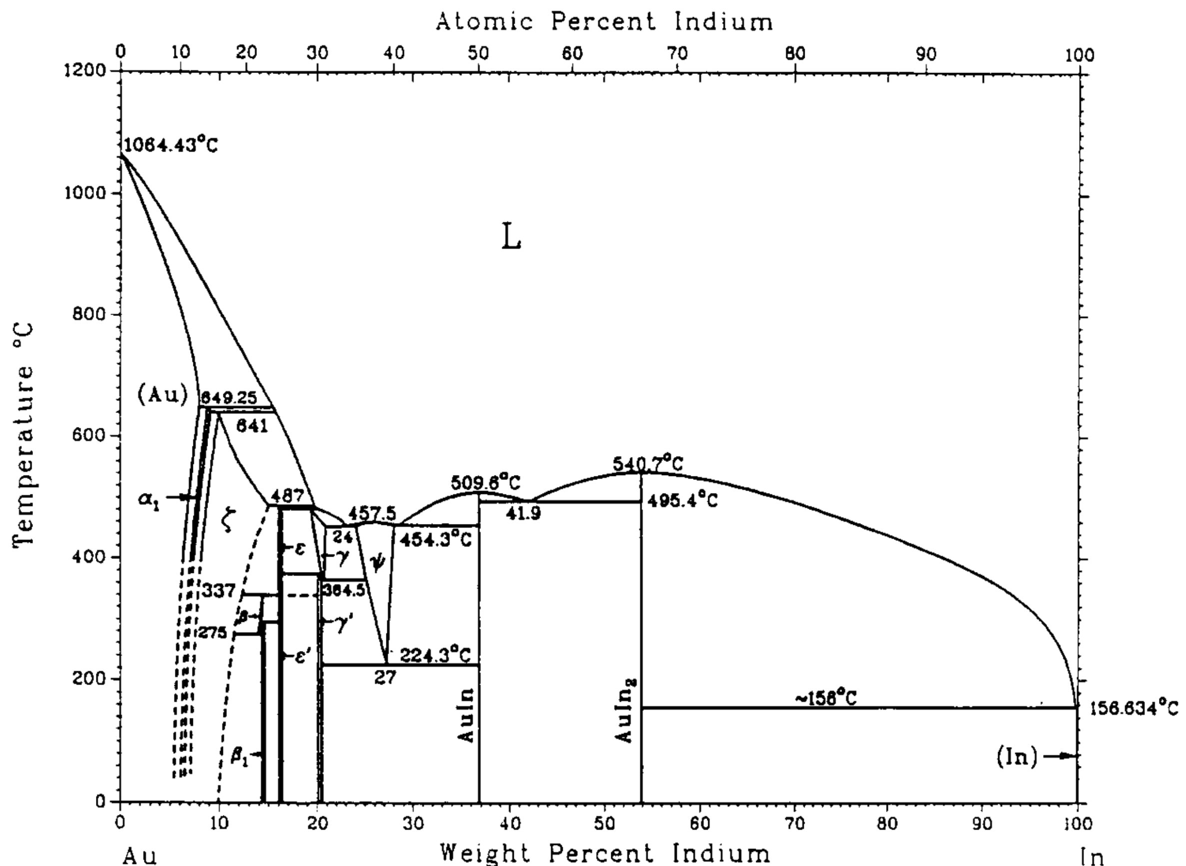


Figure 2.8: Equilibrium phase diagram of the Au–In binary system [8].

The equilibrium phase diagram of the In–Au system (figure 2.8) shows that at indium contents above 67 at%, the two compounds $AuIn_2$ and In are present. Shieu *et al.* [9] have shown that joints that had nonalloyed In in them were less strong than when all indium has been transformed into one of the In–Au compounds. Compositions with less than 67 at% indium are therefore chosen for further investigation.

The diffusion and the stability of the various In–Au compounds formed at room temperature have been studied by Simić *et al.* [10]. Gold and indium layers of various thicknesses were

evaporated onto glass substrates, and the compounds formed were identified at several times after deposition by X-ray diffractometry.
It has been found that $AuIn_2$ is formed immediately, and remains stable for at least 9 months when the indium content is above 45 wt%. For indium contents between 45 wt% and 53 wt%, only $AuIn_2$ could be identified, while at higher indium contents In was found as well.
The next compound found for increasing Au contents is AuIn. It forms during several days after evaporation, and then remains stable for the 9 months investigated if the In content is between 23 and 36 wt%. At still higher Au contents, the compounds $Au_7In_3$ and $Au_4In$ could be identified, but are formed only after several weeks to months.

The relatively slow formation of compounds with higher Au content than 50 at% ($\approx$ 63 wt%) demonstrated by Simić *et al.* as well as the void formation due to differences in the density of the various compounds formed [7] make bonding layer compositions with less than 50 at% indium less appealing.
The most interesting compositions for SLID bonding therefore are between the compounds AuIn and $AuIn_2$, that is between 50 at% (37 wt%) and 67 at% (54 wt%) indium. With densities at standard conditions of $\rho_{\mathrm{Au}} = 19.3\,\mathrm{g/cm^3}$ and $\rho_{\mathrm{In}} = 7.31\,\mathrm{g/cm^3}$, and the atomic masses $m_{\mathrm{Au}} = 197.0\,\mathrm{u}$ and $m_{\mathrm{In}} = 114.8\,\mathrm{u}$, the corresponding layer thicknesses are between $h_{\mathrm{In}}/h_{\mathrm{Au}} = 1.54$ and 3.08.

Most of the bonds are fabricated at layer thicknesses $h_{\mathrm{In}}/h_{\mathrm{Au}} = 2$, which corresponds to 43.1 wt% indium and is close to the eutectic at 41.9 wt%. However, as evidenced by SEM images of cross-sections of the bonding layer (figure 2.9), a uniform composition is not reached. Instead, two phases can be discerned, which correspond most likely to $AuIn_2$ in the center of the bond, and AuIn at the borders. The color of the surface of bonding layers after etching of one of the substrates is clearly different from the color of Au, which indicates that all of the gold is consumed by reactions with indium.

#### Au anti-oxidation layer

Indium oxidizes practically instantly on contact with air. In order to avoid the oxide layer, some authors [8] suggest to depose a thin gold layer on top of the indium layer within the same vacuum cycle. The two metals immediately form the $AuIn_2$ compound [8], which is resistant to oxidation.
Kumar *et al.* [11] reported adverse effects of such a gold layer, as the $AuIn_2$ compound with its high melting point inhibits indium diffusion during bonding more than the oxide layer that is formed without the gold layer.

The evaporation chamber used for indium evaporation is also equipped with a crucible for gold evaporation. Gold evaporation rates are slow and not material efficient, mostly due to the geometry of the chamber, which is optimized for indium evaporation. Thin layers of gold can be deposited nonetheless, and some bonds are fabricated with a thin gold protection layer on top of the indium layer.

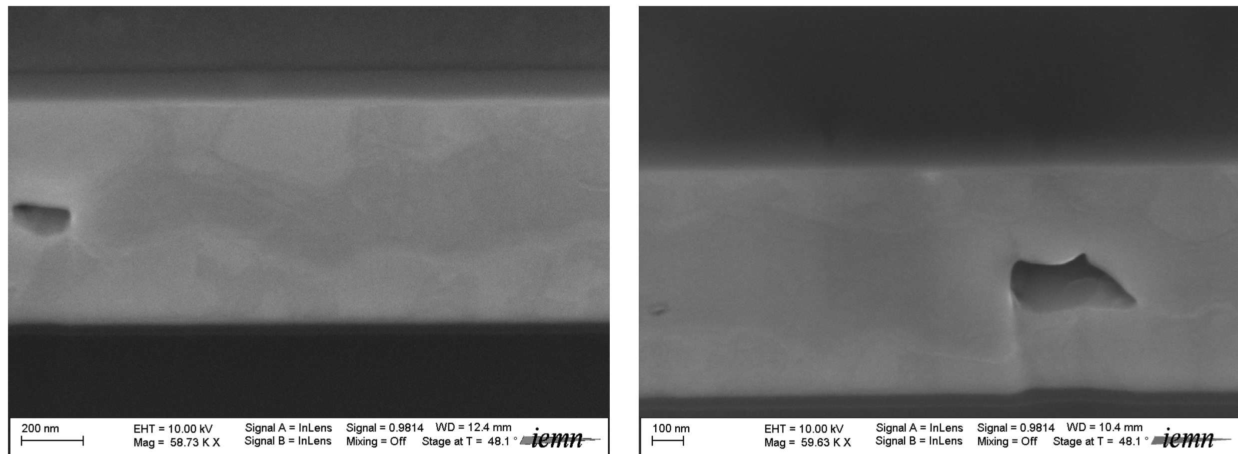


Figure 2.9: SEM images of cross sections of two different bondings. The processes used are the same except that an additional 20 nm gold protection layer has been deposited on the sample to the left. The metallizations are 30 nm Ti, 150 nm Au on both GaAs and Si substrate, and additionally on the GaAs wafer 600 nm In, followed on the left sample by 20 nm Au. Bonding took place at 200 °C for 2 h under 6.1 MPa pressure. Indium evaporation rates are 7.4 nm $s^{-1}$ for the left sample, and 6.1 nm $s^{-1}$ for the right sample.

In figure 2.9 are shown SEM images of FIB cuts of two different bondings. In both cases, an eighth of a 2 in GaAs substrate has been bonded to a quarter of a 2 in Si wafer. On one sample a 20 nm Au protection layer was evaporated on top of the indium layer.
No difference is discernible between the two bondings from the SEM images. In both cases there is no joint visible, and the density and size of voids is comparable. However, as discussed in the next section, fewer voids would be expected for the higher indium evaporation rate of the sample with the additional gold layer.

In contrast to the reports by Kumar *et al.* [11], no strong diminution in the quality of the joint itself could be observed by adding the gold layer. This could be due to the difference in thicknesses of the anti-oxidation layers as 20 nm Au were used here instead of 120 nm [12]. However, an improvement of the quality of the bond due to the anti-oxidation layer could also not be observed, and all further bondings are therefore fabricated without the additional gold layer.

#### Influence of In evaporation rate

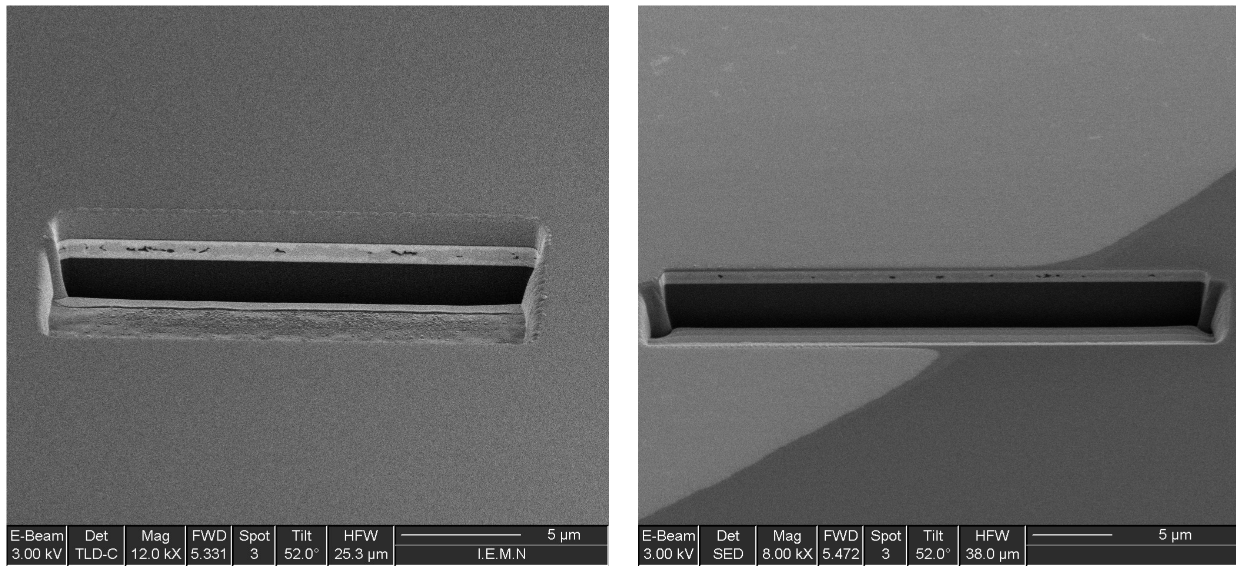


Figure 2.10: SEM images of FIB cross sections of In–Au SLID bonding layers fabricated with different In deposition rates. Metallizations are 30 nm Ti and 150 nm Au on the Si substrate, and 30 nm Ti, 150 nm Au, 600 nm In, 20 nm Au on the GaAs substrate. The rate of In deposition was $2.7\,\mathrm{nm\,s^{-1}}$ on the sample to the left, and $7.4\,\mathrm{nm\,s^{-1}}$ on the sample to the right. Bonding took place at 200 °C for 2 h under 6.1 MPa pressure. The FIB cut is $19\,\mu$m wide on the left sample, and $34\,\mu$m wide on the right sample.

SEM images of FIB cross sections of two samples are compared in Figure 2.10. The only difference in the preparation of the sample is the evaporation rate of indium. It is very clear that an evaporation rate of $7.4\,\mathrm{nm\,s^{-1}}$ results in far fewer voids than a rate of $2.7\,\mathrm{nm\,s^{-1}}$.

The dependence of the density of voids on the indium evaporation rate can be explained by the surface roughness of the indium layer. During film deposition, several mechanisms influence the microstructure of the film. These include nucleation, island growth, coalescence of islands, grain coarsening, formation of polycrystalline islands, development of a continuous structure, and film growth [13], see also figure 2.11. The type of microstructure that is developed is similar for different materials at the same homologous temperature $T_\mathrm{s}/T_\mathrm{m}$, where $T_\mathrm{s}$ is the substrate temperature during film growth, and $T_\mathrm{m}$ is the melting point of the material. Due to the low melting point of indium, the ratio $T_\mathrm{s}/T_\mathrm{m}$ is $\approx 0.68$ at room temperature. At these high homologous temperatures, diffusion effects dominate film growth and films with coarse grains are obtained [13].

A study performed on indium deposition on $SiO_2$ and glass substrates by sputtering showed that larger grains result in a higher surface roughness [14]. Smaller grains were obtained by

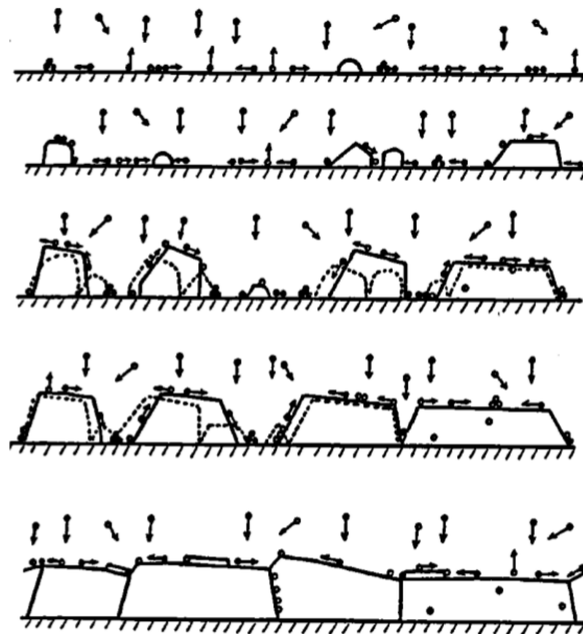

Figure 2.11: Illustration of the growth processes during film growth [13].

lower substrate temperatures during film deposition, and by higher deposition rates. Both methods reduce the diffusion effects relative to other mechanisms like nucleation. The lower roughness of these films was measured by AFM, and a higher reflectance of the films was also demonstrated [14].

It is likely that the reduced roughness of indium layers deposited at high evaporation rates is responsible for the reduction of voids in the bonds. Additionally, the strong tendency of indium to form grains in the high diffusion region (low evaporation rate) might lead to the incorporation of voids in the indium layer already during evaporation.

The best bonding results are obtained with indium deposition rates between 7 and 7.5 $\mathrm{nm\,s^{-1}}$. Higher rates are difficult to achieve in the evaporation chamber used. Very high crucible temperatures are needed for deposition rates of 7.5 $\mathrm{nm\,s^{-1}}$, and deformation of the glass plate below the indium crucible (figure 2.6) has been observed during maintenance of the chamber after many depositions at this rate. Higher evaporation rates also result in reduced material efficiency, because of increased evaporation of material during the heating phase before film deposition and during cool-down afterwards.

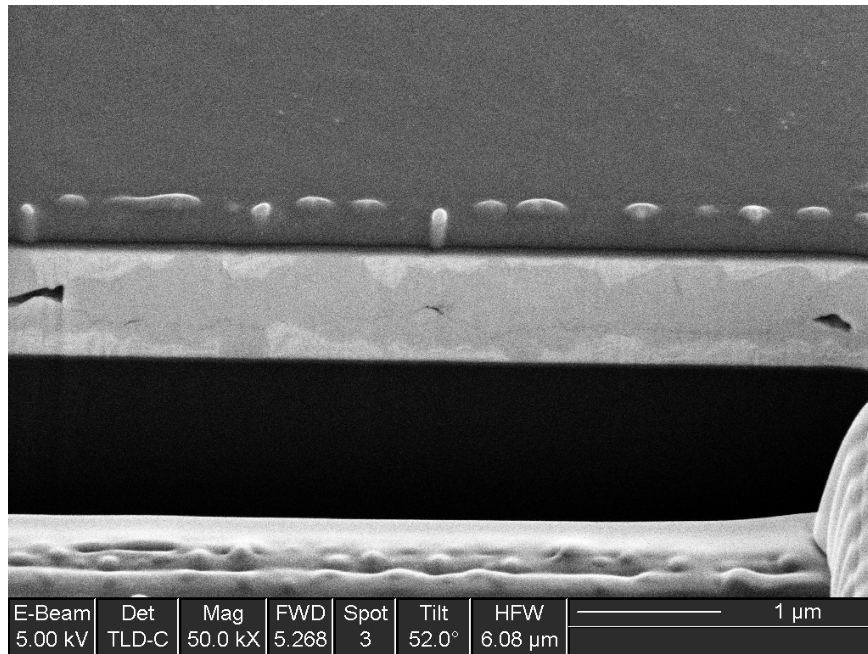


Figure 2.12: SEM image of FIB cross section of Au rich In–Au SLID bonding. Metallizations are 30 nm Ti and 225 nm Au on the Si substrate, and 30 nm Ti, 225 nm Au, 450 nm In (6.4 nm $s^{-1}$) on the GaAs substrate, giving a composition with 27.5 wt% In. Bonding took place at 200 °C for 2 h under 6.1 MPa pressure.

#### Influence of the composition of the bond

The influence of the composition on the bonding quality is also investigated. Figure 2.12 shows the cross section of a bonding layer with 27.5 wt% indium. Several voids are visible, and they are connected by a visible joint between the layers. The quality of the bond is lower possibly due to a larger fraction of the thinner indium layer diffusing into the gold layer before the sample reaches the bonding temperature. The intermetallics are harder than indium and result in less intimate contact between the substrates.

#### Transfer of epitaxial layers to rough substrates

Shown in figure 2.13 are two bonds fabricated on different substrates, Si and diamond coated Si. Both bonds are of very high quality, with almost no voids and without visible joint. The diamond layer on the diamond coated Si substrate is 10 $\mu$m thick and polycrystalline. The heat spreading capabilities of this layer are investigated in section 2.2. The surface of the diamond layer is relatively rough, and the excellent bond quality shows that the roughness can be overcome by SLID bonding thanks to the softness and liquid phase of indium.

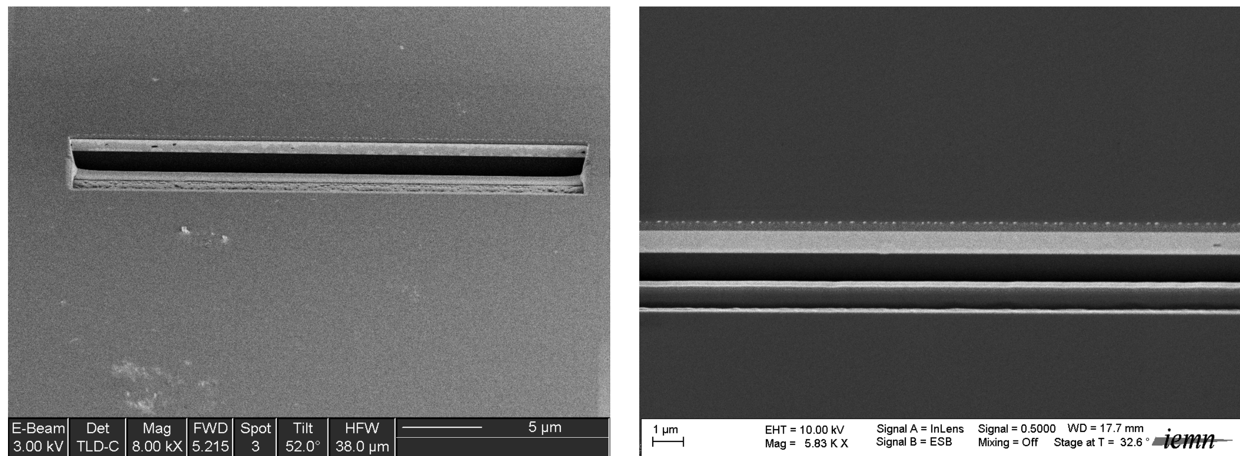


Figure 2.13: SEM images of FIB cross sections of In–Au SLID bonding layers after bonding an LTG-GaAs layer to a Si substrate (left) and a diamond-coated Si substrate (right). Metallizations are 30 nm Ti and 150 nm Au on the Si (diamond-Si) substrate, and 30 nm Ti, 150 nm Au, 600 nm In on the GaAs substrate. Bonding took place at 200 °C for 2 h under 6.1 MPa pressure. Indium evaporation rates for the left and right sample were 7.4 nm s$^{-1}$ and 7.3 nm s$^{-1}$, respectively.

It is interesting to compare the two samples of figure 2.13 with the sample to the right in figure 2.10. All three samples have the same metallization and are bonded with the same parameters, except for the gold anti-oxidation layer of the latter sample. More voids are visible in the sample with the anti-oxidation layer, which is consistent with the observation of increased voids in bonds with higher gold content.

#### Bonds fabricated at temperatures below 200 °C

The result of attempts to further reduce the bonding temperature are shown in figure 2.14. The joint is not visible in the sample bonded at 180 °C, and the overall quality is good with some voids attributable to the indium evaporation rate, which was reduced to 5.2 nm s$^{-1}$ in order to save material. On the sample bonded at 170 °C, a crack connecting the voids is visible, similar to the result obtained at compositions with higher gold contents. A sample bonded at 160 °C showed a larger crack than the sample bonded at 170 °C, confirming that the low temperature is the main reason for the crack.

#### Summary

Lower bonding temperature, higher gold content in the composition, and gold anti-oxidation layer all reduce the amount of indium available in the liquid phase during bonding. The

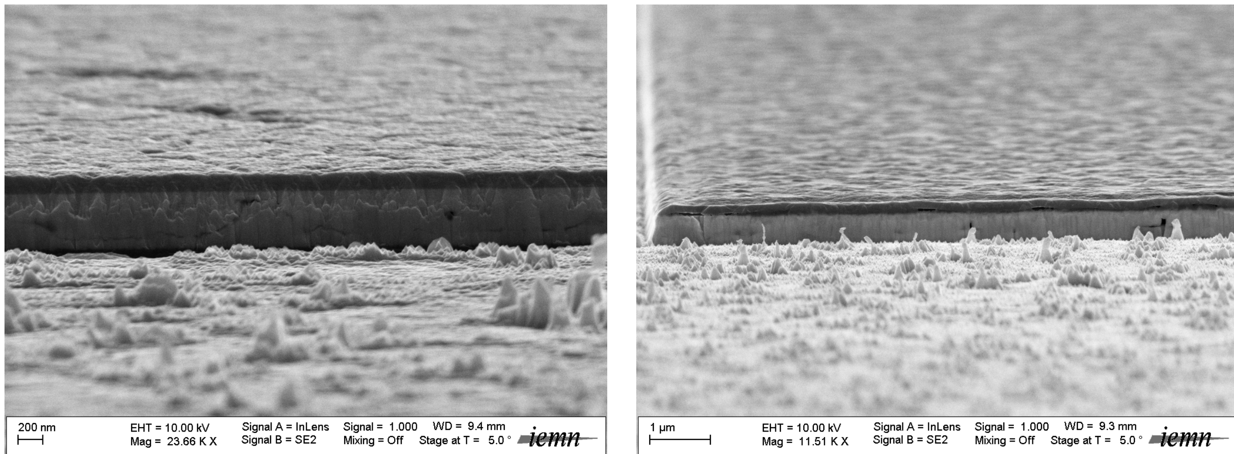


Figure 2.14: SEM images of cross sections of In–Au SLID bonding layers after 10 min dry etching. The left sample has been bonded at 170 °C, the right sample at 180 °C. Metallizations are 100 nm Ti and 75 nm Au on the Si substrate. 75 nm Au and 300 nm In ($5.3\,\mathrm{nm\,s^{-1}}$) are deposited on the (now removed) InP substrate of the left sample, and 75 nm Au, 10 nm Pt, 75 nm Au, and 300 nm In ($5.2\,\mathrm{nm\,s^{-1}}$) on the (removed) InP substrate of the right sample. The patterns are protected by an initially 200 nm thick Ti layer. Bonding took place for 2 h under 4.4 MPa pressure.

bond quality is lower, with an increased number of voids, and a visible crack in the bonding layer in most samples. This underlines that the liquid phase is required in order to obtain the best bonds, and careful selection of the composition is necessary.

Very high quality bonds have been fabricated by choosing the correct parameters. The bonding joint is not visible in cross sections of the bonding layer, and very few voids are found. At low indium deposition rates, many more voids are formed in the indium layer. An increased number of voids is also observed if a gold anti-oxidation layer is deposited on the indium layer, or if the composition contains a higher amount of gold. Bonding at temperatures of 170 °C or lower results in a crack in the bonding layer, as does increasing the amount of gold in the composition.

### 2.1.4 Optical properties of the bonding layer

The optical properties of the bonding layer are important for some applications. As an example, the bonding layer is used as a mirror for laser light illuminating the photoconductor in the vertical photoconductor configuration by Peytavit *et al.* [1]. In this case, a high reflectance at the interface between semiconductor and bonding layer is desired.

During In–Au SLID bonding, indium diffuses into the gold layers and In–Au compounds

are formed. Inspection by eye after removal of one substrate already shows that these compounds have different optical properties than the gold originally deposited on the semiconductor.

The refractive index of bonding layers with varying composition is measured using a Horiba Jobin Yvon ellipsometer. The bonds are fabricated as described in section 2.1.1. After bonding and removal of one substrate, the reflectivity of the surface of the bonding layer is measured. The composition of the bonding layer is not homogeneous, and the values obtained are effective indices. The penetration depth at 1.55 $\mu$m is 24 nm for Au. The measurements indicate that the reflectance of the intermetallic is less than that of gold, which is a very good mirror at 1.55 $\mu$m wavelength (99.3% in air). The measured values are summarized in table 2.1. Larger Au contents result in refractive indices closer to that of pure Au, but do not reach the value of Au, and reduce the quality of the bond.

| Sample | n | k | metal content of bonding layer |
|---|---|---|---|
| pure Au | 1.2 | 10.5 | 150 nm Au |
| 16.8 wt% In | 2.0 | 10.4 | 750 nm Au, 400 nm In |
| 27.5 wt% In | 3.6 | 8.9 | 300 nm Au, 300 nm In |
| 43.1 wt% In | 3.6 | 8.5 | 150 nm Au, 300 nm In |
| Pt barrier | 1.3 | 10.8 | 150 nm Au, 300 nm In – 20 nm Pt – 75 nmAu |

Table 2.1: Refractive indices at 1.55 $\mu$m of bonding layers, measured by ellipsometry. The pure Au sample is measured after evaporation of Au, all other samples are measured after bonding and removal of one substrate. The samples were bonded for 2 h at 200 °C.

Distinct layers for bonding and for reflection would allow to independently optimize the bonding and optical properties. A diffusion barrier which inhibits the diffusion of indium from the bonding layer to the reflection layer is then necessary. Several metals are investigated as to their capability of separating the two layers.

The following metallizations are prepared on Si substrates: 20 nm Ti – 75 nm Au – 300 nm In – 75 nm Au – 20 nm X – 75 nm Au, where X denotes one of Ti, Pt, or no metallization. The samples are cleaved into two pieces, and one is placed in an oven at 200 °C for 2 h to simulate the bonding process. Figure 2.15 shows photographs of the three samples after heating of one of the pieces.

The color of the heated piece clearly changes for the samples without diffusion barrier or with X = Ti, due to the diffusion of indium into the top gold layer. On the other hand, Pt

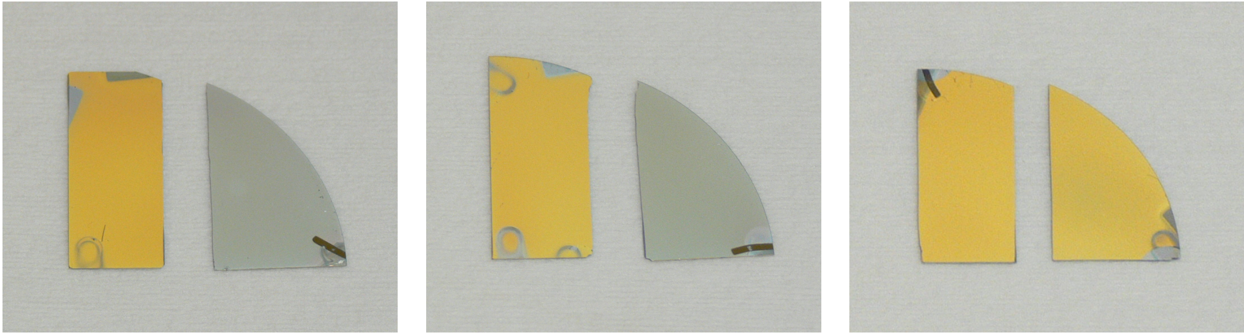

Figure 2.15: Photographs of Si wafers metallized with 20 nm Ti – 75 nm Au – 300 nm In – 75 nm Au – 20 nm X – 75 nm Au. After metallization, the sample is cleaved, and the part to the right is heated for 2 h at 200 °C. Left: no barrier layer X, middle: X = Ti, right: X = Pt.

appears to be an effective barrier with virtually no color change of the sample after heating. The surfaces are not mirror-like, but rough, which is due to the indium metallization.

For ellipsometry measurements, a smooth surface is required. Wafer bonding using the Pt barrier layer is performed, and after removal of the substrate, a mirror-like, gold colored surface is obtained. Ellipsometry measurements on this surface show that indeed the refractive index of gold is obtained (table 2.1).

In summary, it has been shown that Pt is an effective diffusion barrier for the In–Au SLID bonding layers. It can be employed as a barrier between bonding and reflective layer, allowing to separately optimize the bonding process and optical properties.

### 2.1.5 Etching of the bonding layer

For some applications it is advantageous to etch the bonding layer at specific locations during device fabrication. If the epitaxial layers are bonded to a high resistivity substrate, etching of the metallic bonding layer allows to fabricate access pads to the device on the high resistivity substrate, such as CPW accesses for on-wafer measurements. Removing the metallic bonding layer except where needed for the device also makes it possible to integrate photomixers with antennas which radiate into the substrate, for example broad-band spiral antennas or log-periodic antennas.

Previous work at the IEMN has resulted in a process for etching Au–Au thermocompression bonds [2]. Pure wet etching in a solution of KI and $I_2$ in water did not yield the desired results: The solution entered the joint between the two gold layers of the bond, resulting in a large under-etch, up to a complete lift-off of the device structures. A combined dry and

wet etch approach has therefore been employed: A resist mask is used to protect the devices, and the top Au layer including the bonding joint is etched by dry etching. A different resist mask is then employed to protect the devices and to cover the side of the bonding joint, so that the remaining gold can be etched by wet etching.

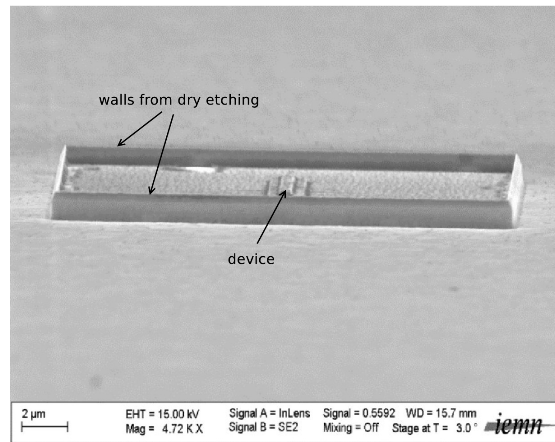


Figure 2.16: SEM image of a transistor during fabrication after etching of the Au–Au thermocompression bond by combined dry etching and wet etching, from [2]. Thin walls of material remain around the device.

This method was successful in exposing the underlying high-resistivity substrate, however a thin wall of material was always left at the borders of the mask used for dry etching, most likely due to redeposition of material during dry etching, see figure 2.16. Also, the removal of the protecting resist after dry etching was difficult, traces of resist were often left on parts of the sample.

Etching the In–Au intermetallic formed during SLID bonding turned out to be very challenging, mostly due to the difficulty of finding a solution which homogeneously etches the different compounds in the bonding layer. Moreover, while several authors have published work on In–Au SLID bonding, no results of etching the intermetallics have been presented.

When removing the GaAs substrate after bonding in the piranha solution ($H_2O_2$:$H_2SO_4$:$H_2O$), it is observed that the In–Au bonding layer is etched as well. The GaAs substrate first is dissolved completely in the center, and the area without GaAs expands from there. During etching, a relatively wide gradient area between the center, where the bonding layer has also been etched, and the border of the GaAs wafer appears, which indicates that the etch speed of the In–Au layer in piranha is relatively slow. Due to the etching of In–Au in piranha, all bonds that are prepared without epitaxial layers are fabricated using InP as top substrate, as the removal of InP in HCl does not etch the bonding layer.

Pure wet etching of the bonding layer in gold etchant (10 g KI and 3 g $I_2$ dissolved in 120 ml

$H_2O$) is attempted. In contrast to Au–Au thermocompression bonding, the bonding joint is not visible in samples using In–Au SLID bonding, and there should be no problems related to the solution entering the joint. However, as shown in figure 2.17, the etching of In–Au in gold etchant is not uniform. Etching starts in small areas which then increase in size, while parts of the surface remain nearly unetched. It appears that the gold rich surface (likely AuIn) is etched slower than the middle of the bond (likely $AuIn_2$), resulting in fast lateral spread of the etchant once the surface has been penetrated. This makes the etching process unpredictable and the etching around small patterns unfeasible.

As the piranha solution has shown to etch the bonding layer, pure wet etching using piranha is also attempted. However, a similarly non-uniform etch as obtained with gold etchant is observed.

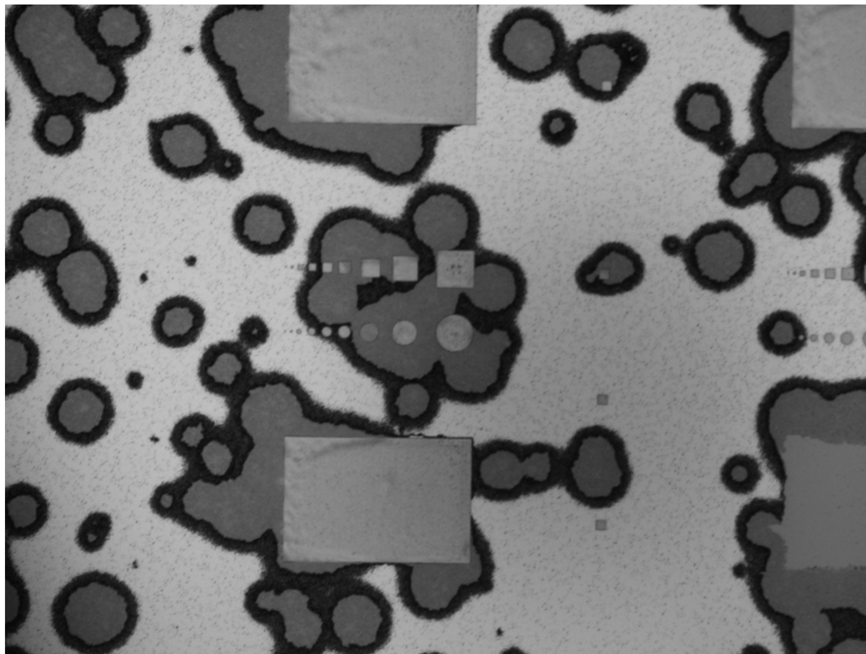

Figure 2.17: Image taken with optical microscope of the surface of the In–Au bonding layer after 45 s etch in gold etchant (10 g KI and 3 g $I_2$ dissolved in 120 ml $H_2O$). The largest patterned squares (circles) have 30 $\mu$m sidelength (diameter). The bonding layer contains 150 nm Au and 300 nm In (43.1 wt% In), the patterns are 200 nm Ti.

Dry etching of the bonding layer using a Plassys MU 350 ion miller is investigated. Instead of using a resist mask, with the associated problems of left-over thin walls from redeposition and difficult resist removal after dry etching, a titanium mask is used. The 200 nm titanium layer is deposited by a lift-off process, and can be removed in HF or buffered oxide etch (BOE, based on $NH_4F$:HF 7:1).

SEM images of two samples after 10 min dry etching are shown in figure 2.14. The Ti mask layer is visible on the patterns, and the bonding layer has been etched where no Ti mask was deposited. However, the surface of the etched part is not smooth, but small features remain. Several attempts have been made to remove these features by wet etching.
Images taken after 12 s etching in gold etchant are shown in figure 2.18. The Ti mask is not etched noticeably, but the bonding layer below it is underetched by approximately 3 $\mu$m. However, the substrate surface is still not clean. The small features are etched more slowly in gold etchant, hinting at a different composition.

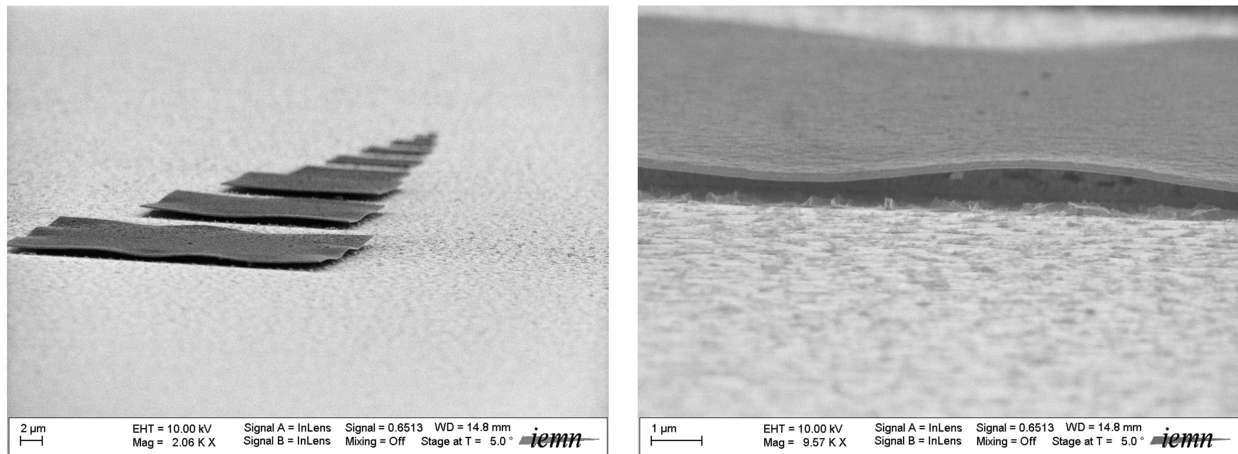


Figure 2.18: SEM image of sample after 10 min dry etching and 12 s gold etchant.

Another approach to obtain a clean surface is undertaken: a 100 nm thick titanium layer is deposited on the Si substrate before the other metallizations. If the Ti layer is reached during dry etching, it can then be removed in HF. Figure 2.19 shows a sample after 10 min of dry etching. The Ti layer below the bonding layer can clearly be seen.

During the first 45 s of etching in HF (5% in $H_2O$), gas production can be observed. In this first attempt, the sample is left in HF for several minutes nonetheless, to be certain of removing the Ti layer completely. As evidenced in the SEM images shown in figure 2.20, the Ti layer is completely etched, and the patterns are lifted off. The Ti mask layer is also removed, and the bonding layer is not etched. However, the surface of the substrate is only clean where the patterns were, and the remains of dry etching are not lifted off as expected. It is not understood why the remains are not lifted off, even though the relatively thick titanium layer below is not removed during dry etching.

Several attempts are undertaken to etch the remains. Piranha solution slowly etches the remains under strong gas production. The best results have been obtained by etching in piranha solution after dry etching, followed by HF etching of the titanium layer. However,

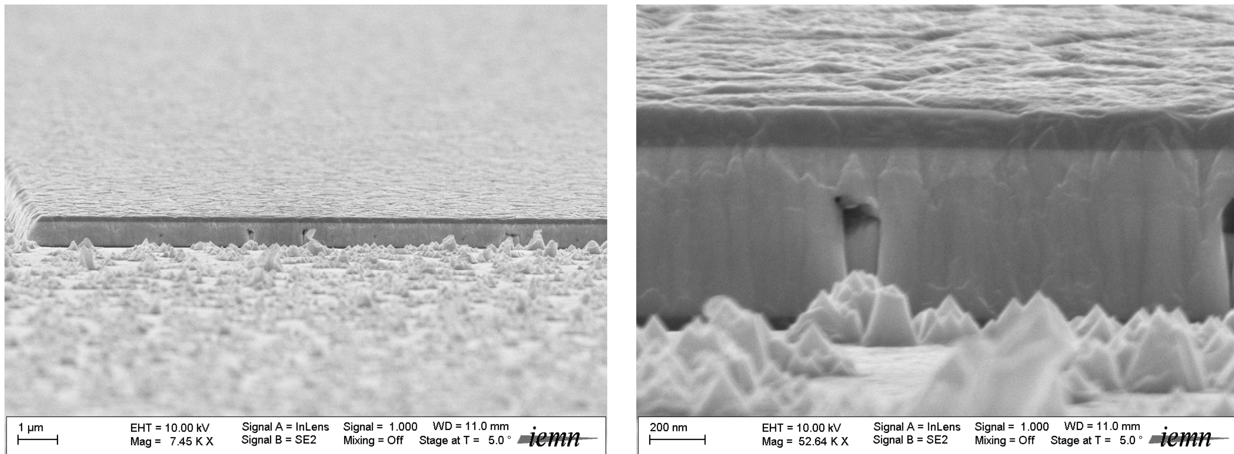


Figure 2.19: SEM image of sample after 10 min dry etching. A 100 nm thick Ti layer has been deposited between Si substrate and bonding layer.

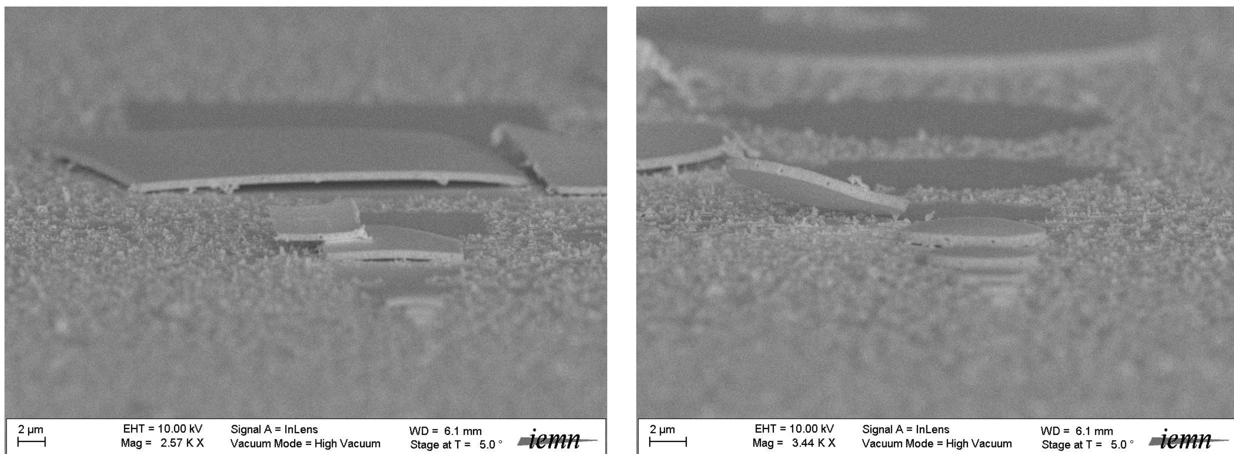


Figure 2.20: SEM image of sample after 10 min dry etching and several minutes wet etching in HF (5% in $H_2O$).

the results are not sufficient for the fabrication of CPW lines on high resistivity substrates, and a suitable protection for the patterns during etching is not known.
Because of these difficulties, etching the bonding layer is not pursued further. Instead, device access for on-wafer measurements is done by depositing an insulating $SiO_2$ layer, and by fabricating grounded CPW lines on the $SiO_2$ layer. The process is detailed in section 4.2.2

The use of a titanium mask for dry etching has been demonstrated to work well. The mask layer is easy to remove in HF, and no redeposition on the sides of the Ti layer, as had been observed for resist masks [2], was found. Using a Ti mask for dry etching of Au–Au thermocompression bonds has not been tried, but it is expected that this would solve the

main problems that arise during dry etching with resist masks.

## 2.2 Thermal characterization of bonded LTG-GaAs layers

In order to evaluate the effect of the transfer of epitaxial layers to high thermal conductivity substrates on the thermal properties of devices, thermal measurements are performed in a configuration similar to vertical photoconductors. LTG-GaAs layers are transferred to a new substrate, and Ti strips are deposited and heated by a current. An infrared thermal imaging camera is used to measure the resulting temperature, and several combinations of bonding parameters and host substrates are compared.

### 2.2.1 Sample preparation and measurement setup

The samples are prepared using the bonding method detailed in section 2.1.1: parts of a 250 nm thick LTG-GaAs layer are transferred to different substrates using various bonding parameters. Titanium resistances 8 $\mu$m wide, 50 nm high, and with eight different lengths between 100 $\mu$m and 1 mm and gold contact pads are deposited using standard electron-beam lithography and lift-off techniques. A photograph of the fabricated resistances taken with an optical microscope is shown in figure 2.21.

Figure 2.21: Photograph of Ti resistances with Au access pads taken with an optical microscope. The resistances shown are 8 $\mu$m wide and between 100 $\mu$m and 486 $\mu$m long.

The resistance is heated electrically. Two needles are placed on each contact pad. One of the needles of each pad is used for current injection and the other one for voltage measurement.

This four-wire method reduces errors in the voltage measurement due to resistances in the wires and contacts, and allows for more exact determination of the heating power. Typical injected currents are between 10 mA and 20 mA.

The measurements are based on an infrared thermal imaging camera (QFI InfraScope) which is used to measure the temperature of resistances on the samples heated by current injection. The InSb pixels of the camera are liquid nitrogen cooled to reduce noise, are sensitive between 2 $\mu$m and 4 $\mu$m wavelength and the resolution is 500 × 500 pixels. At the highest magnification, one pixel corresponds to an area of 2 $\mu$m × 2 $\mu$m. During measurements, the bottom of the substrate is kept at a constant temperature of 45 °C. The temperature is raised above room temperature for increased thermal radiation, resulting in measurements with more dynamic range.

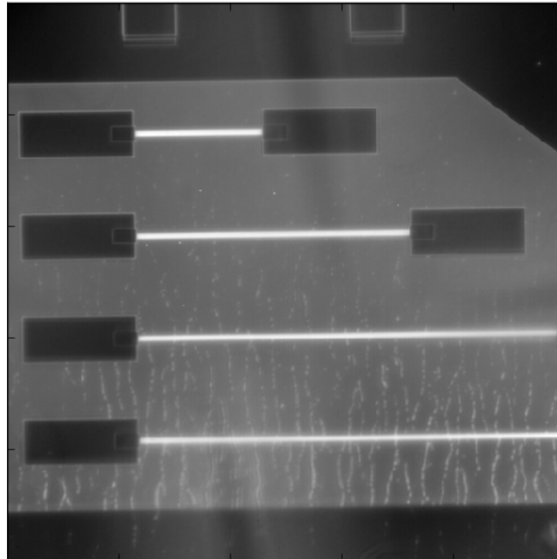

Figure 2.22: Image taken with the infrared camera of the sample at uniform temperature of 45 °C. The area depicted is 1 mm × 1 mm.

Figure 2.22 shows an image taken with the infrared camera of a sample at uniform temperature. The different materials can be discerned because of their different emissivities $\epsilon$. When measuring the temperature of a heated resistance, the radiation has to be corrected for the material emissivity. A reference image is first taken at a known uniform temperature, from which the emissivities are deduced. The resistance is then heated, and a new image is taken with the camera. The camera software directly displays the temperature at each pixel, calculated under the assumption that the emissivity does not change noticeably with the temperature increase.

### 2.2.2 Measurement of the thermal conductance

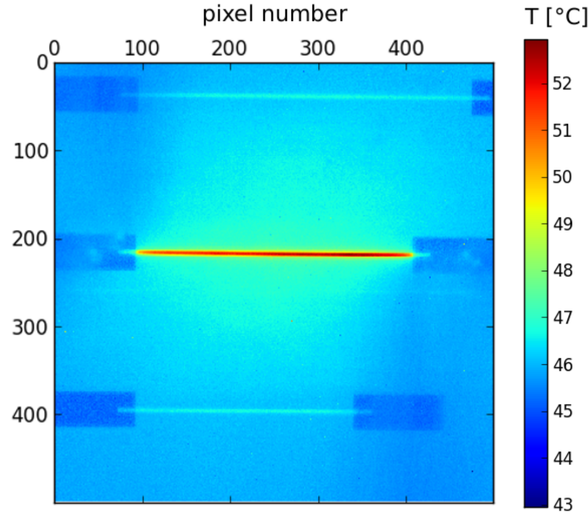


Figure 2.23: Temperature map measured by the infrared camera of a resistance of length 614 $\mu$m heated by a current of 20 mA (577 mW) on sample S2. The area depicted is 1 mm × 1 mm.

Energy loss due to radiation is negligible compared to the electrical power used to heat the resistance: Images from the infrared camera (figure 2.23) show that the area $A$ of temperature increase around a heated resistance is much smaller than 1 mm$^2$. The temperature $T_{\mathrm{r}}$ of the heated resistance itself rises by about 10 K to 55 °C. With a room temperature of $T_{\mathrm{RT}} \approx 20\,°\mathrm{C}$, the power radiated is smaller than $P = \epsilon\sigma A(T_{\mathrm{r}}^4 - T_{\mathrm{RT}}^4) \approx 0.2\,\mathrm{mW}$, ($\sigma$: Stefan-Boltzmann constant), while the resistances are heated by tens of mW.

Energy loss due to convection is also negligible: the energy loss is $P = hA(T_{\mathrm{r}} - T_{\mathrm{RT}})$, where $h$ is the convective energy transfer coefficient. Estimating $h \approx 10\,\mathrm{W/m^2K}$, and overestimating $A$ with 1 mm$^2$, $P \approx 0.35\,\mathrm{mW}$, much smaller than the electrical heating power.

The thermal conductance between the resistance and the bottom of the substrate is $G = P_{\mathrm{el}}/\Delta T$, where $\Delta T$ is the temperature difference measured with the infrared camera, and $P_{\mathrm{el}}$ is the electrical heating power, given by voltage and current obtained by four-wire sensing. The dependence of the thermal conductance on the length $l$ of the resistance is modeled by $G(l) = G_0 + lg$, where $g$ is the thermal conductance per unit length of the wire, and $G_0$ contains all border effects at the ends of the wire. This linear approximation is expected to hold well for long resistances, where a homogeneous temperature distribution is reached in the middle part of the resistance. As the shortest resistances are 100 $\mu$m long, 12.5 times longer than their width, the linear approximation holds well, see figure 2.24.

As the detector of the infrared camera is noisy, the temperature values of several pixels have to be averaged in order to get more precise measurements of the temperature of the resistance.
In a first approach, the temperature is determined by taking the highest average of three adjacent pixels on a line perpendicular to the resistance, going through the center of the resistance. This method depends on the orientation of the resistance with respect to the detector. In order to avoid this dependence, a second method based on numerically integrating the a $3\,\mu\text{m} \times 10\,\mu\text{m}$ large area in the center of the resistance, is investigated. Two dimensional spline interpolation of the thermal image is employed to always average the same area of the resistance, independent of the orientation of the detector.

The first measurements are carried out on resistances fabricated directly on semi-insulating substrates to verify the method. The samples investigated are a GaAs substrate ($415\,\mu$m thick), sample S1, and a diamond coated Si substrate ($10\,\mu$m diamond layer on 1 mm thick Si substrate), sample S2.
The two different methods of determining the temperature of the resistance are compared on the left in figure 2.24. While the temperatures differ between the two methods, the two regression lines have almost the same slope, $26.8 \pm 2.4\,\text{mW K}^{-1}\ \text{mm}^{-1}$ for the 3 px average, and $27.2 \pm 1.8\,\text{mW K}^{-1}\ \text{mm}^{-1}$ for the method based on interpolation and integration. Indeed, constant, purely additive systematic errors have no effect on the slope of the fit, which is the parameter used in this analysis.
The indicated uncertainty of the fit parameter is calculated from the statistics of the data points only. It is the variance $\sigma$ of the fit parameter, obtained under the assumption of Gaussian errors of the measured values around the fit line. In the following, only the temperatures obtained with the second method are indicated.

Figure 2.24 shows the measured data of samples S1 and S2; linear fits yield $g = 27.2 \pm 1.8\,\text{mW K}^{-1}\ \text{mm}^{-1}$ for S1 and $120.1 \pm 4.3\,\text{mW K}^{-1}\ \text{mm}^{-1}$ for S2. The thermal conductivity of the diamond coated Si substrate is more than a factor four higher than that of the GaAs substrate, evidencing its potential for improvement in thermal management of photoconductors.
The relative error is larger for the GaAs sample, because currents of only 10 mA and a base temperature of 30 °C were used in this first measurement. All subsequent measurements were performed at currents of 20 mA and a base temperature of 45 °C, resulting in a better signal-to-noise ratio in the detector.

In order to evaluate the effect of the bonding on the heat sink properties available to an active device, measurements are performed on LTG-GaAs layers after transfer to high con-

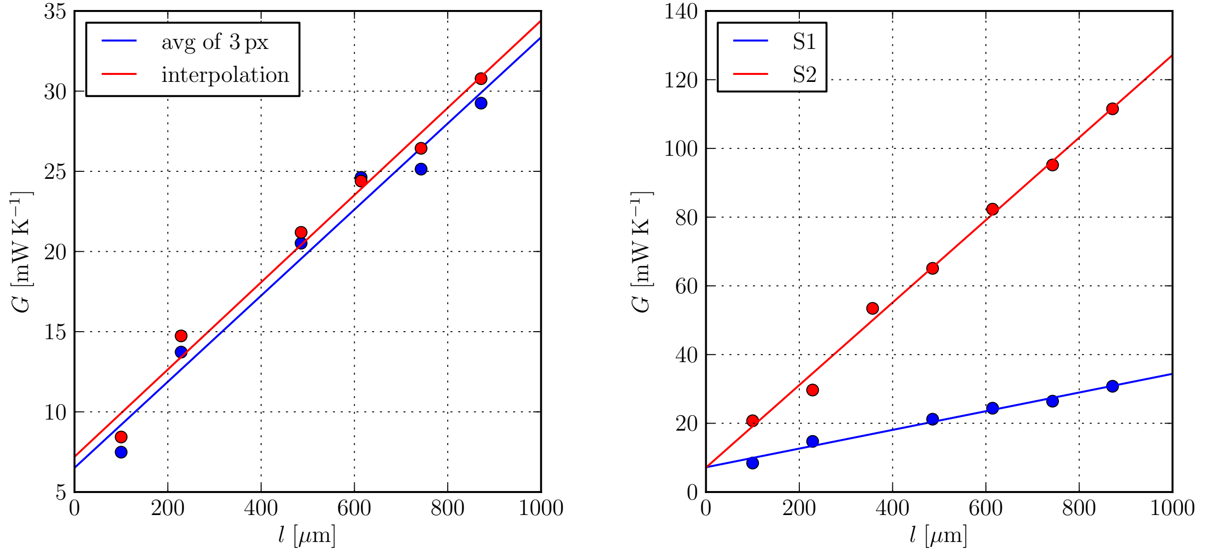


Figure 2.24: Left: comparison of the two methods of determining the temperature of the strip. Data is from sample S1. Right: Measured conductances $G(l)$ of GaAs (S1) and diamond-coated Si (S2) samples. Linear fits yield slopes of $g = 27.2 \pm 1.8\,\mathrm{mW\,K^{-1}\,mm^{-1}}$ for S1, and $g = 120.1 \pm 4.3\,\mathrm{mW\,K^{-1}\,mm^{-1}}$ for S2.

ductivity substrates.

Parts of one 250 nm thick epitaxial LTG-GaAs layer are bonded to a 250 $\mu$m thick Si substrate using a 900 nm thick In–Au SLID bonding layer (sample B1: 300 nm Au and 600 nm In; sample B2: 450 nm Au and 450 nm In), to a diamond coated Si substrate (sample B3), using the same bonding parameters as sample B1, and to Si using a 4.8 $\mu$m thick In–Au layer (sample B4). SEM images of the cross sections of the bonding layers of samples B1 and B3 are shown in figure 2.13, sample B2 is shown in figure 2.12, and sample B4 is shown in figure 2.25. Ti strips of thickness 100 nm, 8 $\mu$m wide and between 100 $\mu$m and 1000 $\mu$m long are fabricated, resulting in resistances between 130 Ω for the shortest and 1300 Ω for the longest strip.

All thermal measurements are performed at 45 °C base temperature. Currents of 20 mA are used to heat the five shorter resistances (100 $\mu$m to 614 $\mu$m long, 50 mW to 300 mW heating power), while the current is reduced to 10 mA for the three resistances between 743 $\mu$m and 1 mm (90 mW to 130 mW) in order to avoid breakdown of the LTG-GaAs layer due to excessive voltage, see also figure 2.26. From the measurements, parameter values of $g = 50.6$, 42.7, 58.1, and $39.9\,\mathrm{mW\,K^{-1}\,mm^{-1}}$ are deduced for samples B1 to B4, respectively (table 2.2).

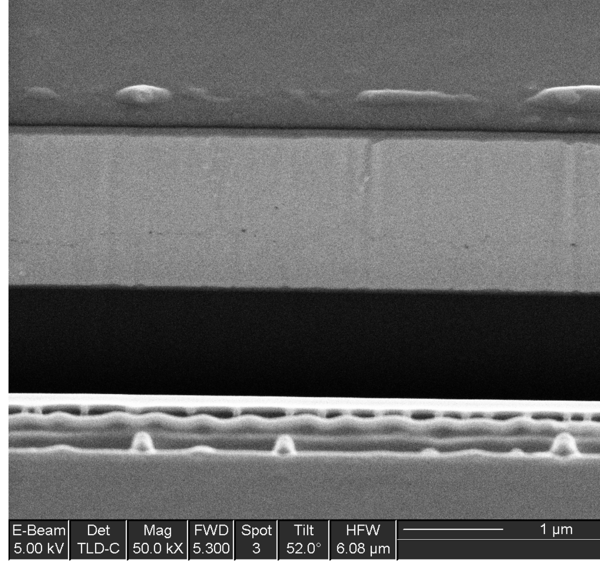


Figure 2.25: SEM image of FIB cut of sample B4, showing the 4.8 $\mu$m thick, In rich bonding layer.

### 2.2.3 Simulation of the thermal conductivities

In order to further evaluate the thermal conductivity of the bonding layer, a two dimensional model of the samples is created in the finite-element software Comsol. As shown in figure 2.27, only half the structure needs to be simulated for symmetry reasons. The bottom of the substrate is set to the base temperature $T_{\text{base}} = 45\,^{\circ}\text{C}$, and the heating strip temperature is set to $T_{\text{base}} + 2\,\text{K}$. All remaining borders are modeled as isolated; heat transfer takes place by conduction only. The width of the simulated substrate is chosen much larger than the height, 2000 $\mu$m for standard substrates and 4000 $\mu$m for the thicker diamond covered Si substrates. The thermal conductances obtained are essentially the same as for an infinitely wide substrate.
The power $p$ (mW/mm) transferred per unit length from the strip to the heatsink in steady state is given by integrating the $y$-component of the heat flux over any cross section of the structure in $x$-direction (see figure 2.27). The factor 2 in power transfer of the whole structure as compared to the simulated half structure is offset by the temperature difference of 2 K, and the thermal conductance per unit length of an infinitely long resistance is given by $g_{\text{simul}} = p/1\,\text{K}$.

For the simulation of sample S1 (strips directly on SI-GaAs substrate), only the substrate height and the thermal conductivity of GaAs, $k_{\text{GaAs}} = 46\,\text{W/K m}$ [15] is needed. The simulation results in a conductivity per unit length of $25.9\,\text{mW K}^{-1}\,\text{mm}^{-1}$, in good agreement with the measured value of $27.2 \pm 1.8\,\text{mW K}^{-1}\,\text{mm}^{-1}$. All simulations are summarized in

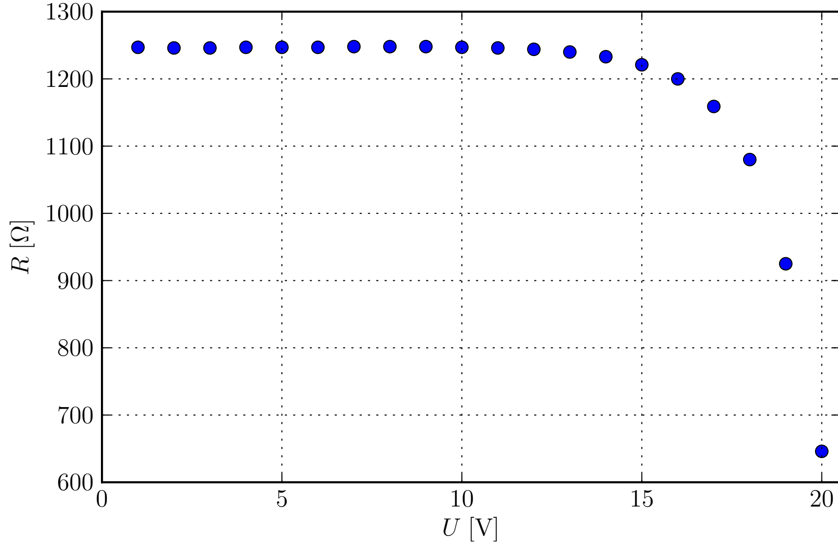


Figure 2.26: Measured resistance in dependence of the voltage for the longest resistance (1 mm) of sample B1. The resistance between the contact pads decreases with increasing voltage due to breakdown of the LTG-GaAs layer and conduction through the metallic bonding layer.

table 2.3.

Sample S2 is composed of a Si substrate ($k = 148\,\mathrm{W/K\,m}$) and a layer of polycrystalline diamond. By comparing simulation and experiment, a thermal conductivity of the diamond layer of $k_{\mathrm{Di}} = 600\,\mathrm{W/K\,m}$ is deduced. This is an effective thermal conductivity, which contains the effects of interface thermal resistances, which are not modeled in the simulation. The value is lower than that of crystalline diamond ($900 \ldots 2000\,\mathrm{W/K\,m}$ [16]), but appears reasonable for the polycrystalline layer.

Two parameters are necessary for the simulation of the bonded layers B1-B4: the conductivity of the bonding layer, $k_{\mathrm{bond}}$, and the conductivity of the bonded LTG-GaAs layer, $k_{\mathrm{LTG-GaAs}}$. Measurements by Jackson *et al.* [17] have shown that the high defect density of LTG-GaAs results in thermal conductivities of only 46% of the value of GaAs. A value of $k_{\mathrm{LTG-GaAs}} = 20\,\mathrm{W/K\,m}$ is therefore assumed for the simulations.

Samples B1 and B2 are very similar, except for the composition of the In–Au bond (higher Au content in sample B2). The measurements indicate a better thermal conductance of sample B1, as would be expected from the SEM images of the cross sections (figures 2.13 and 2.12).

Simulations agree with the experimental data if conductivities of the bonding layers of $13\,\mathrm{W/K\,m}$ (B1) and $8\,\mathrm{W/K\,m}$ (B2) are assumed. In the simulation, the bonding layer is

| Sample | $g$ [W/K m] | bond composition | substrate |
|---|---|---|---|
| S1 | $27.2 \pm 1.8$ | | GaAs (415 $\mu$m) |
| S2 | $120.1 \pm 4.3$ | | diamond (10 $\mu$m) coated Si (1mm) |
| B1 | $50.6 \pm 1.6$ | 300 nm Au – 600 nm In | Si (270 $\mu$m) |
| B2 | $42.7 \pm 1.2$ | 450 nm Au – 450 nm In | Si (270 $\mu$m) |
| B3 | $58.1 \pm 1.3$ | 300 nm Au – 600 nm In | diamond (10 $\mu$m) coated Si (1mm) |
| B4 | $39.9 \pm 1.8$ | 300 nm Au – 4500 nm In | Si (270 $\mu$m) |

Table 2.2: Measured thermal conductances of samples fabricated from the same 250 nm thick LTG-GaAs layer, transferred to different substrates using different bonding parameters. Samples S1 and S2 are included for comparison.

modeled as homogeneous, and no interface thermal resistances between layers or within the bonding layer are taken into account. The thermal conductivities used in the simulations are in fact effective thermal conductivities which model the thermal resistance composed of the actual thermal resistance of the bonding layer and the resistances of the interfaces.

The effective conductivities of the bonding layers are relatively low, well below that of indium (82 W/K m) or gold (320 W/K m), which is partly due to interface thermal resistances, and partly due to lower thermal conductivities of the alloys. Similar values have also been obtained by Kumar *et al.* [11]. The relatively large difference in the effective thermal conductivity of the bond of samples B1 and B2 underlines the importance of the correct material composition and process parameters during fabrication of the bond.
In the work by Kumar *et al.* [11], an effective thermal conductivity of 10 W/K m has been obtained for 2 $\mu$m thick In–Au bonds used in quantum cascade lasers at 120 K. As the thermal conductivity of the bonding layer is lower than that of the adjacent layers, the bonding layer acts as a thermal resistance, and it is preferable to employ thinner layers, as presented here. A sample similar to B1, but with a 2 $\mu$m thick bonding layer with $k_{\text{bond}} = 10\,\text{W/K m}$ would result in a thermal conductance of 32.9 mW K$^{-1}$ mm$^{-1}$.

Sample B3 uses the same diamond coated substrate as sample S2. The same thermal conductivities for diamond layer and silicon substrate are therefore used in the simulation. Also, the bond was fabricated using the same parameters as sample B1, hence the same thermal conductivity of 13 W/K m is used for the bonding layer, leaving no free parameter in the simulation. The simulated value of 56.2 mW K$^{-1}$ mm$^{-1}$ is in very good agreement with the experimentally obtained value of 58.1 mW K$^{-1}$ mm$^{-1}$, which confirms the conductivities obtained for the diamond and bonding layers, and also demonstrates the repeatability of the bonding process.

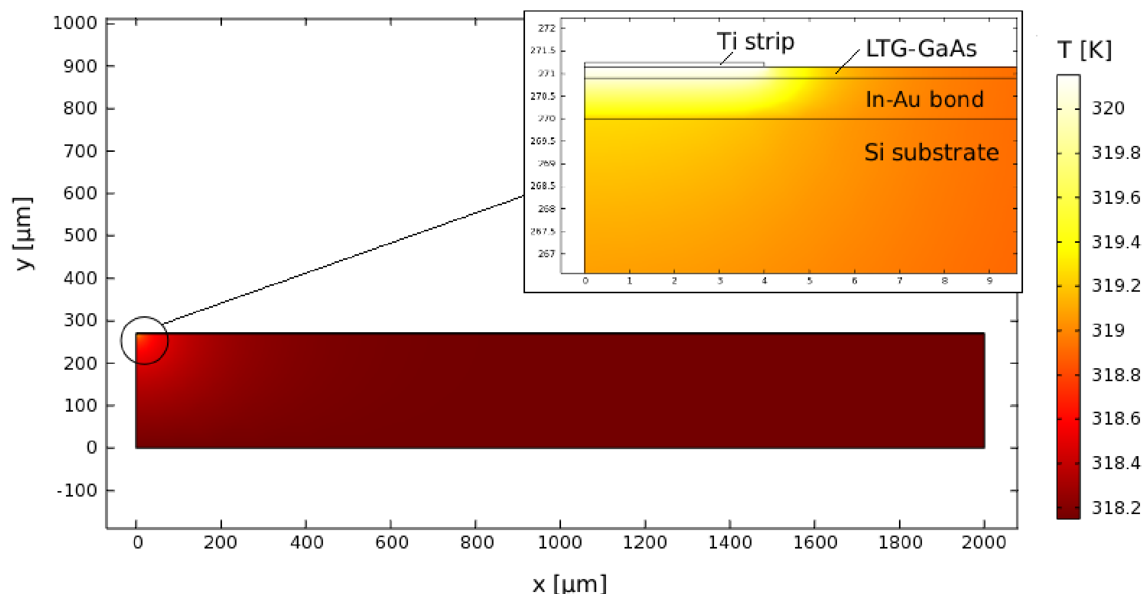


Figure 2.27: Temperature distribution in the simulated structure for sample S2. The simulation is performed in Comsol.

The indium rich thick bonding layer of sample B4 can be modeled with an effective thermal conductivity of 25 W/K m. This is much higher than the values of the other bonds, and is due to the larger thickness of the bonding layer: for a thicker bonding layer, the interface resistances contribute a smaller fraction of the total thermal resistance, and a higher effective conductivity is obtained when modeling bonding layer and interface resistances by an effective conductivity.

Despite the higher effective conductivity, the thermal resistance of the bonding layer of sample B4 is still higher because of the larger thickness, resulting in a lower thermal conductance of the sample. The effective thermal conductivity of the bonding layer is also still clearly lower than that of pure indium (82 W/K m) due to the thermal resistances across layer and bond boundaries.

In summary, good agreement between experiment and simulation has been obtained by modeling the bonding layer with a homogeneous, effective thermal conductivity, which comprises thermal resistances due to the interfaces and imperfect bonding. The values are strongly dependent on the bonding parameters.

All measured samples show higher conductances than would be expected from simulation for a similar LTG-GaAs layer on GaAs substrate (24.7 mW $K^{-1}$ $mm^{-1}$). The best conductances are obtained for relatively thin bonding layers, and are higher than those reported elsewhere

| Sample | $g_{\mathrm{exp}}$ [W/K m] | $g_{\mathrm{simul}}$[W/K m] | thermal conductivities [W/K m] |
|---|---|---|---|
| S1 | $27.2 \pm 1.8$ | 25.9 | $k_{\mathrm{GaAs}} = 46$ |
| S2 | $120.1 \pm 4.3$ | 122.9 | $k_{\mathrm{Di}} = 600$ |
| B1 | $50.6 \pm 1.6$ | 50.4 | $k_{\mathrm{bond}} = 13$ |
| B2 | $42.7 \pm 1.2$ | 42.1 | $k_{\mathrm{bond}} = 8$ |
| B3 | $58.1 \pm 1.3$ | 56.2 | $k_{\mathrm{bond}} = 13$, $k_{\mathrm{Di}} = 600$ |
| B4 | $39.9 \pm 1.8$ | 38.6 | $k_{\mathrm{bond}} = 25$ |

Table 2.3: Comparison of experimentally determined and simulated conductances. The thermal conductivities used in the simulations are $k_{\mathrm{Si}} = 148$ W/K m and $k_{\mathrm{LTG-GaAs}} = 20$ W/K m, in addition to those shown in the last column.

for In–Au SLID bonding [11].

The thermal conductivity of the bonding layer and the interface thermal resistances could not be deduced separated in this study, and only effective thermal conductivities were obtained. Samples with bonding layers of different thicknesses should allow to separate the interface resistances from the layer conductivities. However, it is expected that the fabrication of bonds with different thicknesses but the same process parameters would no result in layers with the same thermal conductivity due to different time scales of the diffusion processes during bonding.

### 2.2.4 Influence of the substrate conductivity on photoconductor output power

The influence of the thermal conductance of bonding layer and substrate on the maximum output power of a vertical photoconductor has been investigated by Dr. Emilien Peytavit [18]: One quarter of a 300 nm thick LTG-GaAs layer was transferred to a Si substrate using Au–Au thermocompression bonding. Another quarter of the same epitaxial layer was bonded to a SiC substrate using the same bonding parameters. Vertical photoconductors for on-wafer measurements were fabricated [19], and Ti strips for thermal measurements were also included on the mask, although only four different lengths were fabricated due to limited space on the wafer. Also, the Ti strips were metallized at the same time as other components of the wafer, to reduce the number of processing steps, and were therefore only 20 nm thick.

At voltages above 10 V, the measured electrical resistance decreases rapidly, due to breakdown of the LTG-GaAs layer and conduction in the metallic bond, see figure 2.28. Due

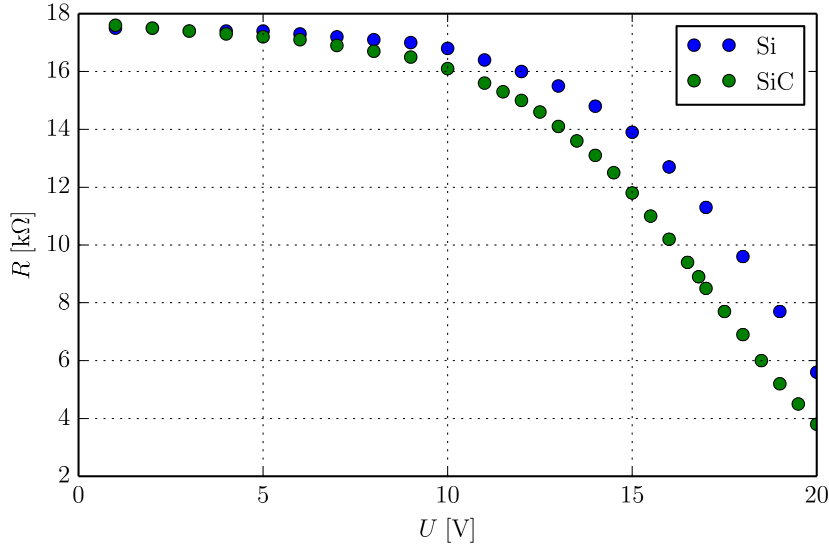


Figure 2.28: Measured resistance in dependence of the voltage for the longest resistances (1 mm) on the Si and SiC samples.

to the low thickness of the resistances, the currents at 10 V are only about 2.5 mA for the smallest resistances, and smaller for the longer resistances. The low temperature increase of less than 1 K could not be measured with sufficient precision to allow for the same analysis as has been done for the other samples. However, at the same currents, the temperature increases are clearly lower for the SiC sample. Table 2.4 shows the values measured for the smallest resistance (229 $\mu$m long) at 2 mA and 2.5 mA. The conductance of the SiC sample is approximately 80% higher than that of the Si sample, proving the influence of the substrate conductivity on the conductance of the whole stack, across epitaxial and bonding layers.

| | Si | | SiC | | |
|---|---|---|---|---|---|
| $I$ [mA] | $P$ [mW] | $\Delta T$ [K] | $P$ [mW] | $\Delta T$ [K] | $g_{\text{SiC}}/g_{\text{Si}}$ |
| 2.0 | 16.0 | 0.95 | 16.4 | 0.53 | 1.84 |
| 2.5 | 24.9 | 1.51 | 25.4 | 0.88 | 1.74 |

Table 2.4: Measured heating power $P$ and temperature difference $\Delta T$ of the two samples at 2 mA and 2.5 mA, corresponding to voltages of approximately 8 V and 10 V. The conductances are $g = P/\Delta T$.

On-wafer measurements of the maximum THz output power of the photoconductors before destruction have been performed by Dr. Emilien Peytavit. However, despite the clearly

better heat dissipation of the SiC sample over the Si sample, no significant increase in the maximum THz output power could be measured [18]. Similar behavior has been observed by Verghese *et al.* [15], when the maximum input power before destruction was measured at various temperatures between 77 K and 290 K. It was found that device failure did not depend on the absolute temperature of the device, but rather on the temperature gradient at the surface of the device. This has been attributed to thermal fracture as a result of residual strain in the epitaxial layers.

A study of the long-term reliability of LTG-GaAs photoconductors has been undertaken by Göbel *et al.* [20]. A clear correlation of device lifetime and operating temperature has been found. However, all tested devices had the same thermal conductance, and therefore the operating temperature was given directly by the input power.

It would be interesting to investigate the dependence of the long-term failure mechanism on the absolute device temperature, i.e. to compare the average lifetimes of the SiC and Si photoconductors at the same input power below the immediate failure, where the SiC devices operate at lower temperatures. Another intriguing experiment would be the mapping of the device temperature during operation, for example by micro-Raman thermometry [21], which could measure the temperature at which failure occurs, and could identify possible hot spots in the device.

## 2.3 Summary

The use of indium for low temperature wafer bonds has been explored. While In–In thermocompression bonds can be fabricated at very low temperatures, they are not stable at temperatures above 160 °C, limiting the processing steps available after bonding.

Solid-liquid interdiffusion bonding using the In–Au system has also been investigated. The process parameters have been optimized, and very high quality bonds have been achieved at 200 °C. It has been shown that Pt is an effective diffusion barrier for the In–Au system, which allowed to optimize the optical properties independently from the bond. Attempts at etching the In–Au bond have not been successful, the main difficulty being the different etch speeds of the various In–Au compounds.

The thermal characteristics of transferred LTG-GaAs layers have been investigated. A measurement method based on an infrared camera has been developed, and it has been shown that the optimized In–Au bonding parameters produce samples with higher thermal conductance than bonds with higher Au content. The effectiveness of a diamond heat

spreader on the substrate has also been demonstrated (factor 4 increase of diamond coated Si substrate over GaAs substrate). Through comparison with simulations, an effective thermal conductivity of the bonding layer of 13 W/K m for a 900 nm thick layer has been deduced, which is higher than the values found for In–Au bonds in the literature.

It has also been shown that the photoconductors wafer-bonded to SiC substrate fabricated by Dr. Emilien Peytavit have a 80% higher thermal conductance than those transferred to Si substrate. Preliminary results seem to indicate that the maximum THz output power of the SiC photoconductors is not higher than that of Si photoconductors. However, further studies are necessary to confirm this preliminary finding.

# Bibliography

[1] E. Peytavit, C. Coinon, J.-F. Lampin, *A metal-metal Fabry-Pérot cavity photoconductor for efficient GaAs terahertz photomixers*, Journal of Applied Physics **109**, 016101 (2011)

[2] A. Ndèye, *Etude de développement de transistors bipolaires à hétérojonctions InP/GaAsSb reportés sur Si en vue de l'amélioration de la dissipation thermique*, PhD thesis, Université Lille 1 (2012)

[3] E. Peytavit, J.-F. Lampin, F. Hindle, C. Yang, G. Mouret, *Wide-band continuous-wave terahertz source with a vertically integrated photomixer*, Appl. Phys. Lett. **95**, 161102 (2009)

[4] D. Andrijasevic, M. Austerer, A. Andrews, P. Klang, W. Schrenk, G. Strasser, *Hybrid integration of GaAs quantum cascade lasers with Si substrates by thermocompression bonding*, Applied Physics Letters **92**, 051117 (2008)

[5] C. Tsau, S. Spearing, M. Schmidt, *Characterization of Wafer-Level Thermocompression Bonds*, Journal of Microelectromechanical Systems **13**, 963 (2004)

[6] B. S. Williams, S. Kumar, Q. Hu, J. L. Reno, *Operation of terahertz quantum-cascade lasers at 164 K in pulsed mode and at 117 K in continuous-wave mode*, Optics Express **13**, 3331 (2005)

[7] L. Bernstein, *Semiconductor joining by the solid-liquid-interdiffusion (SLID) process*, Journal of the electrochemical society **113**, 1282 (1966)

[8] C. C. Lee, C. Y. Wang, G. Matijasevic, *Au-In bonding below the eutectic temperature*, IEEE Transactions on components, hybrids, and manufacturing technology **16**, 311 (1993)

[9] F. Shieu, C. Chen, J. Sheen, Z. Chang, *Intermetallic phase formation and shear strength of Au-In microjoint*, Thin solid films **346**, 125 (1999)

[10] V. Simić, Ž Marinković, *Thin film interdiffusion of Au and In at room temperature*, Thin solid films **41**, 57 (1977)

[11] S. Kumar, B. S. Williams, S. Kohen, Q. Hu, J. L. Reno, *Continuous-wave operation of terahertz quantum-cascade lasers above liquid-nitrogen temperature*, Appl. Phys. Lett. **84**, 2494 (2004)

[12] B. S. Williams, S. Kumar, H. Callebaut, Q. Hu, J. L. Reno, *Terahertz quantum-cascade laser at* $\lambda \approx 100\,\mu$m *using metal waveguide for mode confinement*, Appl. Phys. Lett. **83**, 2124 (2003)

[13] I. Petrov, P. Barna, L. Hultman, J. Greene, *Microstructural evolution during film growth*, Journal of Vacuum Science & Technology **21**, S117 (2003)

[14] J. H. Park, *Microstructure development and evolution of sputter deposited indium thin films in cryogenics*, Master thesis, Auburn University (2007)

[15] S. Verghese, K. A. McIntosh, E. R. Brown, *Optical and terahertz power limits in the low-temperature-grown GaAs photomixers*, Appl. Phys. Lett. **71**, 2743 (1997)

[16] L. Wei, P. Kuo, R. Thomas, T. Anthony, W. Banholzer, *Thermal Conductivity of Isotopically Modified Single Crystal Diamond*, Physical Review Letters **70**, 3764 (1993)

[17] A. W. Jackson, J. P. Ibbetson, A. C. Gossard, U. K. Mishra, *Reduced thermal conductivity in low-temperature-grown GaAs*, Appl. Phys. Lett. **74**, 2325 (1999)

[18] E. Peytavit, *private communication*

[19] E. Peytavit, C. Coinon, J.-F. Lampin, *Low-Temperature-Grown GaAs Photoconductor with High Dynamic Responsivity in the Millimeter Wave Range*, Appl. Phys. Express **4**, 104101 (2011)

[20] T. Göbel, D. Schoenherr, C. Sydlo, M. Feiginov, P. Meissner, H. Hartnagel, *Reliability investigation of photoconductive continuous-wave terahertz emitters*, IEEE Transactions on microwave theory and techniques **59**, 2001 (2011)

[21] T. Beechem, A. Christensen, S. Graham, D. Green, *Micro-Raman thermometry in the presence of complex stresses in GaN devices*, Journal of Applied Physics **103**, 124501 (2008)

# 3 Materials for photoconductors operating at wavelengths above 1 µm

## 3.1 Short carrier lifetime materials for photoconductors at wavelengths above 1 µm

Low temperature grown GaAs (LTG-GaAs) presents ideal properties for THz photoconductors: Very high dark resistivity ($1{\cdot}10^7\,\Omega$cm [1]), short carrier lifetime ($< 0.3$ ps [2]), and high electrical breakdown field ($1 \cdot 10^5\,\mathrm{V\,cm^{-1}}$ [3]). However, due to the bandgap of GaAs of 1.42 eV, LTG-GaAs photoconductors are used with 850 nm or shorter wavelength lasers. Many efforts have been undertaken to find materials suitable for photomixing with lasers at longer wavelengths in order to use the better developed, cheaper, and more compact sources and components at 1.55 $\mu$m telecom wavelengths. Also, higher efficiency photomixers are theoretically possible due to the lower photon energy of 0.8 eV as compared to 1.55 eV for photons with 800 nm wavelength.

In order to obtain short carrier lifetimes below 1 ps, the materials are either grown at low temperature similar to LTG-GaAs, doped during growth, irradiated or implanted with ions after growth, or through incorporation of nanoparticles. While all of these methods have been successful in creating short carrier lifetimes, the main problem of the small bandgap materials remains the dark resistivity, which should be high for photoconducting applications.

### 3.1.1 InGaAs-based materials for THz photoconductors

One much investigated material for 1.5 $\mu$m THz photoconductors is InGaAs. $In_{0.53}Ga_{0.47}As$, lattice matched to InP, has an energy gap of 0.74 eV, below the 0.8 eV photon energy of a 1.55 $\mu$m laser, and high electron mobilities around $10^4\,\mathrm{cm^2\,V^{-1}\,s^{-1}}$, making it an interesting candidate for THz photoconductors.

### Low temperature grown InGaAs

Following the success of low temperature growth followed by annealing in creating low carrier lifetime and high resistivity in GaAs, naturally the first try of making InGaAs compatible with THz applications was low temperature growth [4, 5]. Similar to LTG-GaAs, growth of $In_{0.53}Ga_{0.47}As$ at low temperatures under excess As flux results in the incorporation of the excess As in the material under formation of $As_{Ga}$ antisites and other defects.

These defects act as recombination centers, reducing the carrier lifetime to the order of 1 ps. However, their activation energy is only 30-40 meV, and their concentration increases with decreasing growth temperature. The low activation energy means that a large part of the n-type donor defects are ionized at room temperature, resulting in a very low dark resistivity which decreases further with decreasing growth temperature [5, 6]. Moreover, post-growth annealing results in increased charge carrier lifetimes and no increase in dark resistivity.

In order to improve the dark resistivity, compensation of residual charge carriers through Be p-doping has been investigated. In InGaAs/InAlAs multiple quantum wells, a Be concentration of $2 \cdot 10^{18}\,\text{cm}^{-3}$ resulted in a residual carrier concentration of $6.3 \cdot 10^{15}\,\text{cm}^{-3}$ as compared to $8.8 \cdot 10^{17}\,\text{cm}^{-3}$ for undoped $In_{0.53}Ga_{0.47}As$ grown at 210 °C [7]. Furthermore, annealing of Be doped samples at 600 °C further reduces the charge carrier lifetime. An electron lifetime well below 1 ps has been reported for highly doped samples with Be doping concentrations above $2 \cdot 10^{20}\,\text{cm}^{-3}$ [8]. This short lifetime was due to the Auger recombination process and the material is not usable for high dark resistivity applications.

As the bandgap of $In_{0.53}Ga_{0.47}As$ lattice matched to InP is slightly smaller than the photon energy at 1.55 $\mu$m, it is possible to reduce the indium content in order to adjust the bandgap to the photon energy, at the expense of introducing a lattice mismatch with respect to the InP substrate. LTG-$In_xGa_{1-x}As$ with indium content varying between $0.45 \leq x \leq 0.53$ has been studied by Takazato *et al.* [9]. The larger bandgap of the $x = 0.45$ material resulted in an increase of the resistivity from 170 Ωcm to 760 Ωcm. But this relatively high resistivity for an LTG-InGaAs material could be achieved also because of the low Hall mobility of only $26\,\text{cm}^2\,\text{V}^{-1}\,\text{s}^{-1}$. Dipole antennas with a gap of 5 $\mu$m and a width of 10 $\mu$m were fabricated on this material and used for THz emission and detection under pulsed excitation at 1.55 $\mu$m. The emitted spectrum recorded with a LTG-GaAs based receiver extended over 3 THz with a peak signal to noise ratio of 54 dB. Using the same InGaAs-based antenna as detector, the spectrum was reduced to 2.5 THz and the signal to noise ratio to 45 dB [10]. The limitation was the higher detector noise due to the higher conductivity material.

Higher resistivities can be expected by further reducing the indium content and thus further

increasing the bandgap. It has been shown that 500 fs lifetime and resistivities of $10^4\,\Omega$cm can be achieved in undoped LTG-$In_{0.3}Ga_{0.7}As$ grown on GaAs substrates at 180 °C and annealed at 450 °C [11]. This composition is suitable for use with Nd:glass pulsed lasers or with Ytterbium (Yb:$CaF_2$) cw lasers around 1.05 $\mu$m, avoiding the expensive and bulky Ti:sapphire lasers usually employed with LTG-GaAs based photoconductors.

By combining low temperature growth and Be p-doping ($10^{18}\,cm^{-3}$) of InGaAs with 23% In content, a lifetime of 4.7 ps and sufficiently high resistivity for cw THz generation has been obtained. Using spiral antennas without interdigitated finger contacts, up to 2 THz could be generated, which was limited by the tuning range of the dual-frequency laser [12]. The output power remained well below 1 $\mu$W in the measured range from 150 GHz to 2 THz, the main limitation being a high dc photocurrent due to a long hole lifetime, and low thermal conductivity of photoconductor and the metamorphic substrate. The metamorphic substrate consisted of a several $\mu$m thick $In_xGa_{1-x}As$ layer with gradient from $x = 0$ to $x = 23\%$ and was necessary for lattice matched growth of the photoconductor material on GaAs substrate.

### Ion irradiated InGaAs

Instead of incorporating the defects necessary for a short charge carrier lifetime by low temperature growth of the material, defects can also be introduced post-growth by ion irradiation. During irradiation, the semiconductor is bombarded with high energy ions. While traversing the semiconductor, ions collide with host atoms, resulting in displacements of the host atom. Due to the high energy of the irradiating ions, the displaced host atoms have enough energy to create further defects, resulting in defect cascades. The initial energy of the ions is chosen so that ions are not stopped in the active layer, but cross it completely, leaving only intrinsic defects related to host atom displacements in the semiconductor, and no doping of the semiconductor occurs. The defects can act as trap and recombination centers for free charge carriers, thus reducing their lifetime [13]. The defect clusters created by heavy ion radiation are thermally stable, while point defects created by light ion radiation are recovered by annealing at 600 °C [14].

It has been shown that a sub-picosecond lifetime can be achieved by irradiating $In_{0.53}Ga_{0.47}As$ with $Au^+$ [15] or $Br^+$ [16] ions. The resistivity of the resulting material was 0.63 $\Omega$cm in the $Au^+$ case and 3 $\Omega$cm in the $Br^+$ irradiated $In_{0.53}Ga_{0.47}As$. Despite the low resistivity, the $Br^+$ irradiated material has been successfully used to generate THz radiation above 2 THz in a pulsed experiment with a dipole antenna [16] as well as by photomixing with an interdigitated planar photoconductor coupled to a spiral antenna [17]. THz generation

with a TEM horn antenna connected to a 2.5 µm wide photoconductive gap has also been reported [18]. Continuous wave output powers from the spiral antenna of 45 nW at 430 GHz and 10 nW at 1 THz have been measured with a liquid helium cooled bolometer. Higher output powers have been achieved with the horn antenna: 380 nW at 200 GHz and 100 nW at 700 GHz.
These values remain however lower than those obtained by similar LTG-GaAs based photoconductors due to the low bias voltage of 1.5 V, which is a consequence of the low material resistivity. The photocurrent close to destruction is also lower than expected, suggesting degraded mobility in the irradiated InGaAs.

### Ion implanted InGaAs

Ion implantation in semiconductors can be done similar to irradiation by choosing an initial energy low enough so that the ions lose all their kinetic energy through collisions with host atoms and remain in the active layer. The defects generated by collisions are similar to those from irradiation, but with smaller cascades and additional impurities created by the implanted ions.

While irradiation can result in homogeneously distributed defects if the ion energy loss is negligible in the active layer, ion implantation results in a non-homogeneous ion distribution that can be approximated by a Gaussian-like distribution. Since most ions are stopped in the semiconductor, the irradiation damage is higher near the surface than deeper in the material and can lead to an amorphous layer close to the surface [19]. Annealing of the semiconductor is usually necessary after implantation to allow the implanted ions to reach substitutional sites and become electrically active.

$Fe^+$ implantation of $In_{0.53}Ga_{0.47}As$ can reduce the carrier lifetime to sub-picosecond values [20]. Deep levels in $Fe^+$ implanted InGaAs are due to defects in the crystal lattice caused by the ion bombardment, and due to the Fe atoms implanted into the crystal. The native defects are donor levels with activation energy of 30-40 meV [5], resulting in a low resistivity. Fe atoms incorporated in InGaAs behave like deep acceptors with energy levels of 350 meV [21, 22], shifting the Fermi level towards the midgap and increasing the resistivity.

Implantation of $Fe^+$ ions with energies of 2 MeV into a 1.5 µm thick $In_{0.53}Ga_{0.47}As$ layer has been studied by Carmody *et al.* [20]. At an implantation dose of $1 \cdot 10^{15}\,\mathrm{cm}^{-2}$ and after annealing at 500 °C for 30 s, a sheet resistance of $4 \cdot 10^5\,\Omega$ and 300 fs carrier lifetime have been reached.

Pulsed THz emission and detection based on $Fe^+$-implanted $In_{0.53}Ga_{0.47}As$ photoconductors

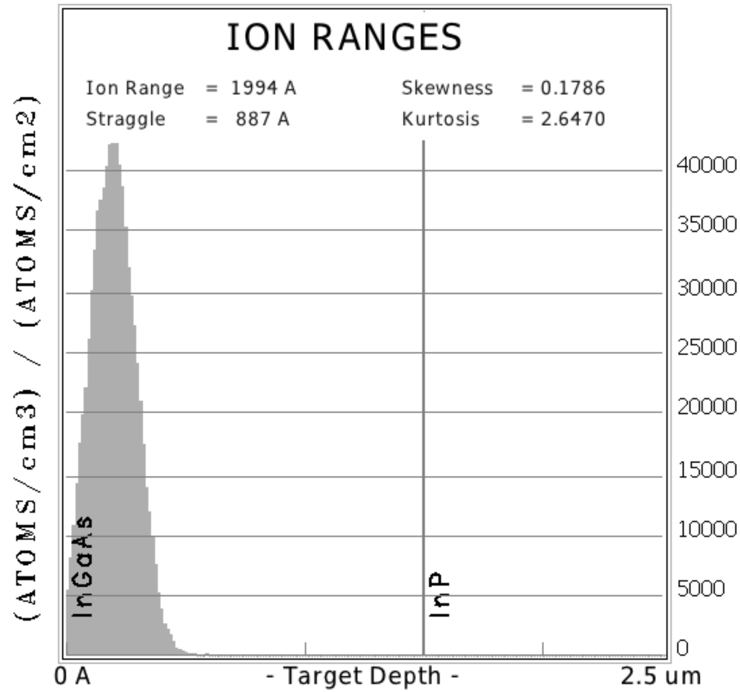


Figure 3.1: Simulated distribution of implanted Fe-atoms in the configuration used by Suzuki *et al.* [19]: The ion energy was 340 keV and the target was a 1.5 $\mu$m thick $In_{0.53}Ga_{0.47}As$ layer on InP substrate. The dose was $1 \cdot 10^{15}$ cm$^{-2}$, giving a peak Fe concentration of $4 \cdot 10^{19}$ cm$^{-3}$. The simulation was performed using the SRIM software [24].

have been reported by Suzuki *et al.* [19, 23]. The photoconductors used were made on a 1.5 $\mu$m thick $In_{0.53}Ga_{0.47}As$ layer grown on semi-insulating InP substrate by metalorganic chemical vapor deposition. The material was implanted with $Fe^+$ ions with 340 keV energy at a dose of $1 \cdot 10^{15}$ cm$^{-2}$. This resulted in a 0.3 $\mu$m thick amorphous layer at the surface, and little damage at depths larger than 0.5 $\mu$m, see figure 3.1. A sheet resistance of 6.3 k$\Omega$ has been obtained. Annealing between 400 °C and 640 °C reduced the sheet resistivity because of recrystallization of the amorphous layer [23]. This is in contrast to the results obtained by Pearton *et al.*, who observed a 3 order of magnitude increase in resistivity by annealing between 300 °C and 600 °C [22].

Iron atoms can also be incorporated in InGaAs by doping during growth by metal-organic chemical vapor deposition instead of post-growth implantation [25]. A resistivity of $2.2 \cdot 10^3$ $\Omega$ cm has been obtained for a 1 $\mu$m thick InGaAs layer grown with a doping concentration of $2 \cdot 10^{16}$ cm$^{-3}$ [26]. No charge carrier lifetimes have been reported, but pulsed THz generation up to 2.5 THz has been demonstrated.

### 3.1.2 Other materials for THz photoconductors

#### Superlattices

Another method of producing short carrier lifetimes is by creating a superlattice of two or more materials instead of using one bulk material. One layer in the superlattice is for the absorption of light, while the other layer is for carrier trapping and recombination. The advantage of this approach is that the absorbing layer does not need to have a short lifetime and can thus be as defect-free as possible, resulting in a high mobility. The lifetime of the material is given by the time it takes photogenerated charge carriers to reach the recombination layer and can be tailored by changing the thickness of the absorption layer. For a short lifetime material, the absorption layer has to be thin ($\sim 100\,\mathrm{nm}$). In order to get sufficient absorption of light, several repetitions of absorption and recombination layer are grown, resulting in a superlattice.

The first proposed superlattice was GaAs with ErAs recombination layers [27]. During epitaxial growth of GaAs, thin layers of ErAs are incorporated. ErAs growth on GaAs results in self-assembled nanometer-sized islands which act as recombination centers. Charge carrier lifetimes as short as 120 fs have been reported.

The same type of ErAs island growth can also be applied to $In_{0.53}Ga_{0.47}As$ for operation at $1.55\,\mu\mathrm{m}$ [28]. In this case, however a low resistivity n-type material is obtained. Driscoll *et al.* have therefore Be doped the ErAs layers, shifting the Fermi level towards midgap and increasing the resistivity up to $350\,\Omega\mathrm{cm}$. [29]
THz radiation up to 3 THz has been generated in a pulsed experiment using this material [30]. The bandwidth was almost independent of the charge carrier lifetime, which was investigated from 0.2 to 6.3 ps, and the limitation was likely the rise time of the pump pulse.

A superlattice composed of LTG-InGaAs and InAlAs layers has been studied by Sartorius *et al.* [6]. Electrons in 12 nm thick LTG-InGaAs layers can tunnel into adjacent 8 nm thick InAlAs layers where they are trapped thanks to native deep levels. In this way the InAlAs layers improve the dark resistivity of the superlattice as compared to bulk LTG-InGaAs by several orders of magnitude [6].
Antennas fabricated on this superlattice material have been used as detectors in cw systems, where the THz radiation was generated by a waveguide-fed photodiode [31]. Water vapor absorption lines were detected up to 1.6 THz.
Mesa etching of the active area allowed for contact placement at the sides of the superlattice structure and for better isolation of the bias lines [32]. The output power in pulsed operation reached $1.24\,\mu\mathrm{W}$ on average with a repetition rate of 100 MHz. The good resistivity of the

material and the isolation of the bias lines allowed for sensitive detectors. A THz time domain system based on such photoconductors both for emission and for detection showed a frequency spectrum exceeding 4 THz.

### InGaAsP

One very promising material for THz photoconductors at 1.55 $\mu$m has been presented quite recently by Fekecs *et al.* [33]: low temperature Fe-implanted InGaAsP. Two main improvements over earlier Fe-implantation works have been developed to increase the material resistivity: The material used is $(\mathrm{In_{0.53}Ga_{0.47}As})_\mathrm{y}(\mathrm{InP})_{1-\mathrm{y}}$, allowing to tune the bandgap to 0.8 eV by changing the composition $y$ while remaining lattice matched to the InP substrate. Also, Fe-implantation was done at low temperatures of 83 K, which reduces defect annealing during implantation. The implantation was done at multiple energies between 0.25 and 2.5 MeV to improve homogeneity. After annealing for 30 s between 500 °C and 600 °C, resistivities above 1200 Ωcm and charge carrier lifetimes below 3 ps were obtained.
Pulsed THz generation using dipole antennas has been demonstrated up to 2 THz, and was likely limited by the detector setup.

The same authors have also presented Fe-implanted $\mathrm{In_{0.72}Ga_{0.28}As_{0.61}P_{0.39}}$ for use with 1.3 $\mu$m lasers [34]. Resistivities of $1.4{\cdot}10^4$ Ωcm and Hall mobilities of 400 $\mathrm{cm^2\,V^{-1}\,s^{-1}}$ with low carrier concentrations of $1{\cdot}10^{12}\,\mathrm{cm^{-3}}$ have been reported, but so far no lifetime measurements or THz generation have been published.

### LTG-GaAsSb

Low-temperature grown GaAsSb with Sb content between 15% and 20% for applications with 1.05 $\mu$m lasers has been studied by Wallart *et al.* [35]. Picosecond lifetimes and resistivities exceeding $1 \cdot 10^3$ Ωcm with good mobility above 300 $\mathrm{cm^2\,V^{-1}\,s^{-1}}$ have been obtained with the proper growth conditions at 280 °C. Annealing at 600 °C strongly reduced the resistivity to 25 Ωcm.

Compositions with 40% and 85% Sb have been investigated by Sigmund *et al.*. THz generation up to 1 THz by pulsed excitation have been demonstrated for the 40% Sb material, which showed sufficiently high resistivity after 600 °C annealing [36]. However, the bandgap corresponds to 1.44 $\mu$m, below the telecom wavelength at 1.55 $\mu$m. Annealing of the sample with 85% Sb did not result in a high resistivity material, but rather decreased the resistivity [37].

CW operation up to 0.4 THz from GaAsSb has also been reported from an interdigitated finger photoconductor integrated with log-periodic spiral antenna [38]. The bandgap of the material was 1 eV, and the lifetime 700 fs.

#### LTG-GaBiAs

The bandgap of GaAs can also be reduced by the incorporation of Bi. One of the advantages of the GaBiAs ternary compound is that the bandgap changes rapidly with Bi content, and only 6% Bi content is necessary for material excitation at 1.3 $\mu$m. On the other hand, low growth temperatures are necessary in order to avoid surface accumulation of the large Bi atoms [39]. A photoconductive emitter with a 20 $\mu$m gap fabricated on $GaBi_xAs_{1-x}$ with $x = 8\%$ showed pulsed emission up to 4 THz [40]. The GaBiAs layer had a resistivity of $10^4\,\Omega$cm. A detector based on a sample with $x = 6\%$ was used to coherently detect THz pulses [41]. It was shown that the detector is most sensitive when excited with 1.1 $\mu$m to 1.3 $\mu$m pulses, but has been demonstrated to also work with 1.55 $\mu$m pulses.

#### LTG-GaAsSbN

A very high resistivity above $10^7\,\Omega$cm was also reported for the quarternary LTG-GaAsSbN after *in situ* annealing at 600 °C [42]. The material had a content of 5% N and 12% Sb, and a picosecond carrier lifetime ($\sim$ 1.3 ps). The absorption coefficient was $2000\,\mathrm{cm^{-1}}$ at 1.55 $\mu$m, with a cut-off wavelength of 2.1 $\mu$m. The Hall mobility was only $\sim 6\,\mathrm{cm^2\,V^{-1}\,s^{-1}}$, which partly explains the high resistivity. No THz generation based on this material has been reported so far.

### 3.1.3 Summary

Many materials have been investigated for photoconductors working at wavelengths above 1 $\mu$m, including low-temperature growth of various ternary and quaternary semiconductors, superlattices, irradiation and implantation, and combinations thereof. Several methods were successful in reducing the carrier lifetime to picosecond values or shorter. However, as evidenced in table 3.1, no material has been found yet that combines the high dark resistivity, short carrier lifetime, and relatively high mobility of LTG-GaAs.

Materials absorbing at 1.55 $\mu$m are preferred for photoconductors because of the cheap optical components at this wavelength, and because of the higher number of photons at the same optical powers. However, the materials investigated so far have low resistivities

| Material | $\rho$ (Ohm cm) | $\mu$ (cm$^2$ V$^{-1}$ s$^{-1}$) | $\tau$ (ps) |
|---|---|---|---|
| LTG-GaAs (0.85 $\mu$m) [1, 3, 2] | $1{\cdot}10^7$ | 200 | $< 0.3$ |
| LTG-$In_{0.53}Ga_{0.47}As$ [10] | 170 | 28 | ··· |
| $Au^+$ irradiated InGaAs [15] | 0.63 | 1360 | 0.9 |
| $Br^+$ irradiated InGaAs [16] | 3 | 490 | 0.2 |
| 2 MeV $Fe^+$ implanted InGaAs [20] | *60* | 100 | 0.3 |
| 340 keV $Fe^+$ implanted InGaAs [19] | *0.9* | 1500 | ··· |
| 50...400 keV $Fe^+$ implanted InGaAs [22] | 5 | ··· | ··· |
| Fe doped InGaAs [25] | 2200 | ··· | ··· |
| Fe implanted InGaAsP [33] | 2500 | 400 | 0.3 |
| ErAs:InGaAs [43] | *500* | 202 | $< 0.3$ |
| InGaAs-InAlAs superlattice [31] | *200* | ··· | ··· |
| Fe implanted InGaAsP (1.3 $\mu$m) [34] | $1.4{\cdot}10^4$ | 400 | ··· |
| LTG-GaAsSb (1.05 $\mu$m) [35] | 1350 | 300–1800 | 1 |
| LTG-GaBiAs (1.3 $\mu$m) [40] | $10^4$ | ··· | ··· |
| LTG-GaAsSbN (1.3…1.55 $\mu$m) [42] | $10^7$ | 6 | 1.3 |

Table 3.1: Summary of the most important material properties of short lifetime materials with bandgap below 1.24 eV (above 1 $\mu$m wavelength), with LTG-GaAs included for comparison. The wavelength corresponding to the bandgap is 1.55 $\mu$m unless indicated differently. Parameters for which no values were published are marked with "···". Resistivities in italics are calculated from data given in the publication, usually from sheet resistance and layer height, by $\rho = R_{\mathrm{sq}}h$. For the inhomogeneous layers of ion implanted samples this is an averaged value.

or very low mobilities. Materials with gaps at 1.3 $\mu$m or 1.05 $\mu$m have also been reported, for use with the optical sources available at these wavelengths. A higher dark resistivity is often obtained with these larger bandgap materials.

Generation of THz radiation has been demonstrated from several of the materials presented, but mostly from pulsed excitation. Very few reports of cw photomixing have been published, and the results were clearly lower than what has been achieved by photoconductors based on LTG-GaAs.

## 3.2 Fe-implanted InGaAs as material for a vertical photoconductor

In the preceding section several materials based on $Fe^+$-implantation of InGaAs have been presented. All InGaAs layers were more than 1 $\mu$m thick in order to absorb a sufficient

amount of light. Due to the nature of ion implantation, the material is not homogeneous over the whole thickness, and can range from amorphous near the surface to almost unchanged as-grown material close to the growth substrate [19]. Fe doping of InGaAs on the other hand results in homogeneous material, and good resistivities above 2000 Ωcm have been reported [25].

In this section, the feasibility of using a thin layer of $Fe^+$ implanted InGaAs in a vertical photoconductor configuration with light absorption in a resonant cavity is investigated. The thin layer allows a very homogeneous implantation profile with relatively little additional irradiation damage close to the surface. This was expected to result in a high resistivity material across the whole thickness of the layer.

Moreover, in the vertical configuration only a thin InGaAs layer with low thermal conductivity is used, and is in direct contact with a metallic heat spreading layer on a high thermal conductivity substrate. It can therefore be expected that a large dark current does not destroy the device as quickly as in interdigitated photoconductors.

In the following, the calculations and simulations performed to determine the layer thickness and ion implantation parameters are presented, followed by measurements of the charge carrier lifetime and of the electrical properties determined by the Hall effect.

### 3.2.1 Determination of the layer thickness

The vertical photoconductor as developed by Peytavit *et al.* [44] (see also figure 1.2) works with only a thin layer of absorbing material thanks to resonant absorption in a Fabry-Pérot cavity. Absorption in such a cavity depends on the thickness of the cavity and can change from a maximum to a minimum with only 100 nm thickness variation (see figure 3.2). The correct layer thickness is therefore crucial. In order to determine the layer thicknesses which yield maximum absorption, calculations are performed using a self developed code based on the transfer matrix method.

The transfer matrix method is often used for calculations of assemblies of thin films. A good introduction can be found in the book by Macleod [45], which served as a basis for the program. In the transfer matrix method, each layer is represented by a characteristic matrix describing the phase change of an electromagnetic wave and the impedance of the layer:

$$M = \begin{pmatrix} \cos(\delta) & i\sin(\delta)/\eta \\ i\eta\sin(\delta) & \cos(\delta) \end{pmatrix}$$

where $\delta = 2\pi N d/\lambda$ is the phase change of the wave when traversing the layer ($N$: complex index of refraction, $d$: layer thickness), and $\eta = N y_0$ is the admittance of the layer ($y_0 = \sqrt{\varepsilon_0/\mu_0}$: admittance of free space). The big advantage of the transfer matrix method is that the characteristic matrix can be calculated for each layer independently from the other layers. To calculate reflection and transmission of an assembly, the product of the characteristic matrices is calculated in the correct order:

$$\begin{pmatrix} B \\ C \end{pmatrix} = \left(\prod_{i=1}^{n} M_i\right) \begin{pmatrix} 1 \\ \eta_m \end{pmatrix} = M_1 M_2 \dots M_n \begin{pmatrix} 1 \\ \eta_m \end{pmatrix}$$

$M_1$ is the characteristic matrix of the layer adjacent to the medium of incidence, $M_n$ is the last layer, adjacent to the substrate with admittance $\eta_m$. Reflectance and transmittance of the assembly if illuminated from a medium with admittance $\eta_0$ can then be calculated using the parameters $B$ and $C$ (the complex conjugate of $x$ is denoted by $x^\star$):

$$R = \left(\frac{\eta_0 - C/B}{\eta_0 + C/B}\right)^\star \left(\frac{\eta_0 - C/B}{\eta_0 + C/B}\right)$$

$$T = \frac{4\eta_0 \mathrm{Re}(\eta_m)}{(\eta_0 B + C)^\star (\eta_0 B + C)}$$

The calculated reflectance at 1.55 $\mu$m of a stack composed of a 10 or 20 nm gold layer ($n = 0.18 - 10.21\,\mathrm{i}$) and an InGaAs layer ($\varepsilon = 12.865 - 0.7198\,\mathrm{i}$) on an optically thick gold layer (modeled as gold substrate) in dependence of the InGaAs layer thickness is shown in figure 3.2.

The calculations show that with a 10 nm thick top contact, the first minimum in reflectance occurs at $h_1 = 143$ nm and reaches almost zero reflectance, the second minimum is at $h_2 = 359$ nm with a reflectance of 8.6%. At the first minimum, close to 80% of the absorbed light is absorbed in the InGaAs layer. The minimum reflectance of the stack with 20 nm top contact is 28% at 160 nm while the second minimum at 375 nm reflects more than 50% of the light.

The influence of the height of the InGaAs layer on the reflectance of a stack with a 10 nm top gold layer is also measured experimentally. This allows to verify the calculated behavior, which depends on values for the refractive indices taken from the literature, and to demonstrate the feasibility of such a resonant cavity at 1.55 $\mu$m.

The setup used is sketched in figure 3.3. It is based on an existing photomixing setup for 1.55 $\mu$m wavelength, and therefore contains elements which are not necessary for the reflectance measurement. Spontaneous amplified emission of an erbium-doped fiber amplifier

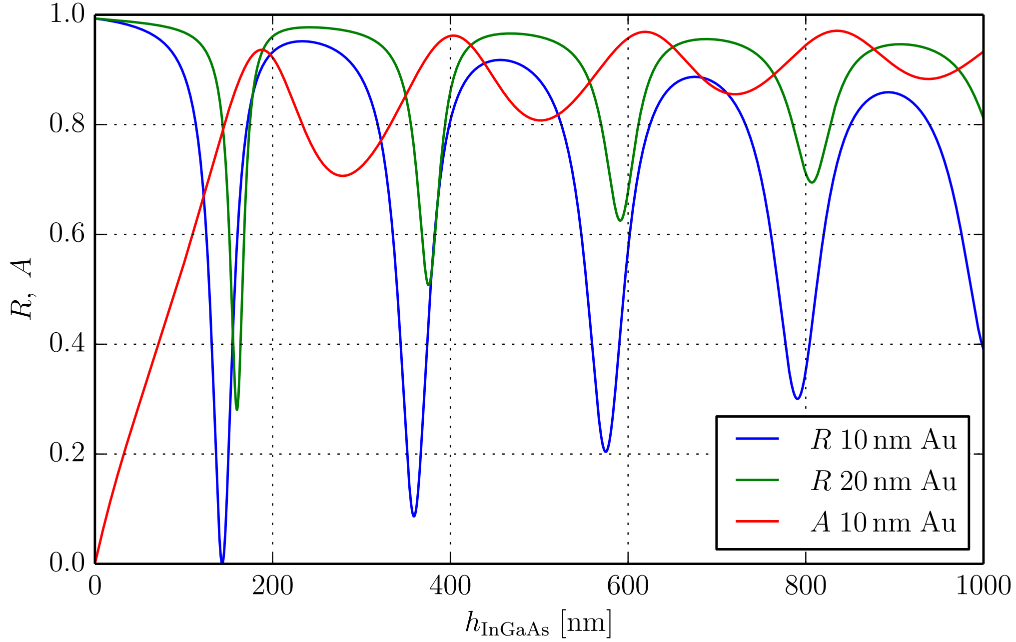


Figure 3.2: Calculated reflectance of a Fabry-Pérot cavity composed of an optically thick Au layer, $In_{0.53}Ga_{0.47}As$ layer, and semitransparent Au top layer. The thickness of the InGaAs layer is varied from 0 to 1 $\mu$m. Calculations for 10 and 20 nm thicknesses of the semitransparent top layer are shown. The red curve shows the fraction of the total absorbed light which is absorbed in the InGaAs layer ($A_{\text{InGaAs}}/(1-R)$) for the 10 nm thick top contact. Illumination is from air ($n = 1$) by coherent light with 1.55 $\mu$m wavelength.

(EDFA) is used as the source. The emission is relatively broadband around 1.55 $\mu$m, and a filter is placed in the free-space part of the setup to reduce the width at half maximum to 40 nm. A 50/50 fiber coupler is used to illuminate the sample with a cleaved fiber, and to verify the spectrum in a spectrum analyzer (SA). The signal is reflected on the sample, back into the cleaved fiber. Half of the reflected signal is detected by a photodiode after the fiber coupler. An oscilloscope is used to measure the diode current. The output power of the EDFA is limited to 13 dBm, because part of the signal is reflected back into the EDFA and no isolator is in the setup in addition to the built-in isolator of the EDFA.

The sample is fabricated from a 1 $\mu$m thick epitaxial $In_{0.53}Ga_{0.47}As$ layer on InP substrate. An eighth of a 2 in wafer is transferred to a Si substrate using Au–Au thermocompression bonding (the process is detailed in section 2.1.1). Wet etching is used to shape the InGaAs layer into a wedge, with thicknesses ranging from 0 to the original 1 $\mu$m. A linear thickness increase is achieved by holding the sample vertically into a beaker, which is initially filled

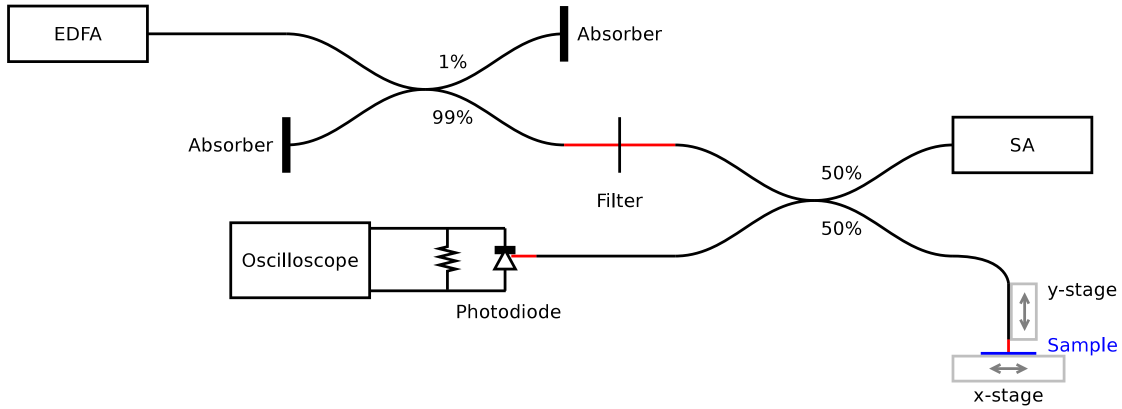


Figure 3.3: Setup used for the measurement of the reflectance of the Fabry-Pérot cavity.

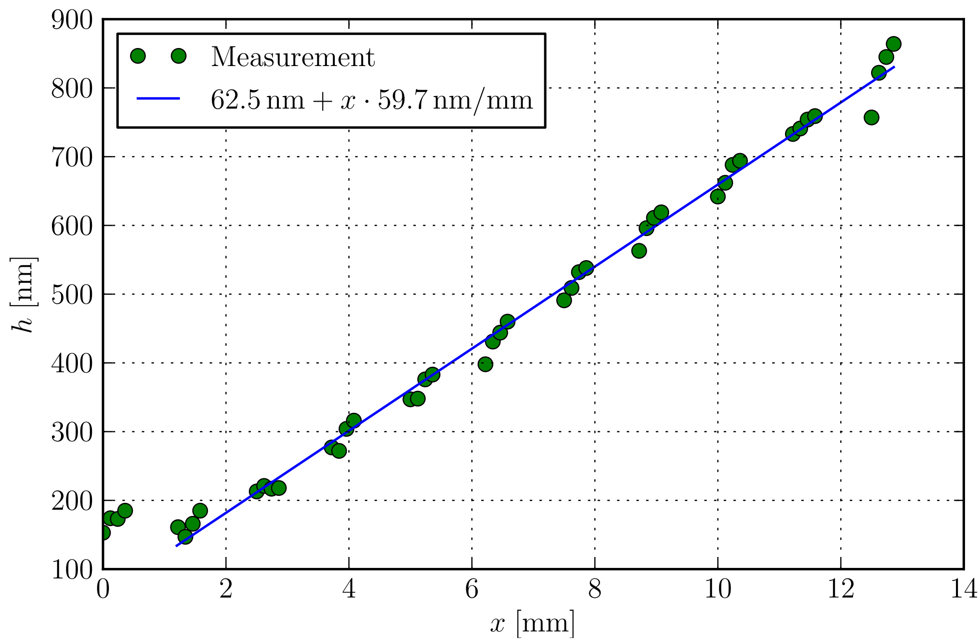


Figure 3.4: Height of the InGaAs layer of the sample used for reflectance measurements in dependence of the position on the surface, measured with a profilometer. A linear fit yields $h = 62.5\,\mathrm{nm} + x \cdot 59.7\,\mathrm{nm/mm}$.

with $H_3PO_4$:$H_2O_2$:$H_2O$ (3:1:20) and which is emptied at constant flow through a tube. 10 nm high Au pads 100 $\mu$m × 100 $\mu$m large are fabricated on the wedge by standard electron beam lithography and lift-off techniques. The etching of the remaining $In_{0.53}Ga_{0.47}As$ between the Au pads in an additional lithography step allows the measurement of the position dependent height of the InGaAs layer by profilometer, see figure 3.4.

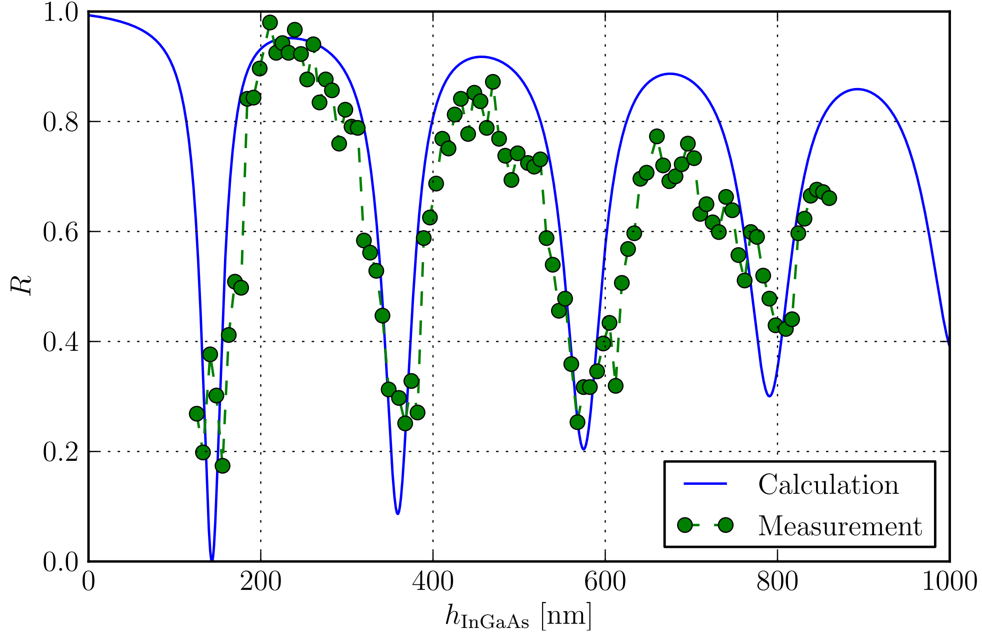


Figure 3.5: Reflectance of a stack composed of 10 nm Au, $In_{0.53}Ga_{0.47}As$ of varying thickness, and an optically thick Au layer. The measured reflectances are obtained by normalizing the photocurrent in the photodiode to that obtained on the pure Au part of the sample, and by assuming that the reflectance on Au reaches 99.3%.

Reflectance measurements are performed by placing the sample on the $x$-stage and adjusting the fiber to be close to the surface with the $y$-stage. From the known diameter of the cleaved fiber (125 $\mu$m) and from the image of sample and fiber taken with a camera with highly magnifying objective, the distance between fiber and sample is estimated to be between 10 $\mu$m and 20 $\mu$m. The measured data is displayed in figure 3.5.

Experiment and calculation are in good agreement. The location of minima and maxima coincide. The amplitude of the measured curve is lower, which may be explained by some roughness of the sample surface after etching and the spectral width of the optical source.

The measured reflectances in the first two minima at $h_1$ and $h_2$ of the 10 nm top contact

sample are about 17% and 25% instead of 0% and 9% as predicted by the calculations. As the minima are narrow, it is difficult to experimentally measure the calculated minimum reflectance.

The most interesting configurations for a photoconductor are the first two minima of a semitransparent gold top contact of 10 nm thickness. The third minimum is above 500 nm thickness of the active layer and makes homogeneous ion implantation more difficult. A semitransparent contact thickness of 20 nm results in relatively high reflectances and less efficient absorption.

Of the two thicknesses $h_1$ and $h_2$, $h_2$ would yield a higher resistance and lower capacitance of the vertical photoconductor, while $h_1$ results in higher photoconductive gain and slightly better absorption. As is detailed in the next section, $h_1$ is chosen for further investigation because of limitations in the available ion implantation energies and thus maximum implantation depths.

### 3.2.2 Determination of ion implantation parameters

In order to determine the implantation parameters dose and ion energy, simulations using the SRIM software have been performed. SRIM [24] is a software package which simulates the transport of ions in matter using the Monte Carlo method. For each individual ion, the path in the semiconductor is simulated using the binary collision approximation, according to which the ion travels on a straight path between collisions with host atoms. Electronic stopping is simulated as loss of kinetic energy of the ions between collisions with host atoms.

The maximum implantation energy available with the IEMN implantation machine is 190 keV. SRIM simulations predict the peak of the corresponding Fe-distribution at 110 nm depth, see figure 3.6. This limitation determines the thickness of the vertical photoconductor: the first absorption maximum of the Fabry-Pérot cavity is around 150 nm thickness, which is compatible with the implantation energy of 190 keV, while the second absorption maximum at 360 nm thickness would result in an inhomogeneous ion distribution in the photoconductor.

In order to optimize the implanted ion distribution, further SRIM simulations have been performed at various ion energies. A two energy implantation with energies of 190 keV and 65 keV and a dose ratio of 5.7 : 1 has been chosen. The corresponding distribution is flat over more than half of the thickness of the photoconductor, see figure 3.7.

A 150 nm thick layer of $In_{0.53}Ga_{0.47}As$ is grown on a 2 in semi-insulating InP substrate by molecular beam epitaxy. In order to investigate several implantation doses, the wafer

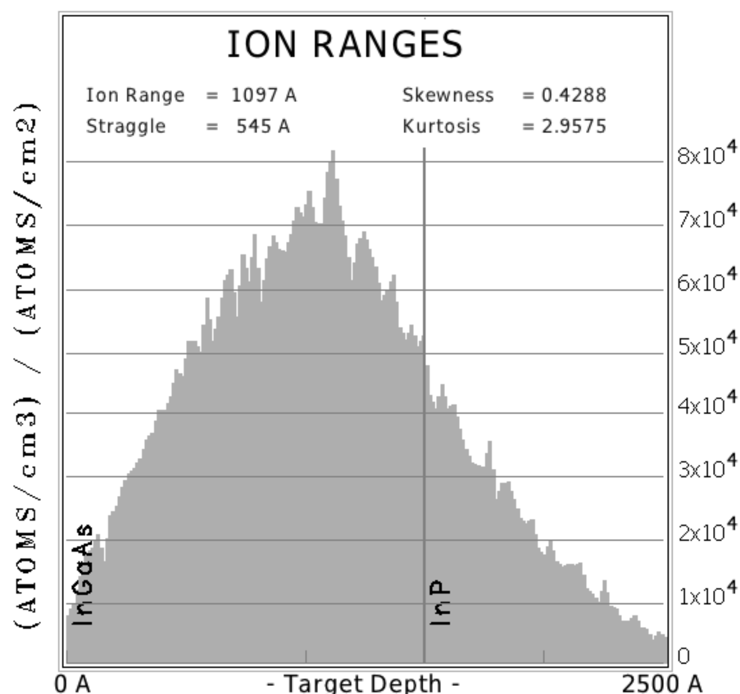


Figure 3.6: Simulated distribution of Fe-atoms in 150 nm InGaAs on InP substrate after implantation with $Fe^{+}$-ions with initial energy of 190 keV.

is cleaved into 4 equal parts. Three parts are implanted while the fourth serves as an unimplanted reference.

The implantation doses are chosen in order to obtain Fe concentrations between $1{\cdot}10^{16}\,\mathrm{cm}^{-3}$ and $1{\cdot}10^{18}\,\mathrm{cm}^{-3}$. The lowest concentration corresponds to the Fe-doping concentration for which high resistivities have been obtained by Wood *et. al* [25]. The upper bound is chosen so as to avoid amorphizing the crystal, which was reported by Suzuki *et al.* [19] for a concentration on the order of $1{\cdot}10^{19}\,\mathrm{cm}^{-3}$. Because of the difficulty of controlling the short implantation time for doses below $1{\cdot}10^{11}\,\mathrm{cm}^{-2}$, the minimum dose used is $1{\cdot}10^{11}\,\mathrm{cm}^{-2}$ for the 65 keV beam, resulting in a Fe concentration of $4{\cdot}10^{16}\,\mathrm{cm}^{-3}$. Table 3.2 summarizes the three different implantation doses used and the simulated resulting Fe concentrations at the plateau of the distribution.

After implantation, all samples are cleaved into two parts, one of which is annealed at 500 °C for 30 s, an intermediate temperature that has been shown to increase the resistivity and decrease the defect concentration [20, 22]. In the following, annealed samples are denoted with subscript $_{\mathrm{ann}}$.

For a first characterization, the transmission spectra of the implanted and annealed samples

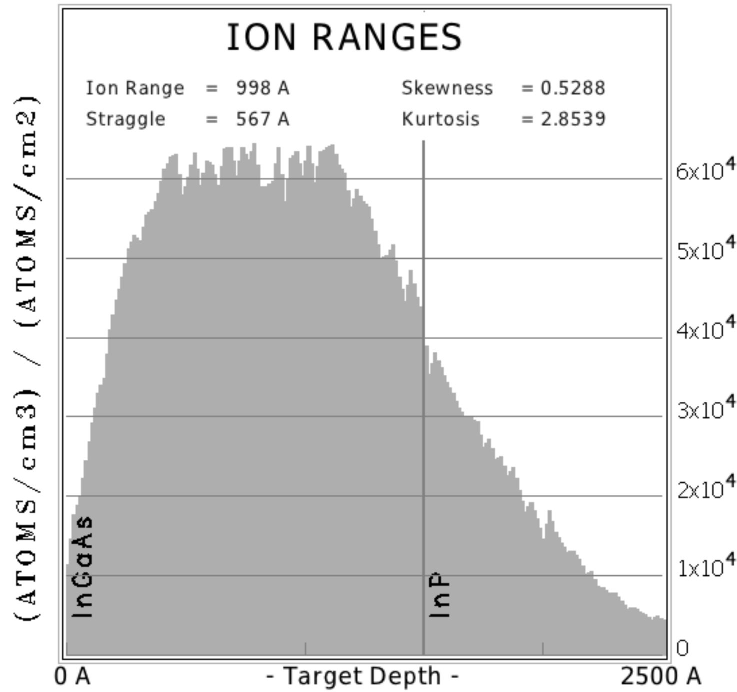


Figure 3.7: Simulated distribution of Fe-atoms in 150 nm InGaAs on InP substrate after implantation with $Fe^+$-ions with initial energies of 190 keV and 65 keV at a dose ratio of 5.7 : 1.

are measured with a commercial Fourier-transform infrared spectrometer (Perkin-Elmer Spectrum GX). The spectra are shown in Figure 3.8 for wavelengths ranging from 1 $\mu$m to 2 $\mu$m. The transmission at long wavelengths above the bandgap is given by Fresnel reflections at the interfaces between InP and air: A refractive index of $n = 3.1$ of InP gives a reflection coefficient $R = (n-1)^2/(n+1)^2 \approx 26\%$ per interface, and a total transmission $T = (1-R)^2 \approx 54\%$ for both interfaces, when neglecting the small difference in $n$ between InGaAs and InP.

Samples A and B show a decrease in transmission below 1.65 $\mu$m, at the bandedge of $In_{0.53}Ga_{0.47}As$, due to the increased absorption. The small change in transmission is due to the limited thickness of the InGaAs layer. The change in transmission is more pronounced for sample A than for sample B. This less well defined bandgap in sample B is due to increased damage to the crystal structure and higher number of defect states within the gap (Urbach tail) due to the higher ion implantation dose. Sample C, which has been implanted at yet higher dose, shows no discernible bandgap. Its crystal structure is highly damaged, and it is most likely not usable as material for a THz photoconductor.

| Sample | dose at 65 keV [$cm^{-2}$] | dose at 190 keV [$cm^{-2}$] | concentration [$cm^{-3}$] |
|---|---|---|---|
| O | | not implanted | |
| A | $1 \cdot 10^{11}$ | $5.7 \cdot 10^{11}$ | $4 \cdot 10^{16}$ |
| B | $2.5 \cdot 10^{11}$ | $1.4 \cdot 10^{12}$ | $1 \cdot 10^{17}$ |
| C | $2.5 \cdot 10^{12}$ | $1.4 \cdot 10^{13}$ | $1 \cdot 10^{18}$ |

Table 3.2: $Fe^+$-implantation doses of the three samples and simulated concentration at the (flat) peak of the ion distribution in figure 3.7.

### 3.2.3 Charge carrier lifetime measurements

The lifetime of photogenerated charge carriers in the implanted samples is investigated using an optical pump–optical probe technique. The setup is shown in figure 3.9. A beam of laser pulses of width 100 fs and repetition rate 80 MHz is generated by a Ti:Sapphire laser at 835 nm. An optical parametric oscillator (OPO) is used to convert the beam to 1550 nm by dividing incoming photons into two photons with lower energy. The idler beam ($\approx$ 1810 nm) is blocked by a filter behind the OPO. The conversion by the nonlinear crystal in the OPO (periodically poled $LiNbO_3$) increases the length of the laser pulses to approximately 150 fs.

A glass plate is used to split the beam into a high intensity pump beam and a lower intensity probe beam. The pump beam is chopped by a mechanical chopper, while a mechanical delay line is incorporated into the path of the probe beam. Both beams are then superposed and focused on the sample. The transmitted probe beam is detected with a photodiode, and the spatially separated transmitted pump beam is blocked. Photodiode and chopper are connected to a lock-in amplifier for synchronous detection with high noise suppression. A computer program controls the delay line and reads the detected signal from the lock-in amplifier, enabling automated acquisition of measurement series.

The expected signal strength in a thin layer of $In_{0.53}Ga_{0.47}As$ of only 150 nm thickness is low, but can still be measured thanks to the sensitivity of the synchronous detection. The time delay $\Delta t$ between pump and probe pulse is scanned using the mechanical delay line. The optical power after the OPO is 190 mW, which is attenuated to give an average pump power after the chopper of 25 mW. The probe beam has a power of 290 $\mu$W.

The differential transmission of sample $A_{ann}$ is shown in figure 3.10. The negative peak at $\Delta t = 0$ is due to two photon absorption in the InP substrate [46]. While the bandgap of InP (1.34 eV) is above the photon energy of the laser beam, two photon absorption is possible. Two-photon absorption is strongly dependent on the laser intensity, quadratic in first approximation. If pump and probe pulses coincide in the substrate, the probability of

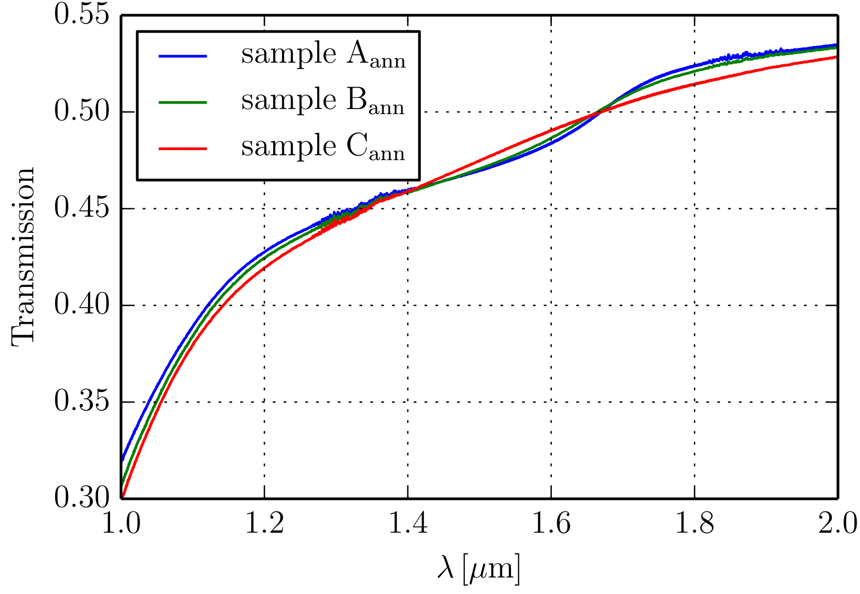


Figure 3.8: Transmission of the implanted samples after annealing as measured with a Fourier-transform infrared spectrometer.

two photon absorption in the probe beam is strongly increased due to the large number of pump photons, and the measured transmission of the probe beam is decreased.

The negative peak is followed by a sharp increase in transmission, which then decreases exponentially. As the energy of photons in the laser beam is larger than the bandgap of the epitaxial layer, electron–hole pairs are generated in this layer. The intensity of the pump beam is high enough to depopulate the valence band in the sample, saturating the absorption. The electrons in the conduction band are trapped with a time constant $\tau$.

If the probe pulse arrives shortly after the pump pulse, $\Delta t < \tau$, absorption of light is reduced due to the limited number of electrons in the valence band that can be excited into the conduction band, and transmission is higher. If the delay between pump and probe beam is large, $\Delta t \gg \tau$, the excited electrons have returned to valence band and absorption of the probe beam is therefore higher. The lifetime $\tau$ of photogenerated charge carriers is given by the time constant of the exponential decrease of the transmission.

An echo with reduced intensity occurs at $\Delta t_0 = 7.5\,\text{ps}$, and a second echo is visible at 15 ps. After traversing active layer and substrate, the pump pulse is partially reflected at the interface InP/air. Its intensity after a second reflection at the interface $In_{0.53}Ga_{0.47}As$/air is still high enough to bleach the active layer, resulting in an echo with the same features as the main pulse, albeit with reduced intensity. The thickness of the substrate can be deduced

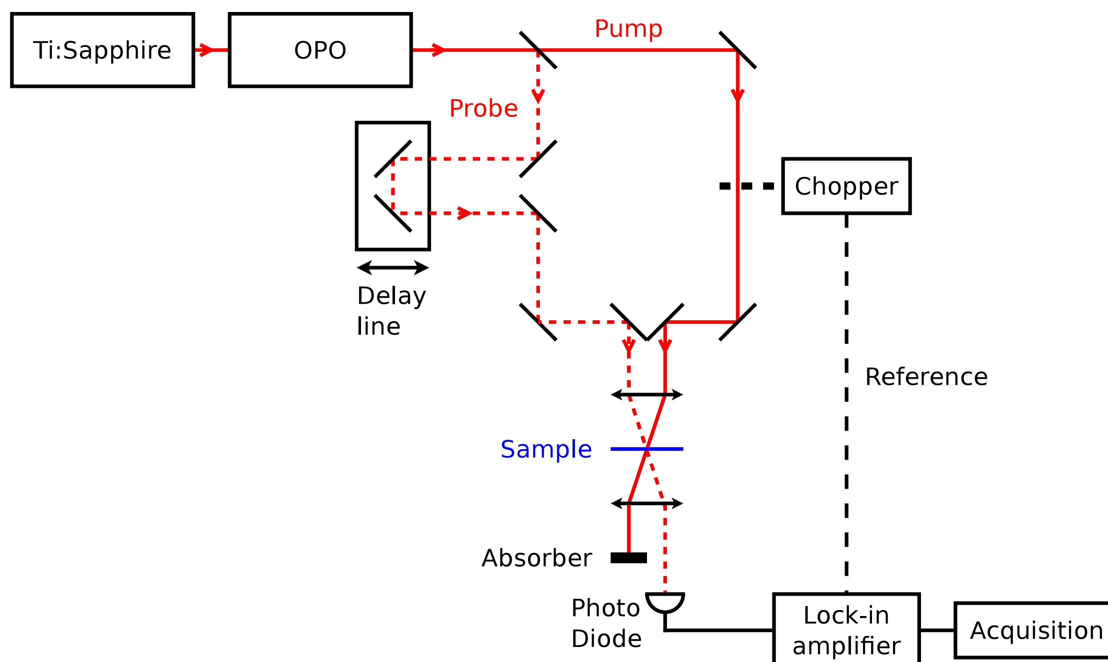


Figure 3.9: Pump–probe setup used for the determination of charge carrier lifetime.

from the delay between main pulse and echo: the optical path traversed by the pump pulse is $l_{\mathrm{opt}} = c\,\Delta t_0$ and the thickness of the substrate is $l = l_{\mathrm{opt}}/2n \approx 360\,\mu\mathrm{m}$ for $n = 3.1$.

A further feature is visible at $\Delta t = -7.5\,\mathrm{ps}$. At this time delay, the first echo of the probe pulse coincides with the pump pulse. Two photon absorption takes place with the same efficiency as at the main peak at $\Delta t = 0$, but only the echo of the probe pulse is involved, making the minimum in transmission much less pronounced.

Figure 3.11 shows the differential transmission of the samples A, $\mathrm{A_{ann}}$, and $\mathrm{B_{ann}}$ as measured with the pump–probe setup. To deduce the charge carrier lifetimes, the part of the data from the maximum to 2 ps is fitted by a single exponential function, $T = o + T_0 \cdot e^{-\Delta t/\tau}$, where $T_0$, the offset $o$, and the lifetime $\tau$ are fit parameters. The single exponential fits the data very well (figure 3.12), and a second lifetime is not needed to explain the data. The deduced lifetimes are approximately 420 fs for samples A and $\mathrm{B_{ann}}$, and 640 fs for sample $\mathrm{A_{ann}}$.

The amplitude of sample $\mathrm{A_{ann}}$ is higher than that of sample $\mathrm{B_{ann}}$, indicating a better crystal structure, which is consistent with the FTIR spectrometer measurements. Samples B, C, and $\mathrm{C_{ann}}$ did not show a measurable increase in transmission after the pump pulse, and therefore no lifetimes could be deduced. The crystal structure of these samples is highly damaged, resulting in many defects within the gap of the as-grown material. This is also

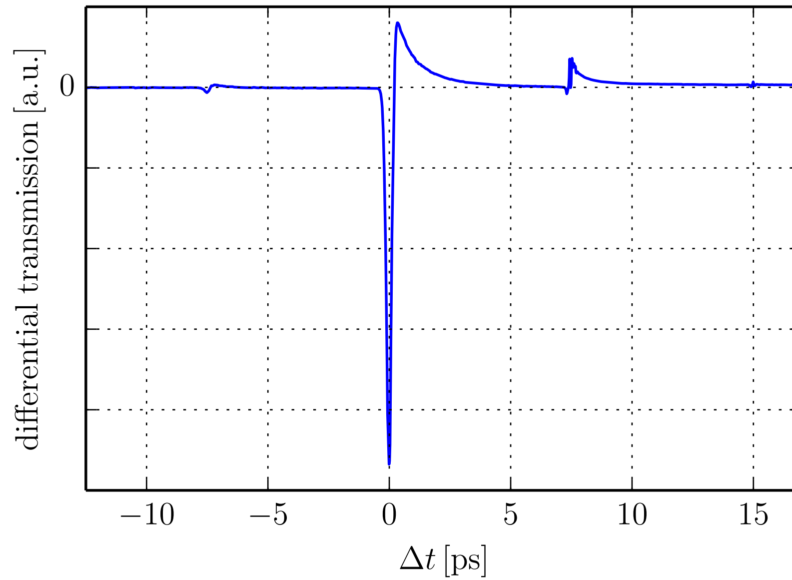


Figure 3.10: Differential transmission of sample $A_{ann}$ measured using the pump–probe setup shown in figure 3.9 at a wavelength of 1.55 $\mu$m.

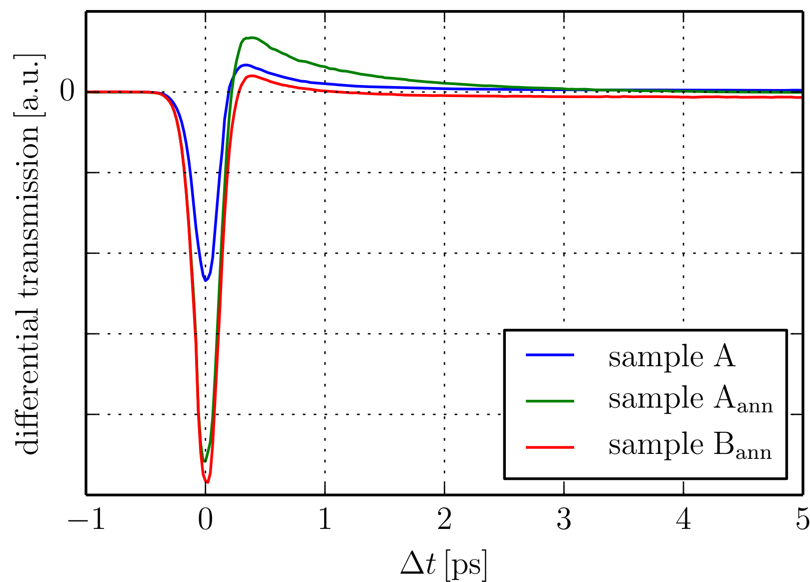


Figure 3.11: Differential transmission of the short lifetime samples measured at 1.55 $\mu$m using the pump–probe setup. Lifetimes are approximately 400 fs for samples A and $B_{ann}$, and 800 fs for sample $A_{ann}$.

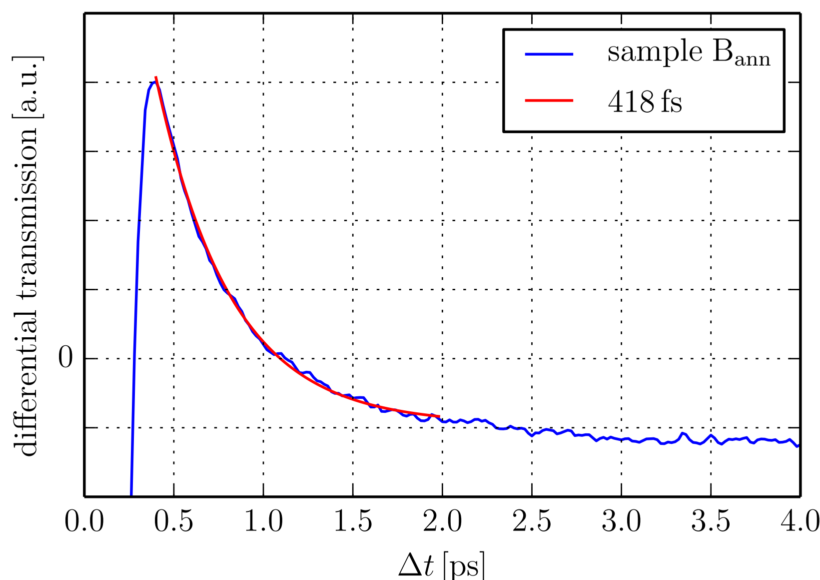


Figure 3.12: Differential transmission of sample $B_{ann}$ and exponential fit from the maximum to 2 ps. The best fit is obtained with a time constant of 418 fs.

consistent with the absence of a gap in the FTIR spectrum of sample $C_{ann}$.

Annealing improved the crystal structure of sample B, and the lifetime of sample $B_{ann}$ could be measured. The defect density in sample $A_{ann}$ is also reduced, which explains the longer lifetime as compared to sample A.

The lifetimes of the as-grown layer, sample O, and the annealed, unimplanted layer, sample $O_{ann}$, are much longer than those of the implanted samples. Figure 3.13 shows the measured differential transmission for sample O. The long lifetime results in only a small change in transmission between the main pulse and the echo. The transmission is higher after the echo, implying that the sample was not completely bleached after one pass of the pump pulse, and that more electron-hole pairs could be created by the echo pulse. This effect is increased due to the low thickness of the epitaxial layer.

Even 200 ps after the pump pulse, the transmission has only decayed to about 5/6 of the peak value. In order to accurately deduce the lifetime, a longer delay line would be necessary to increase the maximum $\Delta t$ that can be measured. However, it can be stated that the lifetimes of the unimplanted samples are on the order of several 100 ps, and probably determined by surface recombinations.

The lifetimes of all measured samples are summarized in table 3.3.

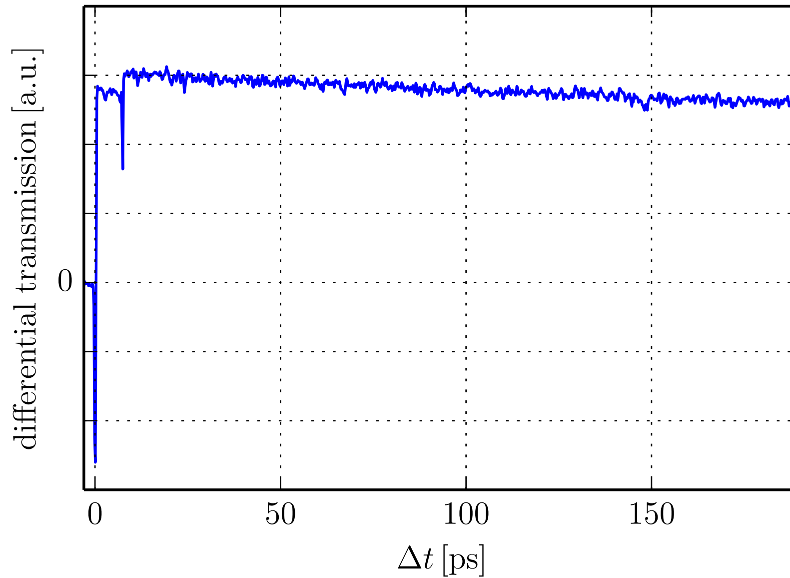


Figure 3.13: Differential transmission of the as-grown layer measured using the pump–probe setup. The charge carrier life time is several 100 ps.

The pump–probe measurements have shown that short lifetimes below 1 ps have been achieved in the measurable implanted samples. The highest implantation dose led to high damage to the sample and no charge carrier lifetimes could be measured. Sample B seems to have been implanted with close to the maximum dose before inflicting too much damage: no signal was detected from the as-implanted sample, but annealing sufficiently recovered the crystal structure. Samples A, $A_{ann}$, and $B_{ann}$ show short lifetimes suitable for the fabrication of THz photoconductors.

### 3.2.4 Hall effect measurements

Hall effect measurements are performed in order to determine the charge carrier concentration and mobility in the different implanted samples. The Van-der-Pauw configuration [47] is especially useful as it can be used for arbitrarily shaped thin samples of constant height. Four ohmic contacts on the circumference of the sample are needed in order to reduce the errors of the Van-der-Pauw method.

Resist protection in the form of a clover leaf like pattern (see figure 3.14) is fabricated on the samples by standard optical lithography techniques. The unprotected areas are then etched in a mixture of $H_3PO_4$:$H_2O_2$:$H_2O$ with proportions 5:1:20, and the resist is removed

| Sample | lifetime | |
|---|---|---|
| | before annealing | annealed 500 °C |
| O | $> 100$ ps | $> 100$ ps |
| A | 400...440 fs | 620...660 fs |
| B | ... | 400...440 fs |
| C | ... | ... |

Table 3.3: Lifetimes of the $Fe^+$-implanted samples deduced from optical pump–probe experiments. For the highly damaged samples, no lifetime could be deduced from the pump–probe curves.

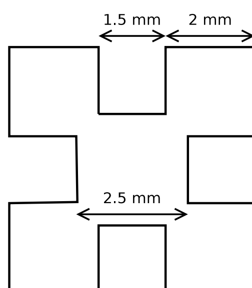


Figure 3.14: Clover-leaf like pattern used for Hall measurements. The sample is contacted by the pads in the corners, resulting in contacts on the circumference of the inner square, as required for the Van-der-Pauw configuration.

in acetone. For the ohmic contacts, small indium pellets are deoxidized in $HNO_3$, rinsed in water and dried at 100 °C for 10 min. They are then deposited on the contact pads of the clover leaf pattern. An Ohmic contact is formed by heating to 360 °C for 3 min under argon atmosphere. The argon atmosphere is maintained until the sample cools down below 100 °C.

Hall measurements are performed in a commercial apparatus (Bio-rad Hall system). The sample is contacted by four needles positioned on the indium pellets. Measurements are performed in the dark, and it is verified that Ohmic contacts are formed. The measured data of sheet carrier concentration $n_{\mathrm{sh}}$ and resistance $R_{\mathrm{sh}}$ as well as mobility $\mu$ is summarized in table 3.4.

The Hall effect measurements indicate that all samples show a relatively high n-background above $1{\cdot}10^{16}\,\mathrm{cm}^{-3}$, even after implantation at the highest dose investigated. This is well above the intrinsic value of $6.3{\cdot}10^{11}\,\mathrm{cm}^{-3}$ and higher than reported in other Fe implantation works ($6.7{\cdot}10^{14}$ has been reported in [20]) and results in a low material resistivity. The

| Sample | $n_{sh}$ [$10^{11}$ cm$^{-2}$] | $\mu$ [cm$^2$/V s] | $n$ [$10^{16}$ cm$^{-3}$] | $\rho$ [$\Omega$cm] |
|---|---|---|---|---|
| O | 19 | 1800 | 13 | 0.027 |
| $O_{ann}$ | 11 | 2500 | 7.3 | 0.034 |
| A | 29 | 500 | 19 | 0.066 |
| $A_{ann}$ | 13 | 1100 | 8.7 | 0.065 |
| B | 15 | 400 | 10 | 0.16 |
| $B_{ann}$ | 9.7 | 1000 | 6.5 | 0.096 |
| C | 5.1 | 100 | 3.4 | 1.3 |
| $C_{ann}$ | 1.9 | 300 | 1.3 | 1.6 |

Table 3.4: Electrical parameters measured using the Hall effect for $Fe^{+}$-implanted samples before and after annealing. The volumic charge carrier concentration $n$ is calculated from the measured sheet value $n_{sh}$ and the sample height $h = 150$ nm. The resistivity $\rho$ is calculated from $n$ and $\mu$: $\rho = 1/ne\mu$.

Hall mobilities are good for a short lifetime material with the exception of sample C, but contribute to the low resistivity.

It should be noted that the Hall measurements are difficult to interpret due to the thin epitaxial layer. Assuming that the conduction band edge at the surface of the InGaAs layer is $\psi_s$ higher than in the bulk, a depletion region of width $W = \sqrt{2\psi_s\varepsilon_0\varepsilon_r/qn}$ is formed at the surface ($q$: elementary charge, $n$: charge carrier density in InGaAs, $\varepsilon_r$: dielectric constant) [48]. Assuming a surface potential of $\psi_s = 0.3$ eV and $n = 10^{17}$ cm$^{-3}$ yields $W \approx 64$ nm, and for a carrier concentration of $10^{16}$ cm$^{-3}$, $W$ becomes $\approx 204$ nm. It is therefore possible that the surface depletion region expands into a significant portion of the InGaAs layer.

In order to verify the resistivities obtained from the Hall measurements, $I$-$V$ measurements in a configuration similar to a vertical photoconductor are performed. One part of sample $B_{ann}$ is bonded to a Si substrate by Au–Au thermocompression bonding, and the InP substrate is removed by wet etching. Au contacts of $80\,\mu$m $\times$ $80\,\mu$m and $65\,\mu$m $\times$ $65\,\mu$m are fabricated on the InGaAs surface, and $I$-$V$ curves between the contact and the metallic ground plane are measured in 4-wire configuration. The measured curves are shown in figure 3.15.

The current is limited to 50 mA to protect the needles used for the measurement. Due to the low resistivity of the material and the large surface of the contacts, which is necessary to permit the placement of two needles, the maximum bias is only 6 mV for the smaller contact size. In the measured voltage range, no deviation from the Ohmic behavior could

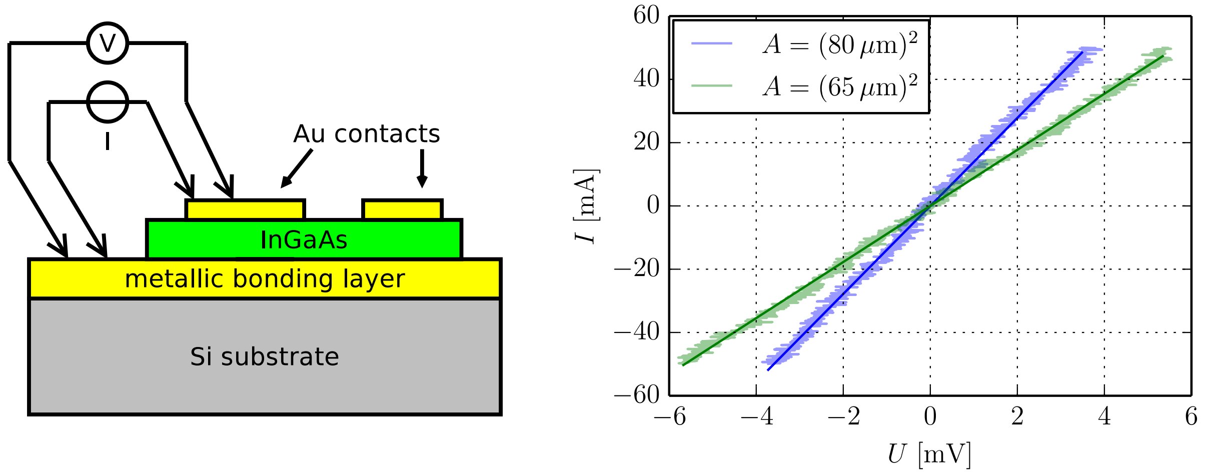


Figure 3.15: Left: Schematic of the sample for 4-wire $I$-$V$ measurements. Right: $I$-$V$ curves for two different contact sizes on sample $B_{ann}$ after transfer to Si substrate, and linear fits. The linear fits yield $R = 0.072\,\Omega$ and $0.113\,\Omega$ for the $80\,\mu$m and $65\,\mu$m sidelength contacts, respectively.

be observed. From the measured resistances, resistivities of $0.31\,\Omega$cm and $0.32\,\Omega$cm are calculated for the $80\,\mu$m and $65\,\mu$m sidelength contacts, respectively. This is of the same order of magnitude as the value obtained from the Hall measurements.

A vertical photoconductor with $3\,\mu$m diameter based on a 150 nm thick layer of material with resistivity of $0.3\,\Omega$cm (sample $B_{ann}$) would have a dark resistance of only $64\,\Omega$. At 1 V bias, the dark current would already reach 16 mA. The Joule heating by the dark current alone would quickly destroy such a photoconductor.

It is interesting to note that due to the high electron mobility $\mu \approx 1000\,\mathrm{cm^2\,V^{-1}\,s^{-1}}$ (sample $B_{ann}$) and the thinness of the photoconductive layer $h = 150$ nm, a bias of only $U = 1$ V is sufficient for electrons to reach saturation velocity ($\mu U/h \approx 6.7 \cdot 10^7$ cm/s). Moreover, the transit time for electrons then is on the order of 1 ps, resulting in a high photoconductive gain. A high photocurrent is therefore expected already at $U = 1$ V, and it is assumed that vertical THz photoconductors could be fabricated with a material having a 10 to 100 times higher resistivity and correspondingly reduced dark current. At higher bias voltages than 1 V, an increase of the photocurrent would be expected mainly from an increased hole photocurrent. Due to the short electron transit time, the short lifetime of the material is needed mainly to reduce the dc hole current.

From table 3.4 it appears that the residual carrier concentration of the annealed samples is not reduced much by higher implantation doses. This suggests that a large fraction of

the implanted Fe-ions is not electrically active. For Sample $A_{ann}$, a higher residual carrier concentration was measured than for the non-implanted sample. This may be due to donor levels added by the defects from Fe ions which are not in the correct site. A higher annealing temperature might have been necessary to allow the migration of Fe ions to substitutional sites.

Due to the small size of the sample implanted for each dose, no pieces remain for annealing at higher temperature. Annealing of the unannealed samples used for Hall measurements would require the prior removal of the In pellets deposited for Ohmic contacts. Attempts to remove the pellets in hot HCl were not successful, and no annealing at higher temperature was therefore performed.

## 3.3 Summary

In this chapter, work towards a vertical photoconductor for use with 1.55 $\mu$m telecom wavelength lasers has been presented. The investigated material is based on Fe-implanted $In_{0.53}Ga_{0.47}As$. A high photocurrent at low bias voltages is expected from such a photoconductor due to the high photoconductive gain and the high electron mobility.

The thickness of the active layer has been calculated for maximum light absorption in the cavity using the transfer matrix method, and the calculations have been confirmed by reflectance measurements in dependence of the active layer height.

The implantation energies of Fe ions have been determined by simulations using the SRIM software. A relatively flat Fe distribution is expected by implantation with ion energies of 65 keV and 190 keV at a dose ratio of 1 : 5.7. The flat distribution is possible due to the thin InGaAs layer and is an advantage of the vertical photoconductor structure over the thicker layers of ion-implanted materials for planar photoconductors.

Pump-probe measurements have been performed on samples implanted at various doses, before and after annealing at 500 °C. Sub-picosecond lifetimes suitable for THz photomixers have been obtained.

Hall measurements in the Van-der-Pauw configuration have been performed for electrical characterization of the samples. High carrier mobilities for short lifetime materials have been obtained, but the high residual dark carrier concentration resulted in low resistivities. It is assumed that annealing at higher temperature would have allowed a larger fraction of Fe ions to reach active sites and reduce the carrier concentration. However further studies would have been necessary before the fabrication of photoconductors. Due to the limited time

available, this was not pursued further, instead focusing the attention on the fabrication and characterization of the UTC photodiodes which were developed in parallel and are presented in the next chapter.

# Bibliography


[1] M. Tani, K. Lee, X. Zhang, *Detection of terahertz radiation with low-temperature-grown GaAs-based photoconductive antenna using 1.55 μm probe*, Applied Physics Letters **77**, 1396 (2000)

[2] E. R. Brown, K. A. McIntosh, K. B. Nichols, C. L. Dennis, *Photomixing up to 3.8 THz in low-temperature-grown GaAs*, Appl. Phys. Lett. **66**, 285 (1995)

[3] E. R. Brown, F. W. Smith, K. A. McIntosh, *Coherent millimeter-wave generation by heterodyne conversion in low-temperature-grown GaAs photoconductors*, J. Appl. Phys. **73**, 1480 (1993)

[4] S. Gupta, J. F. Whitaker, G. A. Mourou, *Ultrafast Carrier Dynamics in III–V Semiconductors Grown by Molecular-Beam Epitaxy at Very Low Substrate Temperatures*, IEEE Journal of Quantum Electronics **28**, 2464 (1992)

[5] H. Künzel, J. Böttcher, R. Gibis, G. Urmann, *Material properties of* $Ga_{0.47}In_{0.53}As$ *grown on InP by low-temperature molecular beam epitaxy*, Applied Physics Letters **61**, 1347 (1992)

[6] B. Sartorius, H. Roehle, H. Künzel, J. Böttcher, M. Schlak, D. Stanze, H. Venghaus, M. Schell, *All-fiber terahertz time-domain spectrometer operating at 1.5 μm telecom wavelengths*, Optics Express **16**, 9565 (2008)

[7] Y. Chen, S. Prabhu, S. Ralph, D. McInturff, *Trapping and recombination dynamics of low-temperature-grown InGaAs/InAlAs multiple quantum wells*, Applied Physics Letters **72**, 439 (1998)

[8] D. Vignaud, J.-F. Lampin, E. Lefebvre, M. Zaknoune, F. Mollot, *Electron lifetime of heavily Be-doped* $In_{0.53}Ga_{0.47}As$ *as a function of growth temperature and doping density*, Appl. Phys. Lett. **80**, 4151 (2002)

[9] A. Takazato, M. Kamakura, T. Matsui, J. Kitagawa, Y. Kadoya, *Detection of terahertz waves using low-temperature-grown InGaAs with 1.56 μm pulse excitation*, Applied Physics Letters **90**, 101119 (2007)

[10] A. Takazato, M. Kamakura, T. Matsui, J. Kitagawa, Y. Kadoya, *Terahertz wave emission and detection using photoconductive antennas made on low-temperature-grown InGaAs with 1.56* $\mu$m *pulse excitation*, Appl. Phys. Lett. **91**, 011102 (2007)

[11] C. Baker, I. S. Gregory, W. R. Tribe, I. V. Bradley, M. J. Evans, E. H. Linfield, M. Missous, *Highly resistive annealed low-temperature-grown InGaAs with sub-500* fs *carrier lifetimes*, Applied Physics Letters **85**, 4965 (2004)

[12] R. Czarny, *Étude et réalisation d'une source térahertz accordable de grande pureté spectrale*, PhD thesis, Université Lille 1 (2007)

[13] J. Mangeney, *THz Photoconductive Antennas Made From Ion-Bombarded Semiconductors*, Journal of Infrared Millimeter Terahertz Waves **33**, 455 (2012)

[14] L. Joulaud, J. Mangeney, J.-M. Lourtioz, P. Crozat, G. Patriarche, *Thermal stability of ion-irradiated InGaAs with (sub-) picosecond carrier lifetime*, Applied Physics Letters **82**, 856 (2003)

[15] J. Mangeney, L. Joulaud, P. Crozat, J. Lourtioz, J. Decobert, *Ultrafast response (∼ 2.2 ps) of ion-irradiated InGaAs photoconductive switch at 1.55* $\mu$m, Applied Physics Letters **83**, 5551 (2003)

[16] N. Chimot, J. Mangeney, L. Joulaud, P. Crozat, H. Bernas, K. Blary, J.-F. Lampin, *Terahertz radiation from heavy-ion-irradiated* $In_{0.53}Ga_{0.47}As$ *photoconductive antenna excited at 1.55* $\mu$m, Applied Physics Letters **87**, 193510 (2005)

[17] J. Mangeney, A. Merigault, N. Zerounian, P. Crozat, K. Blary, J.-F. Lampin, *Continuous wave terahertz generation up to 2 THz by photomixing on ion-irradiated* $In_{0.53}Ga_{0.47}As$ *at 1.55 µm wavelengths*, Appl. Phys. Lett. **91**, 241102 (2007)

[18] J. Mangeney, F. Meng, D. Gacemi, E. Peytavit, J.-F. Lampin, T. Akalin, *Terahertz generation and power limits in* $In_{0.53}Ga_{0.47}As$ *photomixer coupled to transverse-electromagnetic-horn antenna driven at 1.55* $\mu$m *wavelengths*, Appl. Phys. Lett. **97**, 161109 (2010)

[19] M. Suzuki, M. Tonouchi, *Fe-implanted InGaAs terahertz emitters for 1.56* $\mu$m *wavelength excitation*, Appl. Phys. Lett. **86**, 051104 (2005)

[20] C. Carmody, H. Tan, C. Jagadish, A. Gaarder, S. Marcinkevicius, *Ion-implanted* $In_{0.53}Ga_{0.47}As$ *for ultrafast optoelectronic applications*, Appl. Phys. Lett. **82**, 3913 (2003)

[21] B. Tell, U. Koren, B. Miller, *Metalorganic vapor-phase-epitaxial growth of Fe-doped* $In_{0.53}Ga_{0.47}As$, Journal of Applied Physics **61**, 1172 (1987)

[22] S. Pearton, C. Abernathy, M. Panish, R. Hamm, L. Lunardi, *Implant-induced high-resistivity regions in InP and InGaAs*, Journal of Applied Physics **66**, 656 (1989)

[23] M. Suzuki, M. Tonouchi, *Fe-implanted InGaAs photoconductive terahertz detectors triggered by 1.56* μm *femtosecond optical pulses*, Appl. Phys. Lett. **86**, 163504 (2005)

[24] J. Ziegler, http://srim.org

[25] C. Wood, O. Hatem, J. Cunningham, E. Linfield, A. Davies, P. Cannard, M. Robertson, D. Moodie, *Terahertz emission from metal-organic chemical vapor deposition grown Fe:InGaAs using 830* nm *to 1.55* μm *excitation*, Appl. Phys. Lett. **96**, 194104 (2010)

[26] O. Hatem, J. Cunningham, E. Linfield, C. Wood, A. Davies, P. Cannard, M. Robertson, D. Moodie, *Terahertz-frequency photoconductive detectors fabricated from metal-organic chemical vapor deposition-grown Fe-doped InGaAs*, Appl. Phys. Lett. **98**, 121107 (2011)

[27] C. Kadow, S. B. Fleischer, J. P. Ibbetson, J. E. Bowers, A. C. Gossard, J. W. Dong, C. J. Palmstrom, *Self-assembled ErAs islands in GaAs: Growth and subpicosecond carrier dynamics*, Applied Physics Letters **75**, 3548 (1999)

[28] D. Driscoll, M. Hanson, C. Kadow, A. C. Gossard, *Electronic structure and conduction in a metal–semiconductor digital composite: ErAs:InGaAs*, Applied Physics Letters **78**, 1703 (2001)

[29] D. C. Driscoll, M. P. Hanson, A. C. Gossard, *Carrier compensation in semiconductors with buried metallic nanoparticles*, Journal of Applied Physics **97**, 016102 (2004)

[30] A. Schwagmann, Z-Y Zhao, F. Ospald, H. Lu, D. Driscoll, M. Hanson, A. Gossard, J. Smet, *Terahertz emission characteristics of ErAs:InGaAs-based photoconductive antennas excited at 1.55 μm*, Appl. Phys. Lett. **96**, 141108 (2010)

[31] B. Sartorius, M. Schlak, D. Stanze, H. Roehle, H. Künzel, H-G Schmidt, D. Bach, R. Kunkel, M. Schell, *Continuous wave terahertz systems exploiting 1.5* μm *telecom technologies*, Optics Express **17**, 15001 (2009)

[32] H. Roehle, R. Dietz, H. Hensel, J. Böttcher, H. Künzel, D. Stanze, M. Schell, B. Sartorius, *Next generation* 1.5 μm *terahertz antennas: mesa-structuring of InGaAs/InAlAs photoconductive layers*, Optics Express **18**, 2296 (2010)

[33] A. Fekecs, M. Bernier, D. Morris, M. Chicoine, F. Schiettekatte, P. Charette, R. Arès, *Fabrication of high resistivity cold-implanted InGaAsP photoconductors for efficient pulsed terahertz devices*, Opt. Mat. Expr. **1**, 1165 (2011)

[34] A. Fekecs, M. Chicoine, B. Ilahi, F. Schiettekatte, P. Charette, R. Arès, *Towards semi-insulating InGaAsP/InP layers by post-growth processing using Fe ion implantation and rapid thermal annealing*, J. Phys. D: Appl. Phys. **46**, 165106 (2013)

[35] X. Wallart, C. Coinon, S. Plissard, S. Godey, O. Offranc, Y. Androussi, V. Magnin, J.-F. Lampin, *Picosecond carrier lifetime in low-temperature-grown GaAsSb*, Appl. Phys. Express **3**, 111202 (2010)

[36] J. Sigmund, C. Sydlo, H. Hartnagel, N. Benker, H. Fuess, F. Rutz, T. Kleine-Ostmann, M. Koch, *Structure investigation of low-temperature-grown GaAsSb, a material for photoconductive terahertz antennas*, Appl. Phys. Lett. **87**, 252103 (2005)

[37] J. Sigmund, H. L. Hartnagel, *Low-temperature growth and post-growth annealing of GaAsSb*, J. of Crystal Growth **278**, 209 (2005)

[38] J. Sigmund, J.-F. Lampin, V. Ivannikov, C. Sydlo, M. Feiginov, D. Pavlidis, P. Meissner, H. Hartnagel, *Low-Temperature Grown GaAsSb with Sub-Picosecond Photocarrier Lifetime for Continuous-Wave Terahertz Measurements*, IEICE Trans. Electron. **E91-C(7)**, 1058 (2008)

[39] A. Krotkus, *Semiconductors for terahertz photonics applications*, Journal of Physics D **43**, 273001 (2010)

[40] V. Pačebutas, A. Bičiunas, S. Balakauskas, A. Krotkus, G. Andriukaitis, D. Lorenc, A. Pugžlys, A. Baltuška, *Terahertz time-domain-spectroscopy system based on femtosecond Yb:fiber laser and GaBiAs photoconducting components*, Applied Physics Letters **97**, 031111 (2010)

[41] A. Arlauskas, P. Svidovsky, K. Bertulis, R. Adomavicius, A. Krotkus, *GaAsBi Photoconductive Terahertz Detector Sensitivity at Long Excitation Wavelengths*, Applied Physics Express **5**, 022601 (2012)

[42] K. Tan, S. Yoon, S. Wicaksono, W. Loke, D. Li, N. Saadsaoud, C. Tripon-Canseliet, J.-F. Lampin, D. Decoster, J. Chazelas, *Low temperature grown GaNAsSb: A promising material for photoconductive switch application*, Applied Physics Letters **103**, 111113 (2013)

[43] D. C. Driscoll, M. P. Hanson, A. C. Gossard, *Ultrafast photoresponse at* 1.55 $\mu$m *in InGaAs with embedded semimetallic ErAs nanoparticles*, Appl. Phys. Lett. **86**, 051908 (2005)

[44] E. Peytavit, S. Lepilliet, F. Hindle, C. Coinon, T. Akalin, G. Ducournau, G. Mouret, J.-F. Lampin, *Milliwatt-level output power in the sub-terahertz range generated by photomixing in a GaAs photoconductor*, Appl. Phys. Lett. **99**, 223508 (2011)

[45] H. A. Macleod, *Thin-Film Optical Filters* (CRC Press, 2010)

[46] D. Vignaud, J.-F. Lampin, F. Mollot, *Two-photon absorption in InP substrates in the 1.55μm range*, Applied Physics Letters **85**, 239 (2004)

[47] L. van der Pauw, *A method of measuring specific resistivity and hall effect of discs of arbitraray shape*, Philips research reports **13**, 1 (1958)

[48] S. Sze, *Semiconductor device physics* (Wiley, 2002)

# 4 UTC photodiodes with efficient light absorption

Photomixers are useful in various applications, such as high-speed data transmission, spectroscopy, and imaging. For more widespread employment of systems based on photomixing, especially mobile systems, a high efficiency of the photomixer is preferable, as it decreases the heating of the device itself and subsequently the necessary heat sinking capabilities of the packaging, but also the power requirements of lasers and voltage supply units. A highly efficient photomixer can therefore result in a significant overall reduction of the power requirements of such systems, and also reduce the cost as less powerful sources are sufficient for powerful THz sources.

In this chapter, two structures for UTC photodiodes with more efficient light absorption than the widely employed vertical structure are presented. The first structure, double collector UTC photodiodes, is composed of two diodes stacked back-to-back above each other which are illuminated simultaneously. The second structure is based on flip-chip wafer bonding of the epitaxial layers to a Si substrate and integrated with a semitransparent top contact. Devices fabricated with this top-contact have shown high efficiency even without the flip-chip bonding [1], and a further improvement is expected due to the reflection of light at the metallic bonding layer and due to lower series resistances.

## 4.1 Double collector UTC photodiodes

By stacking two photodiodes back-to-back above each other, the effective absorption layer thickness can be doubled without increasing the carrier transit time. The double collector UTC photodiodes have been conceived by Dr. Jean-François Lampin in 2008. A patent application has been filed independently by researchers from Alcatel Lucent in 2010 [2]. For p-i-n diodes, a similar p-i-n-i-p structure has already been used earlier [3].

Recently, the concept has been demonstrated to work well with UTC photodiodes at GHz

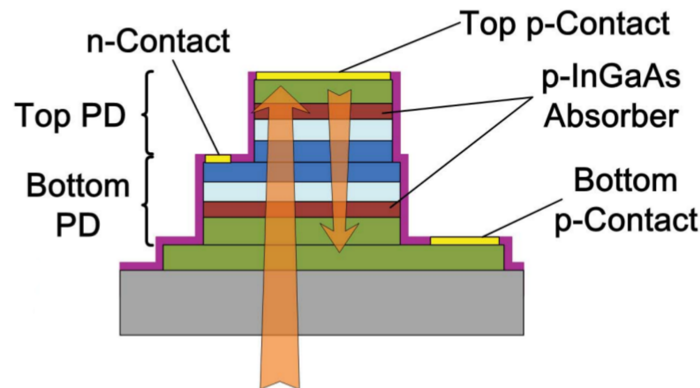


Figure 4.1: Schematic of back-to-back UTC photodiode configuration with 28 GHz bandwidth [4].

frequencies [4] (figure 4.1). A backside illuminated p-i-n-i-p structure was integrated with a coplanar waveguide (CPW) for on-wafer measurements. The absorption regions were 500 nm wide each, and the transport layers were 635 nm thick. A device with 24 $\mu$m diameter showed a responsivity of 0.86 A/W, saturation current of 62 mA and RF power of 31.6 mW at 24 GHz.

### 4.1.1 Design of double collector UTC photodiodes

Development of a double collector UTC photodiode for photomixing in the THz region has been started in the THz photonics group of the IEMN by Dr. Alexandre Beck. The epitaxy and a first version of the masks for the fabrication process have been designed by Dr. Beck, and the first processing steps have been performed, showing some modifications to the masks were needed. Modification of the masks and fabrication of the final devices was part of this PhD work.

The layers of the epitaxy used for the fabrication of the devices are shown in table 4.1. InP is used as diffusion barrier in layer 7. The InP diffusion barrier is not ideal, because it not only blocks electrons, but also presents a barrier for holes. In previous theses in the THz photonics group, $Al_{0.075}In_{0.53}Ga_{0.395}As$ had been used as diffusion barrier [5, 1]. This is not possible for the double collector UTC diode, because the InP layer also serves as an etch stop layer during wet etching, allowing the anode contact to be placed on layer 8. A diffusion layer between layers 8 and 9 has been omitted, and the anode contact region (layer 8) is absorbing at the intended wavelength of operation. Some of the photogenerated electrons will diffuse to the anode contact, but due to the built-in quasi-field, most will be accelerated

| No. | Layer | Material | Thickness [nm] | Doping [$cm^{-3}$] |
|---|---|---|---|---|
| 1 | cathode contact | $In_{0.4}Ga_{0.6}As$ | 10 | $n = 3 \cdot 10^{19}$ |
| 2 | sub-collector | InP | 20 | $n = 3 \cdot 10^{19}$ |
| 3 | collector | InP | 100 | nid |
| 4 | doping plane | InP | 7 | $n = 1 \cdot 10^{18}$ |
| 5 | spacer | $Al_{0.235}In_{0.53}Ga_{0.235}As$ | 20 | nid |
| | | $In_{0.6}Ga_{0.4}As$ | 10 | $p = 1 \cdot 10^{18}$ |
| 6 | absorption region (graded composition) | $In_{0.6}Ga_{0.4}As \dots$ $\dots In_{0.46}Ga_{0.54}As$ | 90 | $p = 1 \cdot 10^{18}$ |
| 7 | diffusion barrier | InP | 20 | $p = 2 \cdot 10^{19}$ |
| 8 | anode contact | $In_{0.53}Ga_{0.47}As$ | 20 | $p = 4 \cdot 10^{19}$ |
| 9 | absorption region (graded composition) | $In_{0.46}Ga_{0.54}As \dots$ $\dots In_{0.6}Ga_{0.4}As$ | 90 | $p = 1 \cdot 10^{18}$ |
| 10 | spacer | $In_{0.6}Ga_{0.4}As$ | 10 | $p = 1 \cdot 10^{18}$ |
| | | $Al_{0.235}In_{0.53}Ga_{0.235}As$ | 20 | nid |
| 11 | doping plane | InP | 7 | $n = 1 \cdot 10^{18}$ |
| 12 | collector | InP | 100 | nid |
| 13 | sub-collector 1 | InP | 20 | $n = 3 \cdot 10^{19}$ |
| 14 | cathode contact | $In_{0.4}Ga_{0.6}As$ | 10 | $n = 3 \cdot 10^{19}$ |
| 15 | sub-collector 2 | InP | 50 | $n = 3 \cdot 10^{19}$ |
| 16 | etch stop | $In_{0.4}Ga_{0.6}As$ | 10 | $n = 3 \cdot 10^{19}$ |
| 17 | buffer | InP | 17.5 | nid |
| 18 | substrate | InP | | semi-insulating |

Table 4.1: Epitaxial layers of the double collector UTC photodiodes as designed by Dr. Alexandre Beck. n-doping was done with Si, p-doping with Be.

towards the cathode. A different design could have been the combination of transparent anode contact layer ($In_{0.4}Ga_{0.6}As$) together with an $Al_{0.075}In_{0.53}Ga_{0.395}As$ diffusion barrier layer between layers 8 and 9.

The absorption regions are 90 nm thick and have a built-in quasi field for the electrons in the conduction band thanks to a gradual composition change with indium content ranging from 0.46 to 0.6. The conduction band energy difference is approximately 140 meV [1], corresponding to an electric field of approximately 15 kV/cm. Photogenerated electrons are accelerated by this field, and the approximation $\tau_a \approx W_A/v_d$ (see section 1.1.3) is valid. Assuming a mobility of $5000\,cm^2\,V^{-1}\,s^{-1}$, the drift velocity is $7.8 \cdot 10^7$ cm/s, and $\tau_a = 0.12$ ps ($f_a = 1375$ GHz). The velocity is probably overestimated, as saturation effects are not taken into account. When assuming $v_d = 4 \cdot 10^7$ cm/s, $\tau_a = 0.23$ ps and $f_a = 707$ GHz.

The transit time through the transport layer is $\tau_{tr} \approx W_C/v_d \approx 0.5$ ps ($f_{tr} = 886$ GHz),

assuming a drift velocity of $v_\mathrm{d} = 2 \cdot 10^7\,\mathrm{cm/s}$ of the electrons in the 100 nm thick transport layer.

The $RC$ time constant is given by the load resistance $R_\mathrm{L}$, and the device capacitance $C$. Neglecting parasitic resistances, $R_\mathrm{L} = 50\,\Omega$ for on-wafer measurements. As the two photodiodes are in parallel, and assuming that the area of the mesas is uniform, $C$ can be estimated to be $C = 2\varepsilon A/W_\mathrm{C}$, with $A$ the device area. For a device with area $36\,\mu\mathrm{m}^2$, $C \approx 62\,\mathrm{fF}$, assuming $\varepsilon_\mathrm{r} = 12.5$ for InP. The corresponding 3 dB-frequency is $f_\mathrm{RC} \approx 51\,\mathrm{GHz}$. For high-frequency operation, smaller capacitances are necessary. Square devices with sidelengths of 6, 4, 3, and $2\,\mu\mathrm{m}$ are incorporated on the mask, the smallest having $f_\mathrm{RC} \approx 460\,\mathrm{GHz}$. The experimental $f_\mathrm{RC}$ will be lower than that due to parasitic capacitances.

### 4.1.2 Fabrication of double collector UTC photodiodes

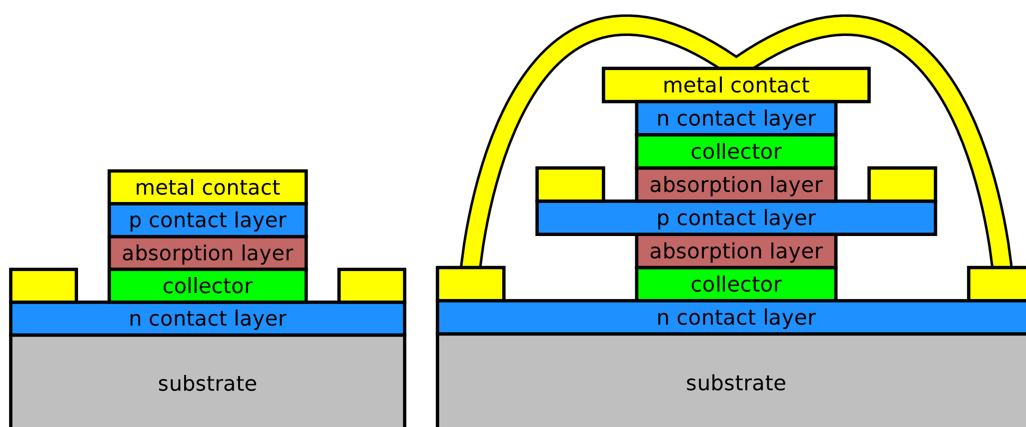


Figure 4.2: Schematic of a standard backside illuminated UTC photodiode (left) and of the fabricated double collector UTC photodiode (right). The two n-contacts of the double collector diode are short-circuited by an air-bridge.

Figure 4.2 shows a schematic of the double collector UTC diode, and that of a standard backside illuminated device for comparison. The diodes are fabricated using wet etching and lift-off techniques. E-beam lithography is used for all patterns. The diodes are integrated with coplanar waveguides (CPW) for on-wafer characterization. The fabrication process is inspired by the process developed for heterojunction bipolar transistors by Dr. Mohammed Zaknoune [6], whose supervision and help during the fabrication of the double collector photodiodes is gratefully acknowledged.

The first step of the fabrication is the metallization of the top cathode contact, followed by the etching of the top diode up to the anode contact, layer 8. InP is etched in $\mathrm{HCl{:}H_3PO_4}$

(5:1), and all As containing layers are etched in $H_3PO_4$:$H_2O_2$:$H_2O$ (5:1:40). In order to obtain a more homogeneous etch, the interfaces between InP and the As containing layers are etched nonselectively for 15 s in $HIO_3$:HCl:$H_2O$ (1:1:100).

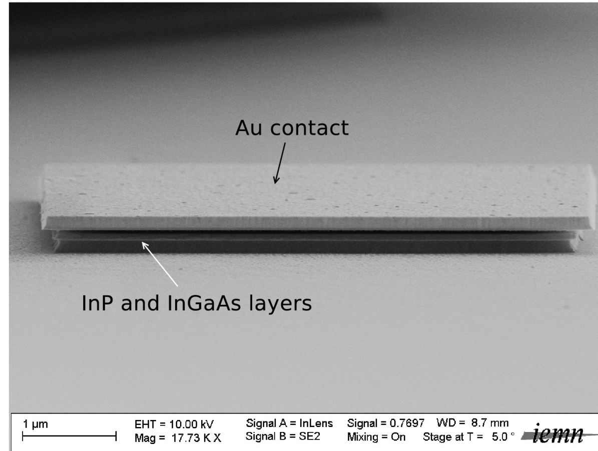


Figure 4.3: SEM image of a 6 $\mu$m diode after cathode metallization and etching of the top diode, layers 1 through 7.

The wet etching of InP in HCl is dependent on the crystal orientation. A well controlled underetch of the diode below the metallic contact is necessary for the intended fabrication process with self-aligned anode contact. A square geometry is therefore chosen for the top cathode contact, and the sides of the square are aligned along the (010) and (001) directions of the InP substrate. A SEM image of the resulting underetch of the top diode is shown in figure 4.3.

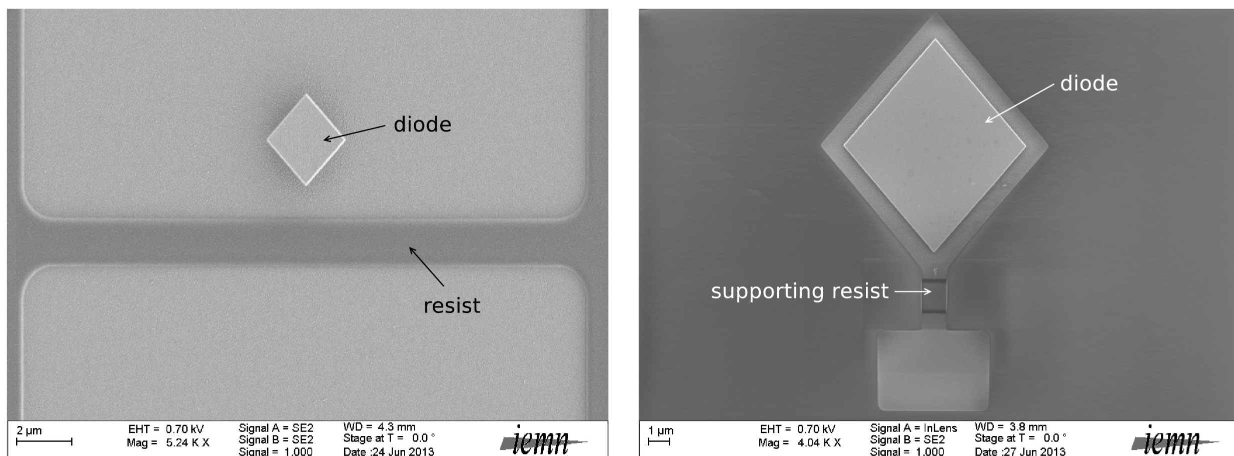


Figure 4.4: Resist patterns for the self-aligned anode contact with access pad. Left image: resist support for the airbridge. Right image: opened resist for lift-off process

The anode contact should be as close as possible to the diodes to reduce the series resistance

and inductance, and should at the same time be relatively narrow ($\approx 500\,\mathrm{nm}$) to allow for good control of the underetch of the bottom diode. Patterning of the resist for direct deposition of the anode contact would be difficult, and a self-alignment technique is used instead. For the self-alignment, the opening in the resist is made as large as the top cathode contact plus the width of the anode contact. During the subsequent metallization, metal is deposited on top of the already metallized cathode contact, and the anode is formed around the cathode contact. This step is possible because of the controlled underetch of the top diode.

As the anode contact is small, connecting it to the CPW with an air-bridge is difficult. A dedicated contact pad is therefore patterned at the same time as the anode. In order to keep the device capacitance small, the contact pad is linked to the anode via airbridge. The airbridge allows for underetching of the epitaxial layers below it with the next etching step.

Two resist patterns are needed for the anode contact, see figure 4.4: First a supporting resist for the airbridge is deposited. It is opened at the bridge contact points. A smooth rise and fall of the airbridge is achieved by creeping the patterned resist for 3 min at 140 °C. The second resist pattern is the opening for the metallization and is composed of a bi-layer for easier lift-off.

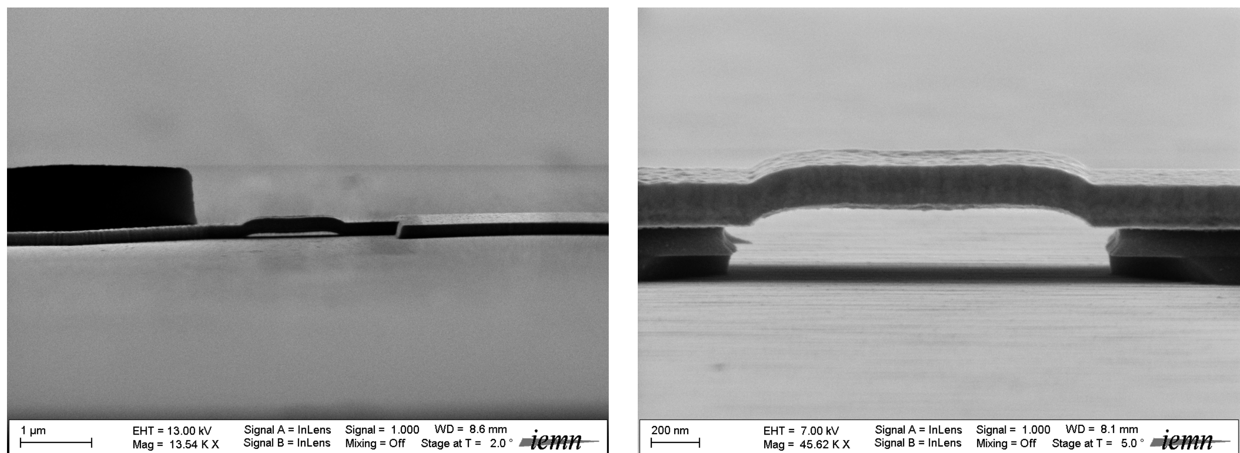


Figure 4.5: Left image: metallized anode contact with airbridge. The diode is protected by resist for the etching of the bottom diode. Right image: Underetched airbridge after etching of the bottom diode.

Shown in figure 4.5 is the fabricated anode contact with the airbridge. The top diode is protected by resist for the etching of the bottom diode, for which the same wet etch process is used as for the top diode. The etching of the As containing layers (layers 8 to 10) has to be controlled by SEM to ensure correct underetch of the air bridge, before the InP layers

11 to 13 are removed as well. SEM images after this etching step are shown in figures 4.5 and 4.6

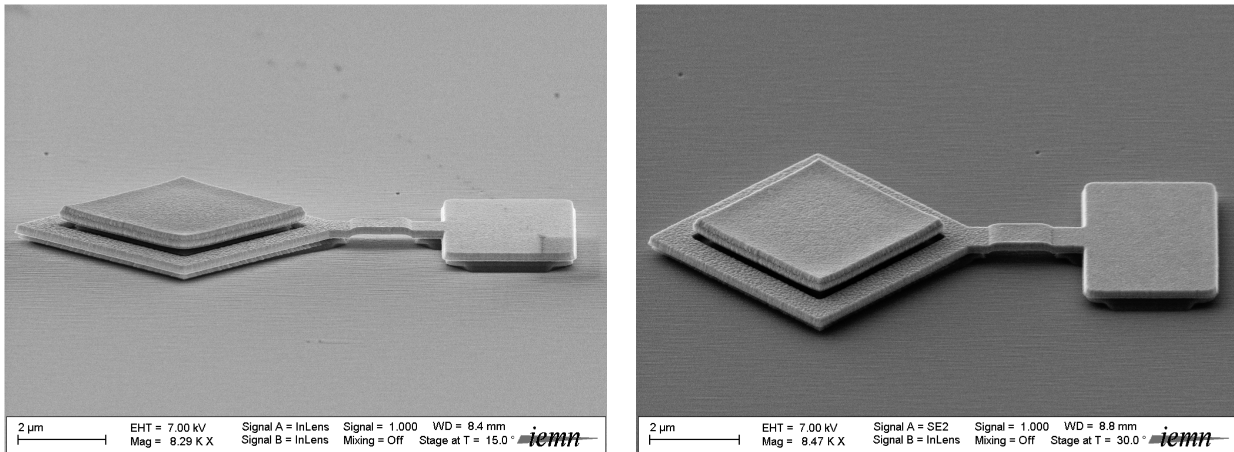


Figure 4.6: SEM images of a 4 $\mu$m sidelength (left) and a 3 $\mu$m sidelength (right) device after etching of the bottom diode.

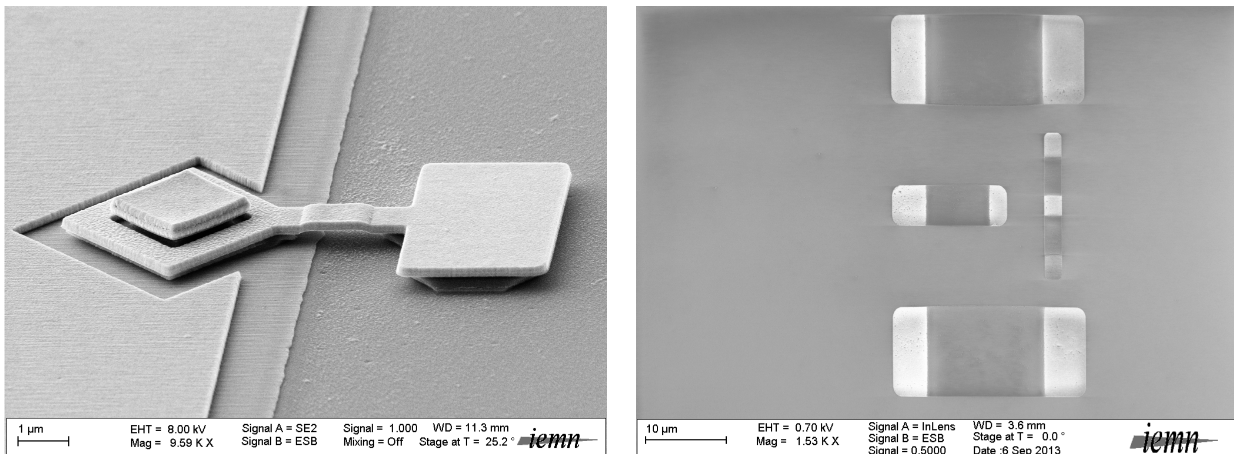


Figure 4.7: Left image: 2 $\mu$m device after metallization of the bottom cathode contact and after the last etching step. Right image: Resist pattern for the airbridges linking the diode to the CPW and short circuiting the two cathode contacts.

The bottom cathode contact is placed around the diode using a standard lift-off technique. Subsequently, the remaining epitaxial layers (layers 14 to 17) are removed by wet etching (figure 4.7), and the CPW access is deposited on the semi-insulating InP substrate.

The last step of the fabrication is the shorting of the two cathode contacts and the connection of the diode to the CPW by airbridges. The resist pattern for the airbridges is again composed of two layers, one for the support of the airbridge and the second for the lift-off process. Cracks in the corners of the second resist pattern occured initially, and were avoided

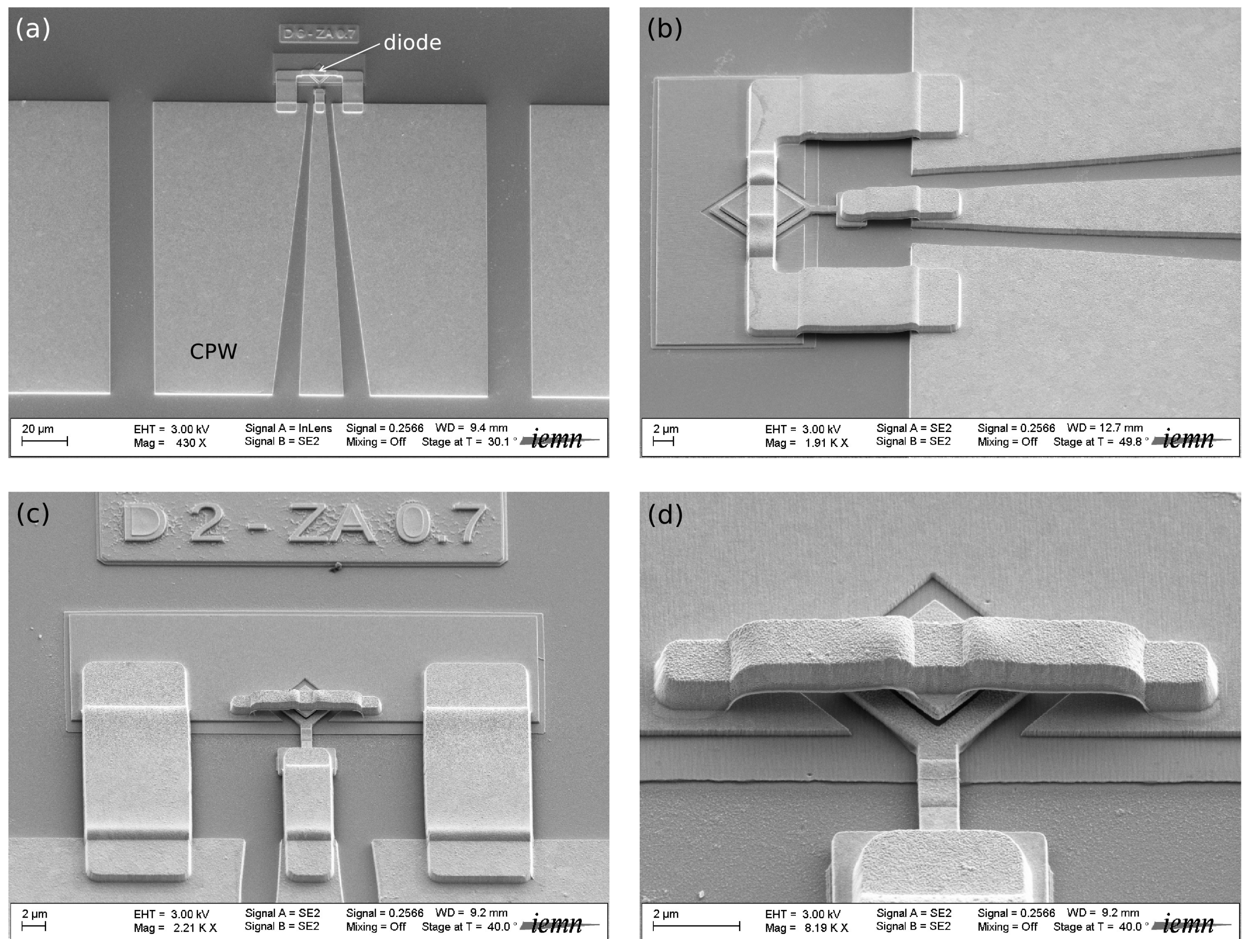


Figure 4.8: SEM images of the fabricated double collector UTC photodiodes. (a) 6 $\mu$m device with CPW access. (b) Close-up of a 6 $\mu$m device. (c) 2 $\mu$m device. (d) 3 $\mu$m device.

by rounding the corners of the pattern. SEM images of the finished devices are shown in figure 4.8.

On-wafer characterization of backside illuminated devices necessitates a special setup that allows to place the coplanar probes on one side of the wafer while allowing to adjust the optics on the backside. Due to the complicated setup, the double collector UTC photodiodes have not been characterized yet. However, fabrication of a suitable wafer support is ongoing.

## 4.2 High efficiency UTC-PDs flip-chip wafer bonded to Si substrate

In the THz photonics group of the IEMN, LTG-GaAs based photoconductors have been fabricated in a vertical configuration with semitransparent top contact and absorption of light in a resonant cavity. These devices have performed very well, generating output powers of 350 $\mu$W at 305 GHz in a broadband configuration [7], and reaching record output powers of 1.8 mW at 250 GHz with an impedance matching circuit [8]. Employing a similar structure for UTC photodiodes may be a promising approach for improved photodiodes.

In this section, the design, fabrication, and characterization of UTC photodiodes transferred to a Si substrate by metallic wafer bonding is reported. The work is closely related to the recent development of a novel semitransparent top contact for UTC diodes during the thesis of Dr. Fabio Pavanello in the THz photonics group [1].

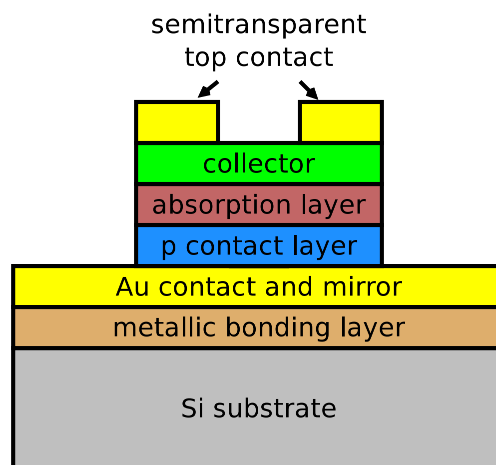


Figure 4.9: Schematic of the transferred UTC photodiodes. The diodes are bonded face down to a Si substrate. A semitransparent top contact is used for front side illumination.

In comparison to the non-transferred devices of the previous thesis, a higher responsivity is expected from the transferred diodes due to the reflection of light at the metallic bonding layer (see figure 4.9). Also, the geometry of the transferred devices allows for a thick metallization of the whole p-contact area, reducing the contact resistance at the anode. The metallization of the cathode contact allows to reduce the spreading resistance compared to standard backside illuminated devices, where the metallic contact is beside the diode (see figure 4.2).

The heat dissipation of the device may also be better due to the heat spreading capabilities

of the bonding layer and the better thermal conductance of the Si substrate [8].

### 4.2.1 Design of UTC photodiodes transferred to Si substrate

The design of the transferred UTC diodes is based on an existing epitaxy. A quarter of the same 2 in wafer that was used in the previous thesis [1] is used. This has the advantage of easier comparison between transferred and non-transferred devices. However, the epitaxy had not been designed for the transferred diodes, making the fabrication more difficult due to thin etch stop layers, and also causing the Fabry-Pérot cavity to be slightly detuned from the resonant thickness.

| No. | Layer | Material | Thickness [nm] | Doping [$cm^{-3}$] |
|---|---|---|---|---|
| 1 | anode contact | $In_{0.4}Ga_{0.6}As$ | 10 | $p = 1 \cdot 10^{20}$ |
| 2 | diffusion barrier | $Al_{0.075}In_{0.53}Ga_{0.395}As$ | 20 | $p = 5 \cdot 10^{19}$ |
| 3 | absorption region (graded composition) | $In_{0.47}Ga_{0.53}As \ldots$ $\ldots In_{0.6}Ga_{0.4}As$ | 150 | $p = 1 \cdot 10^{18}$ |
| 4 | spacer | $In_{0.6}Ga_{0.4}As$ | 10 | $p = 1 \cdot 10^{18}$ |
| | | $Al_{0.235}In_{0.53}Ga_{0.235}As$ | 20 | nid |
| 5 | doping plane | InP | 7 | $n = 1 \cdot 10^{18}$ |
| 6 | collector | InP | 100 | nid |
| 7 | sub-collector 1 | InP | 50 | $n = 3 \cdot 10^{19}$ |
| 8 | cathode contact | $In_{0.4}Ga_{0.6}As$ | 10 | $n = 3 \cdot 10^{19}$ |
| 9 | sub-collector 2 | InP | 300 | $n = 3 \cdot 10^{19}$ |
| 10 | etch stop | $In_{0.4}Ga_{0.6}As$ | 20 | $n = 3 \cdot 10^{19}$ |
| 11 | buffer | InP | 17.5 | nid |
| 12 | substrate | InP | | semi-insulating |

Table 4.2: Epitaxial layers of the transferred UTC photodiodes. The epitaxy is from the same wafer as the one used in the thesis of Dr. Fabio Pavanello [1] and is an improved version of an epitaxy used in the thesis of Dr. Alexandre Beck [9]. n-doping was done with Si, p-doping with Be.

The layers of the epitaxy are listed in table 4.2. It has been designed by Dr. Fabio Pavanello as an improved version of an epitaxy used in a previous thesis in the THz photonics group [9]. The anode contact is highly doped and transparent at 1.55 $\mu$m. The relatively thick absorption region of 150 nm ensures a good responsivity of the devices. A band diagram of the epitaxy is shown in figure 4.10.

The cut-off frequencies are estimated in a similar manner as in section 4.1.1. The time constant of the absorption layer is $\tau_a \approx 0.32$ ps for $v_d = 4.7 \cdot 10^7$ cm/s [1]. The transit

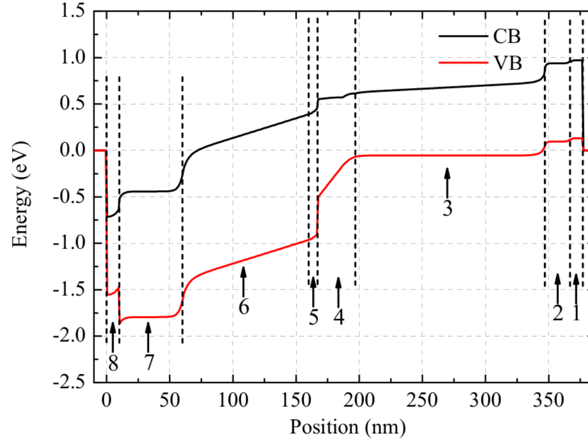


Figure 4.10: Band structure of the epitaxy from table 4.2 [1].

region is the same thickness as in the double collector UTC diodes, and $\tau_{tr} \approx 0.5\,\mathrm{ps}$. The estimated capacitances of square devices with 3, 4, and 6 $\mu$m sidelength are 8.6, 14.3, and 31.1 fF, respectively, without taking into account parasitic capacitances. The corresponding RC cut-off frequencies under a 50 $\Omega$ load are 370, 223, and 102 GHz, respectively.

### Choice of the anode contact metallization

An important aspect for the operation at high frequencies is the series resistance due to the metallic contacts. The series resistance is composed of the resistance of the metal itself, which can be made very small by using sufficiently thick metallizations, and the contact resistance between metal and semiconductor, as well as the series resistance in the semiconductor. The contact resistance can be reduced by a high doping concentration in the semiconductor, which decreases the width of the depletion region between semiconductor and metal and makes tunneling of charge carriers across the barrier more probable [10]:

$$R_\mathrm{c} \sim \exp\left(\frac{4\sqrt{m_\mathrm{h}\varepsilon}\phi_\mathrm{B}}{\sqrt{N_\mathrm{A}}\hbar}\right) \tag{4.1}$$

where $R_\mathrm{c}$ is the contact resistance, $q\phi_\mathrm{B}$ the energy difference between the Fermi level and the valence band at the semiconductor surface, and $N_\mathrm{A}$ is the p-doping concentration.

In the transferred devices, the anode metallization not only serves as electric contact, but also as mirror for the 1.55 $\mu$m light. Gold ($n = 0.18 - 10.21j$) is a very good mirror on InGaAs and InP at these wavelengths, with over 90% reflectance.

It has also been shown that Gold forms low resistance Ohmic contacts on p-doped InGaAs:

Vandenberg *et al.* have found a specific contact resistance of $7 \cdot 10^{-6}\,\Omega\,\mathrm{cm}^2$ for Au contacts on p-$In_{0.53}Ga_{0.47}As$ doped with Zn at a concentration of $4 \cdot 10^{18}/\mathrm{cm}^3$ [11]. A significantly lower contact resistance can be expected for the transferred diodes according to equation (4.1) thanks to the higher doping concentration of $1 \cdot 10^{20}/\mathrm{cm}^3$. Assuming that the higher doping concentration reduces the contact resistance by a factor of 10, the contact resistance of a $9\,\mu\mathrm{m}^2$ device is $7.8\,\Omega$. The voltage drop across the contact for a current of 10 mA is then 78 mV with less than 1 mW dissipated in the contact, which is suitable for high speed and high power operation of the diode. The contact resistance would however reduce the quality factor of an impedance matching circuit for maximum output power at a given frequency.

It is known that Au diffuses into the InGaAs layer already at temperatures between 150 °C and 250 °C under the formation of $Au_3In_2$ and polycrystalline GaAs [11]. The contact then remains stable up to 350 °C [11]. The longterm stability of an Au on InGaAs contact might not be given, and the contact might deteriorate during device operation under high power and high temperature.

Another interesting anode metallization would be a contact composed of a thin Pt layer ($\sim 10$ nm) followed by optically thick Au. A very good contact resistance of $5.3 \cdot 10^{-7}\,\Omega\,\mathrm{cm}^2$ has been found for such a metallization on a similarly p-doped InGaAs layer [1], and it has also been shown that Pt serves as an efficient diffusion barrier in this configuration [12]. On the other hand, the Pt layer would decrease the reflectance of the mirror.

The reflectances of Au and Pt/Au contacts on InGaAs have been calculated using the transfer matrix method (see section 3.2.1). For Au on InGaAs ($n = 3.55 - 0.12j$), a reflectance of 91.2% is found, while a 10 nm Pt layer ($n = 5.31 - 7.04j$) reduces the reflectance to 61.9%. This low reflectance means that a significant portion of the incident light would be absorbed in the contact and heat the device. The responsivity of the device would also be reduced because less light is reflected for a second pass in the absorption region.

A pure Au metallization is therefore chosen for the anode contact, despite the known tendency of Au to diffuse into InGaAs. The thickness of the Au layer is designed to obtain the desired optical properties; the low electrical series resistance is assured by the several 100 nm thick metallic bonding layer underneath. A 75 nm Au layer is larger than 6 times the penetration depth $\delta = \lambda_0/(4\pi k) \approx 12.1$ nm of $1.55\,\mu$m light in Au, and is therefore optically thick and sufficient as anode contact.

### Semitransparent cathode contact

For front-side illumination of the transferred photodiodes, a semitransparent top contact is needed. On vertical LTG-GaAs based photoconductors, a thin Au film (10 nm... 20 nm) has proven to be a suitable semitransparent contact [13]. However, UTC photodiodes based on InP/InGaAs work at 1.55 $\mu$m laser wavelength instead of 800 nm for LTG-GaAs photoconductors. The optical properties of Au at 1.55 $\mu$m, with a high absorption coefficient ($n = 0.18 - 10.21j$), makes thin continuous Au layers less well suited as semitransparent contacts at these wavelengths.

During the previous thesis in the THz photonics group, a novel type of semitransparent contact has been developed [1]. This contact is based on the extraordinary transmission of light passing through subwavelength apertures. Due to the extraordinary transmission phenomenon, the contact can have a higher transmittance $T$ than would be expected from the ratio $\gamma = A_\mathrm{m}/A$ of metallized surface area $A_\mathrm{m}$ to total surface area $A$: $T > (1 - \gamma)$.

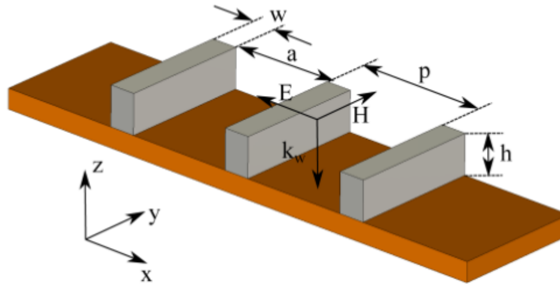


Figure 4.11: Geometry of the semitransparent cathode contact, from [1].

The contact developed in the previous thesis is composed of parallel metallic strips of width $w$ and height $h$, with a distance $a$ between strips, see figure 4.11. Two sets of parameters $w, h, a$ have been identified as especially suitable for UTC photodiodes. Both sets have a metallization height $h = 300$ nm, and a period $p = w + a = 1\,\mu$m, with the strip width $w$ being 300 nm or 500 nm.

In the previous thesis, non-transferred UTC photodiodes with these contacts have been fabricated and characterized. At small diode sizes, the diodes with $w = 300$ nm reached slightly higher responsivities than those with $w = 500$ nm (46 mA/W vs. 41 mA/W for diodes with 3 $\mu$m sidelength). For larger diodes, devices with $w = 500$ nm showed higher responsivities (75 mA/W vs. 66 mA/W for 6 $\mu$m diodes). Both types of contacts have been proven to be suitable for UTC diodes, with a maximum power of 400 $\mu$W generated a 300 GHz for a device with 3 $\mu$m sidelength [1].

The same type of contacts is therefore included in the mask for the transferred diodes. Some strips are metallized with 300 nm Au, as Au behaves close to a perfect electrical conductor (pec) in what concerns the optical properties of the strips [1]. Other devices are fabricated with strips composed of 20 nm Pt and 280 nm Au, where the Pt serves as diffusion blocking layer between the InGaAs contact and Au. Additionally, devices with a thin Au layer (10 nm) below the Au strip contacts are fabricated in order to reduce the contact and series resistances.

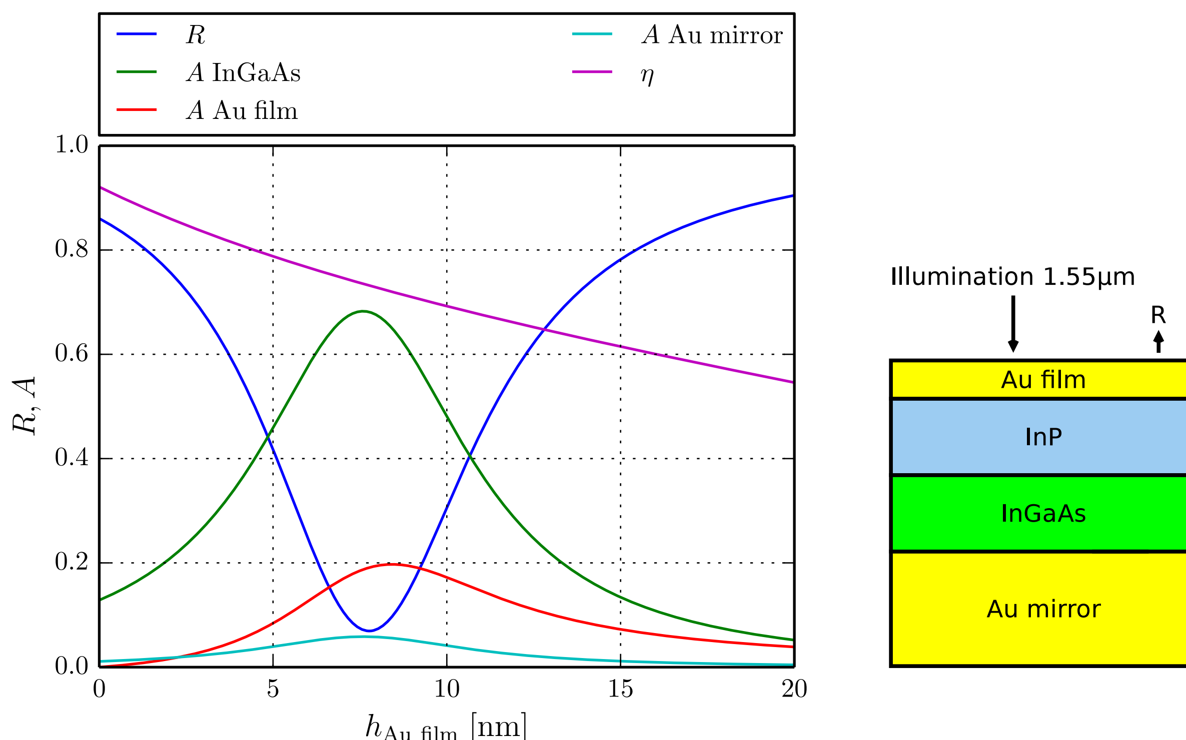


Figure 4.12: Reflectance and absorbance in the different layers of the transferred UTC diode in dependence of the height of the top continuous Au layer. The parameter $\eta = A_{\text{InGaAs}}/(1-R)$ is the fraction of the total absorbed radiation that is absorbed in the active InGaAs layer.

Calculations using the transfer matrix method have shown that, even though less suited than at 800 nm wavelengths, a thin Au layer can still work as cathode contact. Plotted in figure 4.12 are the fraction of radiation absorbed in the InGaAs absorbing region and in the Au contacts for thin top Au contacts with various thicknesses. The model used for the calculations is based on the epitaxial structure in table 4.2, with all transparent InGaAs layers modeled by using only the real part of the refractive index of $In_{0.53}Ga_{0.47}As$. The maximum absorption in the InGaAs layer is obtained for a 7 nm thick Au layer. In order to ensure a continuous layer, a thickness of 10 nm has been chosen, which still yields ≈ 50%

total absorption in the InGaAs layer, with 70% of all absorbed radiation absorbed in the active layer.

Also, for comparison purposes, devices without metallic contact layer on the diode surface are produced. Due to the high doping ($3 \cdot 10^{19}\,\mathrm{cm}^{-3}$) of the cathode contact layer, current flow to the Pt/Au metal contact on the side of the device is still possible. However, a high series resistance (contact resistance and conduction in the contact layer) is expected for these devices.

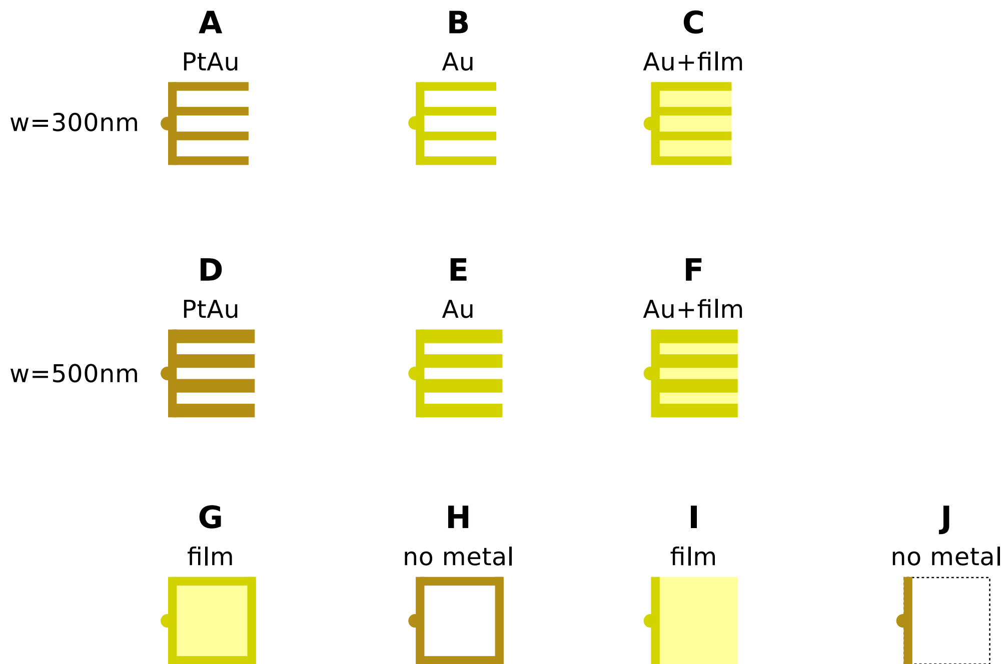


Figure 4.13: Types of cathode contacts included on the mask. Types A-C are strip contacts with strip width $w = 300\,\mathrm{nm}$ and metallizations of 20 nm Pt – 280 nm Au (A), 300 nm Au (B) and 10 nm Au film, 300 nm Au (C). Types D-F are like A-C but with strip width $w = 500\,\mathrm{nm}$. Finally devices without strips are included (G-J), with thin Au film or without, and contact around the diode mesa, or only on one side of the diode. The contacts of devices G and I are metallized with 300 nm Au, and H and J are metallized 20 nm Pt – 280 nm Au.

Figure 4.13 lists the different types of cathode metallizations that are included on the mask. For each type of contact, devices with 10, 6, 4, and 3 $\mu$m sidelength are fabricated. In this thesis, the characterization of A, B, C, G, and H type diodes is reported, while the other contact types had to be omitted due to time constraints.

### 4.2.2 Device fabrication

Device fabrication starts with the metallic bonding of the epitaxial layers to a Si substrate. The process for bonding is described in section 2.1.1. An In–Au bonding at 180 °C is chosen, as that is the lowest temperature at which good bonding results have been achieved. The temperature is chosen as low as possible to minimize diffusion, especially between the Au layer and the anode contact layer. The following metallizations are prepared: Si substrate – 100 nm Ti – 15 nm Pt – 75 nm Au, and Epitaxy – 75 nm Au – 15 nm Pt – 75 nm Au – 300 nm In. The first Au layer on the anode serves as contact and mirror as discussed in section 4.2.1. The Pt layers serve as diffusion barrier for the In–Au bonding layer (section 2.1.4). The Ti layer on the Si substrate serves as adhesion layer. Studies on the etching of the In–Au bonding were still ongoing when the fabrication of the diodes was started, and a thick Ti layer seemed the best choice for the etching (section 2.1.5). For the fabrication of transmission lines on $SiO_2$ that was ultimately used, a thinner metallization ($\sim 20$ nm) would have been sufficient.

After bonding, the InP substrate is etched in diluted HCl (1:2 $H_2O$:HCl). The side borders of the InP substrate are protected with resist to prevent any influx of acid between the substrates at possible bonding defects. As the epitaxy had not been designed with bonding in mind, only a 20 nm InGaAs etch stop layer (layer 10) is included to stop the etch of the 360 $\mu$m thick substrate. Great care is taken to decrease the etch speed towards the end, and the etching is interrupted several times to protect already exposed parts of the etch stop layer with resist. Nevertheless, after etching of the substrate holes in the epitaxy are visible with an optical microscope.

The diode fabrication in the next steps has many similarities with the fabrication of the double collector UTC photodiodes. Again, the expertise and help of Dr. Mohammed Zaknoune in the fabrication process are much appreciated. A first etching process removes layers 10 and 9, as the sub-collector is not needed in the transferred device geometry. The different top contacts described in section 4.2.1 are then placed on the cathode contact layer (layer 8). For the fabrication of the high aspect ratio slits, the same process as described in [1] is used. The diodes are protected by resist, and all remaining layers are etched, stopping on the Au layer.

As the attempts to etch the In–Au bonding layer have not been successful (section 2.1.5), the transmission lines to contact the devices are fabricated on $SiO_2$ instead of directly on the substrate. The process has been developed by Dr. Emilien Peytavit and employed for coplanar probe testing of transferred LTG-GaAs photoconductors [14]. First, a 20 nm Ti layer is deposited for better adhesion of the $SiO_2$ layer. The devices are then protected by

resist, and 2.3 $\mu$m $SiO_2$ is deposited on the whole wafer. A further resist layer protects $SiO_2$ from being etched at the coplanar probe contact areas during the $SiO_2$ etching step by RIE in $CF_4/CHF_3$ plasma.

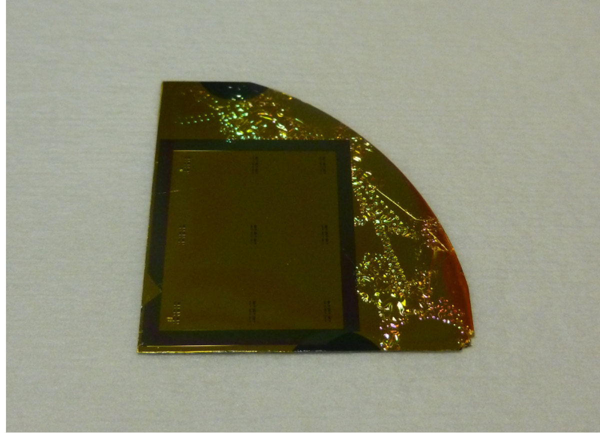

Figure 4.14: Photograph of a test sample (quarter of a 2 in wafer) for the process of transmission line fabrication on $SiO_2$. The ability of the Ti rectangle to stop propagation of cracks in the $SiO_2$ layer is visible.

Preliminary tests of the $SiO_2$ deposition and etching process have shown that the $SiO_2$ layer is very fragile before etching, and that cracks quickly expand to large surfaces ($mm^2$ to $cm^2$). On the transferred diodes, edges of the initial InP substrate remain after etch due to the anisotropy of the InP etch in HCl, and cracks in the $SiO_2$ layer have to be expected at these defects. As shown in figure 4.14, the cracks propagating from the border of the wafer can be stopped effectively by surrounding the device area with a ring of a 20 nm Ti layer. A similar protective Ti ring has been used around the device area of the transferred diodes.

As last step after etching the $SiO_2$ layer, the coplanar waveguides are fabricated on the $SiO_2$ pads and connected to the devices via airbridge using a similar process as described in section 4.1.2. The e-beam lithography of this step had to be done on a different e-beam writer because the machine used for all other steps was in maintenance for nearly two months. Alignment problems between this last layer and the devices were noticed. However, the problem was reproducible in a second attempt of writing the layer, using different alignment markers. The amount of misalignment depends on the position on the wafer, with some fields (repetition of the base mask cell) written correctly and larger misalignments in other fields.

SEM images of the finished diodes are shown in figure 4.15.

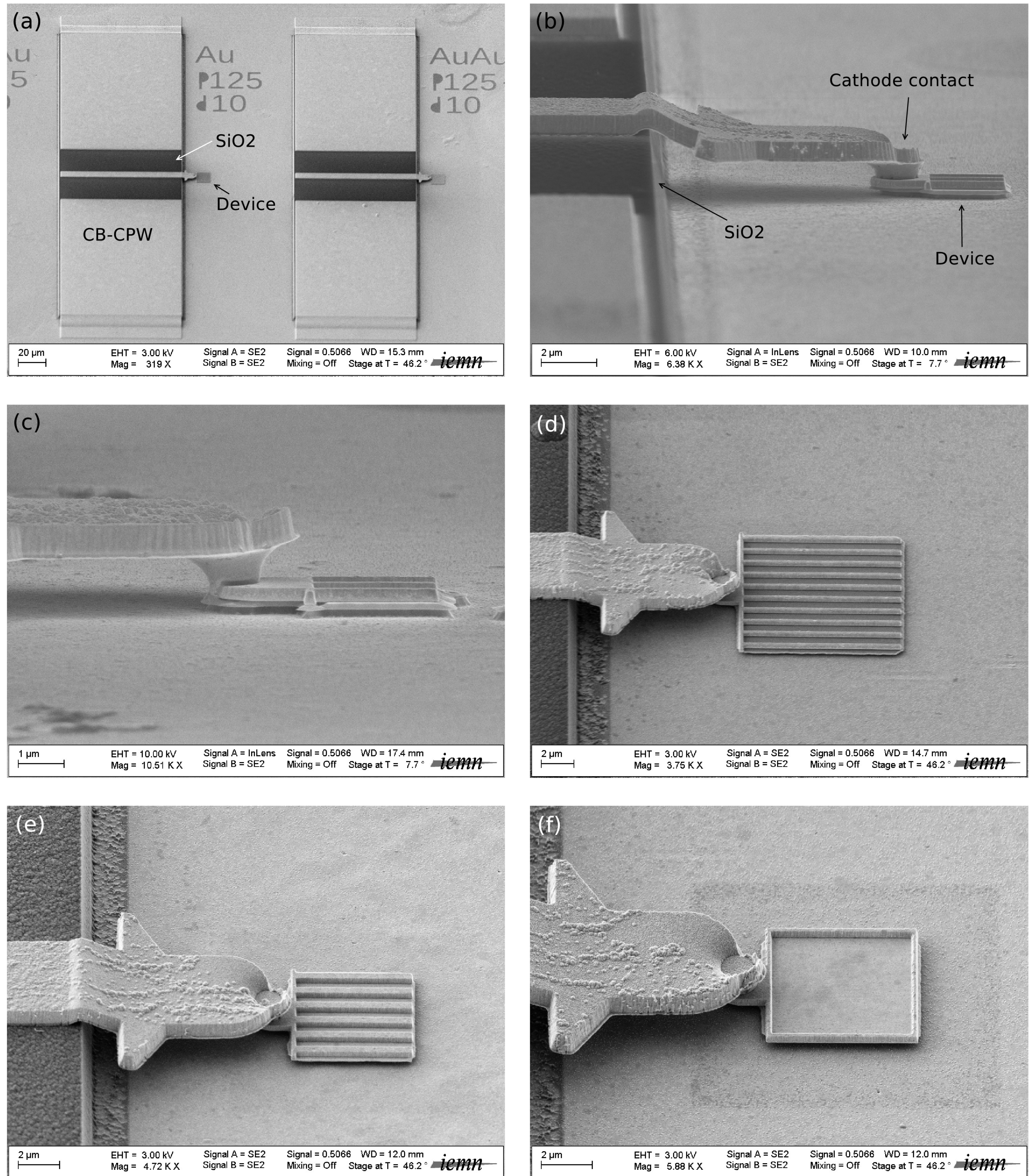


Figure 4.15: SEM images of the fabricated UTC photodiodes transferred to Si substrate. (a) CB-CPW on $SiO_2$ and contact by airbridge to the device and the groundplane. (b) airbridge contacting an A3 type device. (c) B3 type device with alignment problems between airbridge and device (see text). (d), (e), (f) diodes of types B10, F6, G6.

### 4.2.3 Photodiode characterization

On-wafer characterization of the transferred UTC PDs in the frequency range of a WR-3 waveguide (220 GHz - 325 GHz) is performed. The measurement setup is based on an existing photomixing setup with 1.55 $\mu$m lasers. Dr. Guillaume Ducournau, Dr. Antoine Pagies, and Dr. Jean-François Lampin helped with the installation of the setup and during measurements.

#### Experimental setup

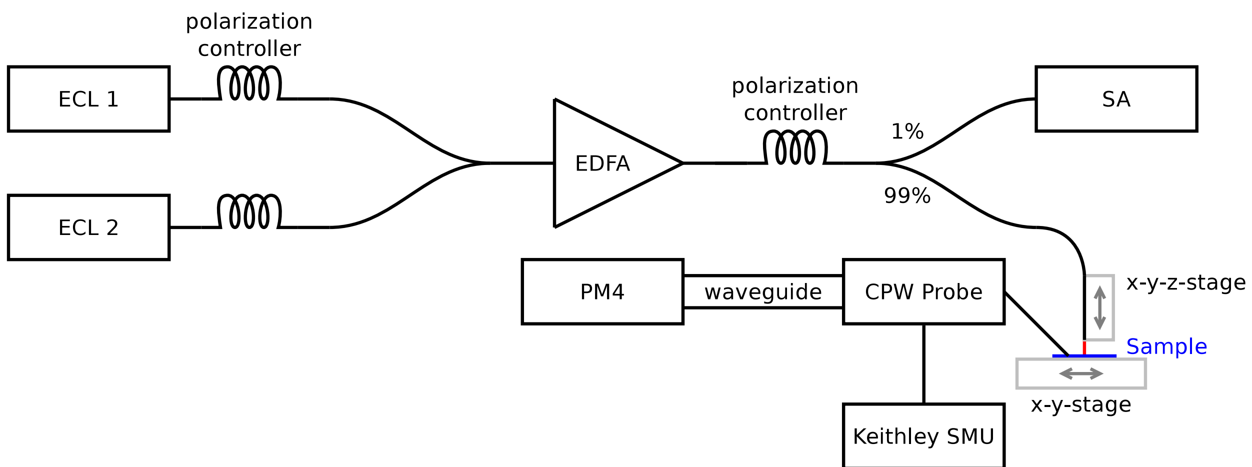


Figure 4.16: Setup used for the on-wafer characterization of the transferred UTC photodiodes.

The optical part of the setup (figure 4.16) is completely fibered, with the exception of a short free space path intended for the placement of filters and also useful for blocking the laser. Two external cavity lasers are used as sources for the two frequencies. Polarization controllers after each laser allow to align their polarization. The lasers are then coupled into one fiber and the signal is amplified by an erbium doped fiber amplifier (EDFA). An additional polarization control stage allows the alignment of the polarization of the two lasers perpendicular to the fingers of the semitransparent top contacts of the devices. A 99/1 coupler is used to couple 1% of the power to a wavemeter, which is used to verify the spectrum, the difference frequency of the lasers, and the relative power of the two laser lines. The relative power of the laser lines depends on the wavelength of the lasers because of the wavelength dependent gain of the EDFA. A maximum difference of 1 dB is maintained during RF measurements. The remaining 99% of the laser power is used to illuminate the device with a lensed fiber with a minimum spot size of 3 $\mu$m, see figure 4.17. The losses

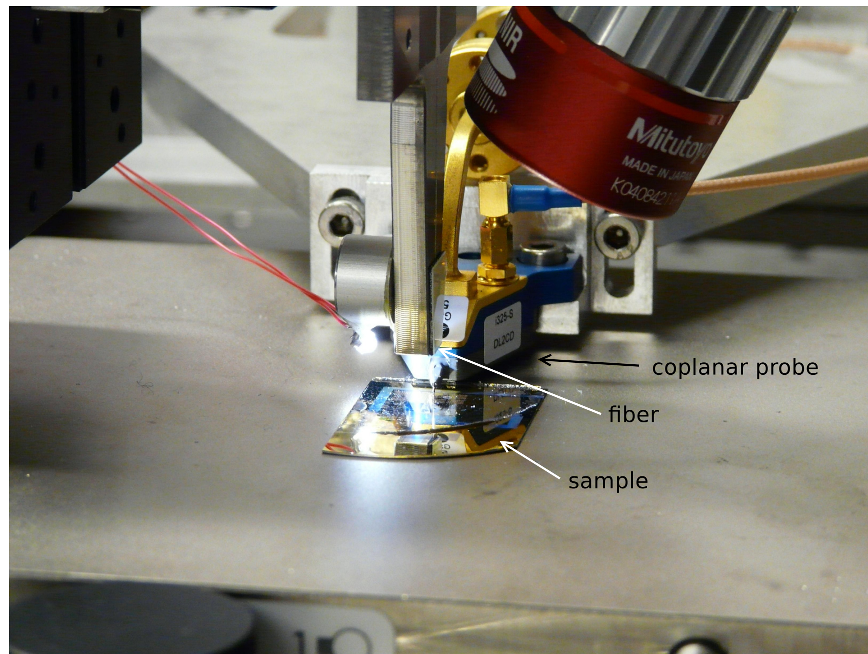


Figure 4.17: Photograph of the sample being connected by the coplanar probes and illuminated from a lensed fiber.

between the EDFA and the fiber output reach 6.4 dB according to measurements of the optical power with a power meter.

On the electric side of the setup, coplanar probes with integrated bias-T (Cascade microtech) are used to contact the sample. The dc output of the bias-T is connected to a source meter, which is used to bias the device and to measure the photocurrent. The RF output of the probes has a WR-3 interface. A WR-3 to WR-10 taper and a 15 cm long WR-10 waveguide are used to connect an Erickson PM4 power meter, which has a WR-10 input. Propagation in the WR-10 waveguide is multimode in the measurement frequency range, but due to the taper the fundamental mode is mainly excited, and if some higher order modes are excited, this is not an issue for the calorimetric power detection. A photograph of the RF propagation part of the setup is shown in figure 4.18.

The measurements of the RF power are corrected for losses. These are composed of the losses of the coplanar probe, of taper and waveguide, and inside the PM4 power meter. The losses of the coplanar probe have been measured by the manufacturer and are between 2.7 dB and 4.2 dB in the WR-3 frequency range (220 − 325 GHz). They reach 3.8 dB at 300 GHz. The losses of taper and waveguide have been measured by Dr. G. Ducournau using a vector network analyzer (VNA). Taper and waveguide have been left joined together to avoid additional uncertainties due to a possibly different connection. The VNA has been connected

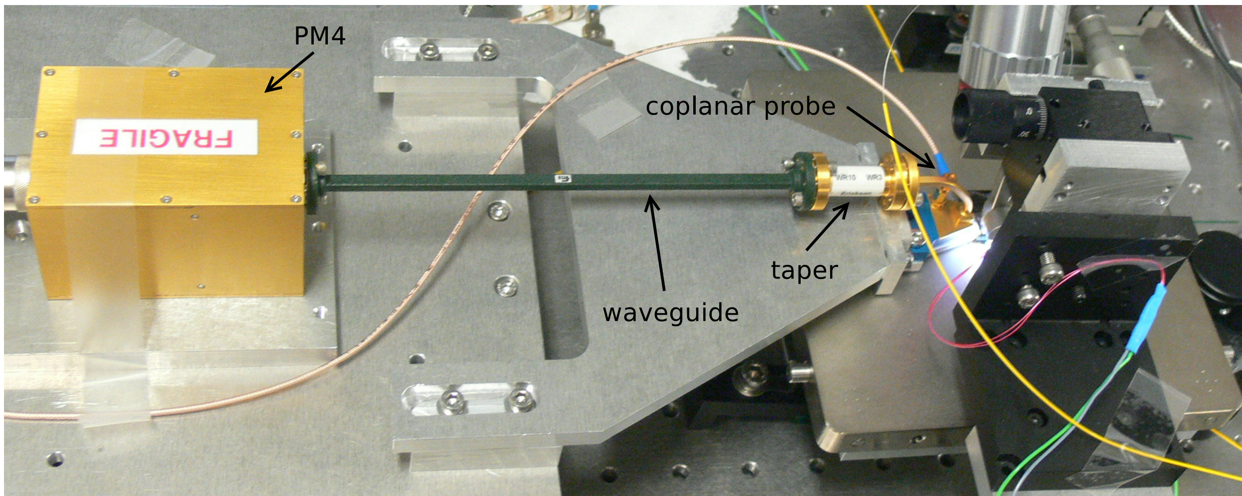


Figure 4.18: Photograph of the RF part of the setup for photodiode characterization.

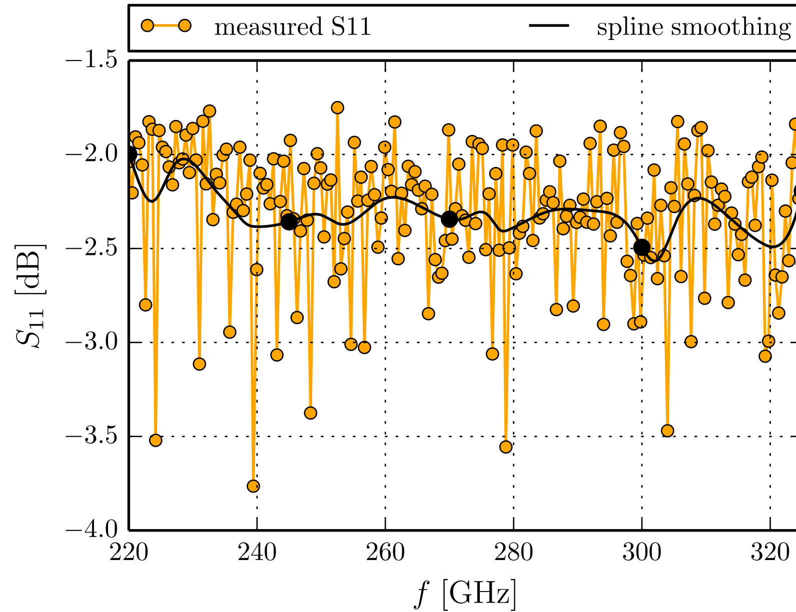


Figure 4.19: Losses of taper and waveguide, connected to a short-circuit, measured using a VNA. Spline smoothing of the noisy measurement is used to deduce the correction factor for RF measurements.

to the WR-3 port of the taper, and a short circuit has been put on the output of the WR-10 waveguide. The measured $S_{11}$ parameter is plotted in figure 4.19. As the measurement is relatively noisy, smoothing of the data using a spline of degree 3 is performed, and the losses at the measured frequencies are obtained from the spline. The frequencies at which the devices were characterized are marked by dots on the spline in figure 4.19. The RF power measurements are corrected by $S_{11}$[dB]/2. Finally, the losses inside the PM4 power meter are 0.2 dB, as given by the manufacturer.

### DC characteristics of the photodiodes

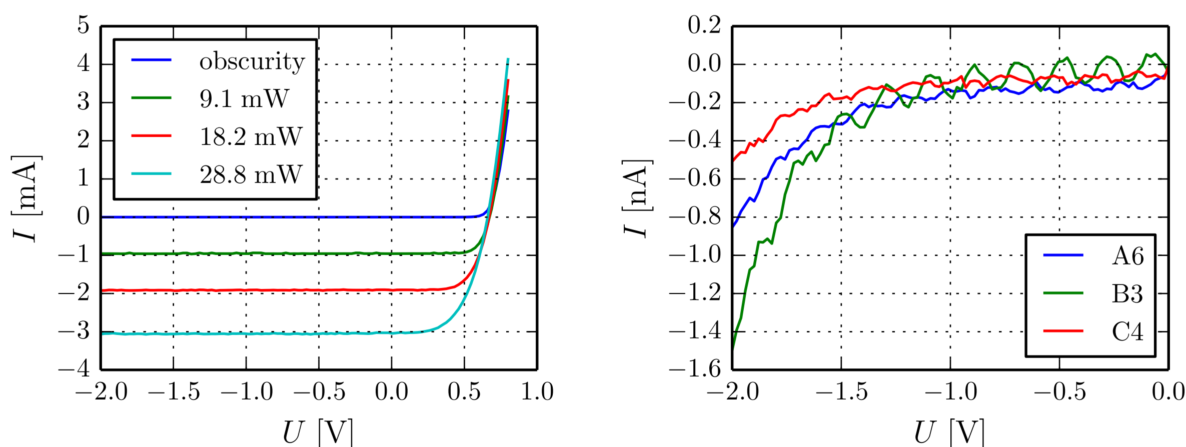


Figure 4.20: Current-voltage curves of the transferred photodiodes. Left image: I-V curves in dependence of the optical power for a B3 type device. Right image: dark currents of different devices.

The first measurement after contacting a device with the coplanar probe is an I-V measurement to verify the diode-like behavior. This assures that the device has been contacted correctly and can quickly identify some problems with the device, such as a short circuit. I-V curves are taken without illumination and at optical powers of 9.1 mW, 18.2 mW, and 28.8 mW, see figure 4.20.

The leakage current at reverse bias can also give information about problems in the fabrication of a particular device. The dark current of the diodes remains typically smaller than 1 nA up to −1.5 V, and remains below 3 nA at −2 V, see figure 4.20. No trend in the leakage current could be observed depending on device size or cathode contact type. Some devices were measured in the field 1,3 on the wafer with alignment problems during fabrication (see section 4.2.2). The A4 type device in this field reached 1 $\mu$A leakage current at −2 V reverse bias, considerably higher than any other of the measured devices.

| Device | $R$ [mA/W] | cathode contact |
|---|---|---|
| A6 / A4 / A3 | 133 / (155) / 100 | Pt/Au strips |
| B6 / B4 / B3 | 160 / 121 / 103 (121) | Au strips |
| C6 / C4 / C3 | 55 / 54 / (69) | Au film and strips |
| G6 | 34 | Au film, Au contact on border |
| H6 | 127 | Pt/Au contact on border |
| a6 / a4 / a3 | 66 / 62 / 46 | Pt/Au strips |

Table 4.3: Responsivities measured at $U = -1\,\text{V}$. The last line shows the responsivities obtained for non-transferred devices with the same semitransparent top contact as the A type devices [1]. Values in parentheses are from devices in field 1,3 on the wafer with alignment problems during the fabrication. The last column describes the top contact type for convenience, which is detailed in figure 4.13.

The responsivity $R = I/P_{\text{opt}}$ of the device can be calculated from current measurements under illumination. In small signal operation, the linear relationship between $I$ and $P_{\text{opt}}$ is well maintained. At a given voltage $U$, the responsivity of a device is calculated by linear fit to the three ($I$, $P_{\text{opt}}$) pairs from the current-voltage measurements, see figure 4.21. For the small optical powers below 30 mW, no deviation from the linear behavior is observed at a bias of $U = -1\,\text{V}$. Table 4.3 summarizes the responsivities of the measured devices.

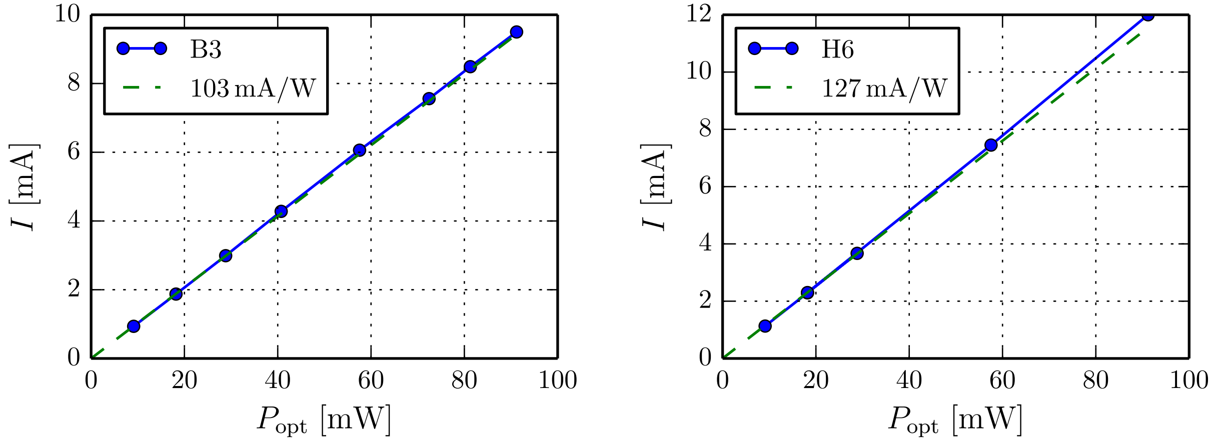


Figure 4.21: Photocurrent in dependence of optical power $P_{\text{opt}}$ at a bias of $-1\,\text{V}$ for a B3 and an H6 type device. The responsivity is calculated from a linear fit to the first three measured points.

Higher responsivities are measured for larger devices. This is due to the minimum spot size of the lensed fiber of $3\,\mu\text{m}$, which implies that only part of the impinging light is focused on

the smaller diodes.

The lowest responsivities are obtained for diodes with the 10 nm Au layer (types C and G). This can be explained by the high reflectance of the Au layer and the absence of an antireflection coating. The responsivities of the other devices are comparable, with the B type devices (Au finger contacts) having higher responsivity than the A type devices (Pt/Au finger contacts). The responsivity of the H6 device (Pt/Au contact only on the circumference of the device) is almost as high as that of the A6 device. This shows that the series resistance of the highly n-doped contact layer does not degrade the dc characteristics.

Responsivities of the 3 devices measured in field 1,3, where the alignment problems between airbridge and device are noticeable, are substantially higher than comparable devices in other fields. From the SEM images (figure 4.15 (c)) it appears that the airbridge to the transmission line contacts the diagonally etched InP transport layer directly, with part of the airbridge contact close to the absorption region. It is thought that this changes the distribution of the electric field in the transport layer, and increases the leakage current.

It is interesting to compare the A-type devices with non-transferred devices with the same top contact geometry. Such devices have been characterized in the earlier thesis [1]. A 2-times increase in responsivity is found for the transferred devices (see table 4.3). This means that the reflectance of the Au groundplane is high. If the absorbed power is from only two passes in the absorption layer with lossy reflection at the Au groundplane in between, an increase in responsivity of 79% over the non-transferred devices is expected. The slightly higher increase in responsivity may be due to the different metallization (20 nm Pt – 280 nm Au on the transferred diodes and 50 nm Pt – 250 nm Au on the non-transferred devices), or partial reflection of the light at the semitransparent top contact, or a combination of both.

Figure 4.21 also shows the behavior of $I(P_{\mathrm{opt}})$ for two devices at higher optical power. The photocurrent at high optical powers is slightly higher than the extrapolation of the linear small-signal behavior. The same effect has been observed in a more pronounced fashion on the non-transferred devices and has been attributed to bandgap shrinking and stronger light absorption in the absorption layer due to the heating of the device [1].

### RF characterization of the photodiodes

According to equation (1.19), the output power of UTC photodiodes is proportional to the square of the modulated photocurrent $I_{\mathrm{ac}}$. $I_{\mathrm{ac}}$ is difficult to measure, but at a given frequency $f$, the ratio between modulated and dc photocurrent is constant, $I_{\mathrm{ac}}/I_{\mathrm{dc}} = \mathrm{const.}$ The output power is therefore proportional to the square of the measured dc photocurrent.

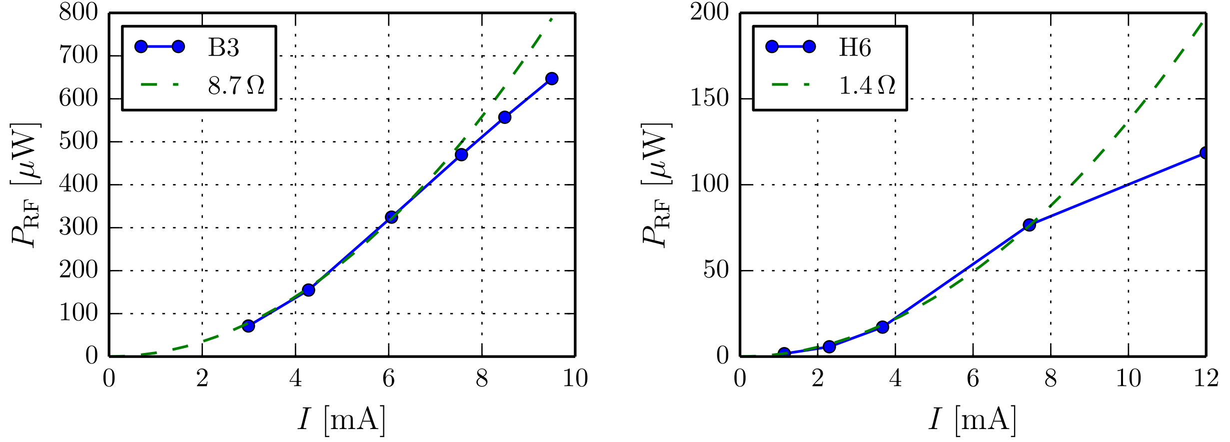


Figure 4.22: RF power at 300 GHz in dependence of the photocurrent at a bias of −1 V. The devices are the same as in figure 4.21. The quadratic fit is computed from the first three data points for the B3 device and from the first four points for the H6 device.

| Device | $r$ [Ω] | cathode contact |
|---|---|---|
| A6 / A4 / A3 | 1.9 / (2.8) / 6.1 | Pt/Au strips |
| B6 / B4 / B3 | 2.2 / 5.1 / 8.7 (6.9) | Au strips |
| C6 / C4 / C3 | 2.2 / 5.8 / (7.1) | Au film and strips |
| G6 | 2.2 | Au film, Au contact on border |
| H6 | 1.4 | Pt/Au contact on border |

Table 4.4: Fit parameter $r$ given by $r = P_{\mathrm{RF}}/I_{\mathrm{dc}}^2$ at 300 GHz and −1 V. Values in parentheses are from devices in field 1,3 on the wafer with alignment problems during the fabrication.

At low optical powers, the quadratic dependence is well maintained (see figure 4.22), and the proportionality factor $r$, given by $P_{\mathrm{RF}} = rI_{\mathrm{dc}}^2$, can be extracted from the measurements. The fit parameters $r$ at 300 GHz and −1 V are listed in table 4.4.

Generation of RF power at 300 GHz is more efficient (larger $r$) for the small photodiodes. This is due to the RC roll-off of the larger devices, as the ratio $I_{\mathrm{ac}}/I_{\mathrm{dc}} \sim \frac{1}{\sqrt{1+(2\pi f R_{\mathrm{L}} C)^2}}$ is reduced by the higher capacitances of the larger devices.

The comparison of $r$ for different contact types for devices of the same size is very interesting, because it eliminates the effect of the different responsivities, and makes an analysis of the effect of the metallization of the cathode contact on the efficiency of RF generation possible. As the $r$ parameters have been deduced in small-signal mode, any saturation or device

heating effects are assumed to be negligible.

It is notable that according to table 4.4, differences in the parameter $r$ depending on the cathode contact geometry and metallization can be observed. Moreover, the difference in $r$ seems to be more important at smaller diode sizes. This fact merits a more detailed inspection.

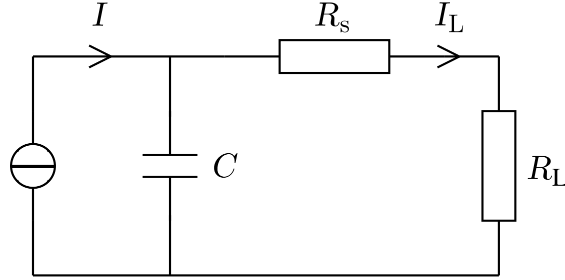


Figure 4.23: AC equivalent circuit of a UTC photodiode with series resistance $R_\mathrm{s}$.

The circuit schematic shown in figure 4.23 is a model of the photodiode as ac current source. A series resistance $R_\mathrm{s}$ is included to model the contact resistance of the cathode. The current through the load, $I_\mathrm{L}$, is given by

$$I_\mathrm{L} = I \frac{Z_\mathrm{C}}{R_\mathrm{s} + R_\mathrm{L} + Z_\mathrm{C}}$$

with $Z_\mathrm{C} = 1/i\omega C$ the impedance of the device capacitance $C$. The RF power is proportional to the square of the load current:

$$P_\mathrm{RF} = \frac{1}{2} R_\mathrm{L} \left| I_\mathrm{L} \right|^2 = \frac{1}{2} R_\mathrm{L} I^2 \frac{1}{1 + \big(\omega C (R_\mathrm{L} + R_\mathrm{s})\big)^2}. \tag{4.2}$$

It is useful to rewrite the equation in terms of different variables. Let $\omega C = A/z$ where A is the device area. The parameter $z$ is the capacitive impedance times unit area ($z = W_\mathrm{C}/2\pi f \varepsilon \approx 5.75 \cdot 10^{-6}\,\Omega\mathrm{cm}^2$ at $300\,\mathrm{GHz}$). Also, assuming that the series resistance is entirely defined by the contact resistances on cathode and anode, $R_\mathrm{s} = \rho_\mathrm{c}/A_\mathrm{c} + \rho_\mathrm{a}/A$ with $\rho_\mathrm{c}$ and $\rho_\mathrm{a}$ the specific contact resistivities of cathode and anode, and $A_\mathrm{c}$ the area of the cathode contact. Equation 4.2 then takes the form

$$P_\mathrm{RF} = \frac{1}{2} R_\mathrm{L} I^2 \frac{1}{1 + \left(\frac{R_\mathrm{L} A}{z} + \frac{\rho_\mathrm{c}}{z}\frac{A}{A_\mathrm{c}} + \frac{\rho_\mathrm{a}}{z}\right)^2}. \tag{4.3}$$

The cathode contact resistivity has a noticeable influence on the RF power only if the term $\rho_\mathrm{c} A/z A_\mathrm{c}$ is not negligible compared with 1, $R_\mathrm{L} A/z$, and $\rho_\mathrm{a}/z$. In the following, it is assumed

that the anode contact resistance is small and it is omitted. As $R_\mathrm{L}A/z$ varies from $\approx 3.1$ to $\approx 0.78$ for $A = (6\,\mu\mathrm{m})^2$ to $(3\,\mu\mathrm{m})^2$, the cathode contact resistivity has an influence if it is on the order of $z$ or larger, that is $\rho_\mathrm{c} \gtrsim 1 \cdot 10^{-6}\,\Omega\mathrm{cm}^2$. This is a typical value for contact resistivities between metals and semiconductors [10].

It is also interesting that for larger devices, the term $R_\mathrm{L}A/z$ becomes more important, and the influence of the contact resistivity is smaller, which is what was observed in table 4.4. Of the $6\,\mu$m devices, those with Au contacts (B6, C6, G6) all have the same $r$, higher than those with Pt/Au metallization (A6, H6). The B6 device has a smaller surface covered with Au than C6 and G6 devices. However, the contact resistivity of the Au–InGaAs contact is low enough that no difference is discernible for these large devices.

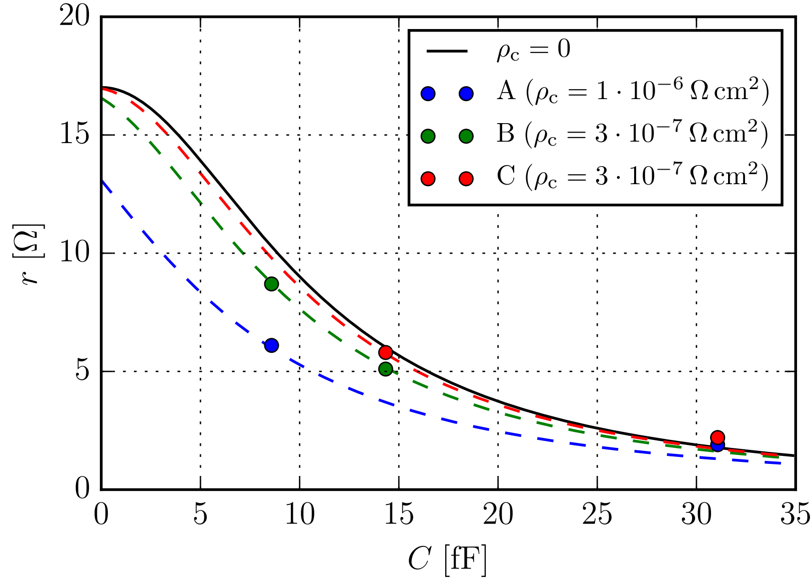


Figure 4.24: Measured values of $r$ at 300 GHz in dependence of the device capacitance, and model calculations. The black curve shows the ideal behavior without series resistance. The curves for B and C type devices are calculated with the same contact resistivity, but with $A_\mathrm{c}/A = 0.3$ for B type devices, and $A_\mathrm{c}/A = 1$ for C type devices.

The absorption region and transport region time constants can be included in equation 4.3 by replacing $I^2 = I_\mathrm{dc}^2 \frac{1}{1+(2\pi f \tau_\mathrm{a})^2} \left(\frac{\sin(\pi f \tau_\mathrm{tr})}{\pi f \tau_\mathrm{tr}}\right)^2$. From this model, expected values of $r$ depending on the cathode contact resistivity can be calculated. Figure 4.24 shows the expected dependence of $r(C)$ and the measured values of the A, B, and C type devices. Reasonably good agreement for the $3\,\mu$m and $4\,\mu$m devices is reached by assuming $\rho_\mathrm{c} = 1 \cdot 10^{-6}\,\Omega\mathrm{cm}^2$ for the Pt–InGaAs contact of the A type devices, and $\rho_\mathrm{c} = 3 \cdot 10^{-7}\,\Omega\mathrm{cm}^2$ for the Au–InGaAs contact of the B and C type devices. The model does not correctly predict

the values of the 6 $\mu$m devices: the predicted values of $r$ are 1.7 Ω and 1.6 Ω for 6 $\mu$m C and B-type devices, (measured: 2.2 Ω), and 1.4 Ω for the A type device (measured: 1.9 Ω). In fact, the capacitive roll-off alone, $\frac{R_L}{2}\frac{1}{1+(\omega R_L C)^2} \approx 2.56\,\Omega$ already predicts values close to those measured, without considering the absorption and transit region roll-offs. The reason for the discrepancy for the 6 $\mu$m devices is currently not known.

However, the relative values of the $r$ parameter of the 6 $\mu$m devices are correctly given by the model: A6 and H6 have the same type of metallization, and the contact area of these devices can be calculated from the mask: $A_{c,A6} \approx 11.9\,\mu m^2$ and $A_{c,H6} \approx 5.8\,\mu m^2$. From equation 4.3, a ratio of $\frac{r_{A6}}{r_{H6}} \approx 1.31$ is calculated for $\rho_c = 1 \cdot 10^{-6}\,\Omega cm^2$, which is close to the measured ratio of $1.9\,\Omega/1.4\,\Omega \approx 1.36$.

From table 4.4 it can be observed that the parameter $r$ is smaller for the devices in field 1,3 than for the other devices. This indicates that a smaller fraction of the dc current is modulated. However, the additional current due to the higher responsivity is partially modulated, as $rR^2$ is larger for the B3 device in field 1,3 than for the other measured B3 device.

Figure 4.22 also shows the generated RF power for large optical input powers. Saturation occurs at high $P_{opt}$, and the measured power at high injection does not follow the small-signal parabola. The saturation effect is more pronounced than would be expected by assuming that the additional photocurrent, above the linear extrapolation of the small signal responsivity, is not modulated. The dominating saturation mechanism is therefore space charge screening in the transport region, induced by the high currents [15]. This effect is also known as Kirk effect in bipolar junction transistors [16]. Saturation starts when the mobile charge carrier density in the transit region is comparable to the doping density.

The saturation current can be increased by n-doping the transit region. In InGaAs–InP UTC photodiodes, donor concentrations between $1 \cdot 10^{16}\,cm^{-3}$ and $5 \cdot 10^{16}\,cm^{-3}$ are typically used [17, 18], as this corresponds to the mobile charge carrier concentrations at the maximum current densities achievable. The transport properties mobility and overshoot velocity are almost unchanged in InP for doping concentrations below $1 \cdot 10^{17}\,cm^{-3}$ [17].

Another consequence of the space charge screening can be observed from the dependence of $P_{RF}$ on the bias voltage $U$, shown in figure 4.25. Initially, $P_{RF}$ increases with increasing voltage, reaching a maximum before declining again. This is due to velocity overshoot in the transport region, which increases the drift velocity of the electrons above the saturation velocity in a certain range of the electric field strength. Space charge screening of the electric field causes the optimum bias to shift to higher voltages at higher optical powers. The plot to the right in figure 4.25 shows that the optimum bias is $\approx -1\,V$ for a photocurrent of

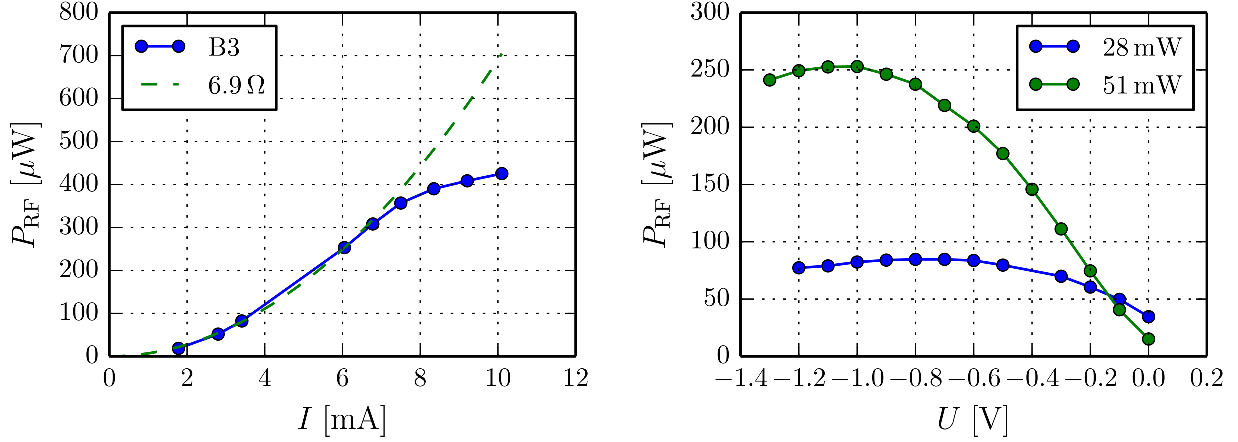


Figure 4.25: Dependence of the RF power at 300 GHz of the B3 device in field 1,3: left: dependence on photocurrent at −1 V, right: dependence on bias voltage at two different optical powers $P_{opt}$, corresponding to photocurrents of 3.4 mA and 6.1 mA.

6.1 mA in the B3 device. This is also the photocurrent starting at which saturation can be observed in the left plot, which shows the RF power at −1 V, because space charge screening would necessitate higher bias voltages for optimal operation at the higher photocurrents.

The highest output power that was measured at 300 GHz was obtained from the B3 device shown in figure 4.22. At a bias of −1 V and $P_{opt} = 91$ mW, $P_{RF} = 647\,\mu$W was measured at a photocurrent of 9.5 mA. The optical power corresponds to the highest available in the experiment, limited by the EDFA. Slightly higher optical powers could be generated, but due to the high reflectance of the Au covered wafer, part of the laser power was reflected back into the fiber and caused additional lines, apart from the two laser frequencies, to appear in the EDFA output spectrum. The inclusion of an additional optical isolator in the setup should solve this problem, but would make a more powerful amplifier necessary for the same optical output powers. Due to the limitation in $P_{opt}$, the bias voltage was increased instead. The maximum power was obtained at $U = -1.2$ V, at which point $P_{RF} = 692\,\mu$W was measured, see figure 4.26. The device remained stable for several 10s of seconds at this optical power and bias before a degradation of the RF power was noticed. The same degradation was noticed in other devices shortly before failure, and is followed by a reduction in responsivity before complete destruction, at which point the device behaves essentially like a short-circuit.

The frequency dependence of the RF power is plotted in figure 4.27 for the frequency range of the WR-3 band. The average roll-off in this frequency region is obtained from a fit, and

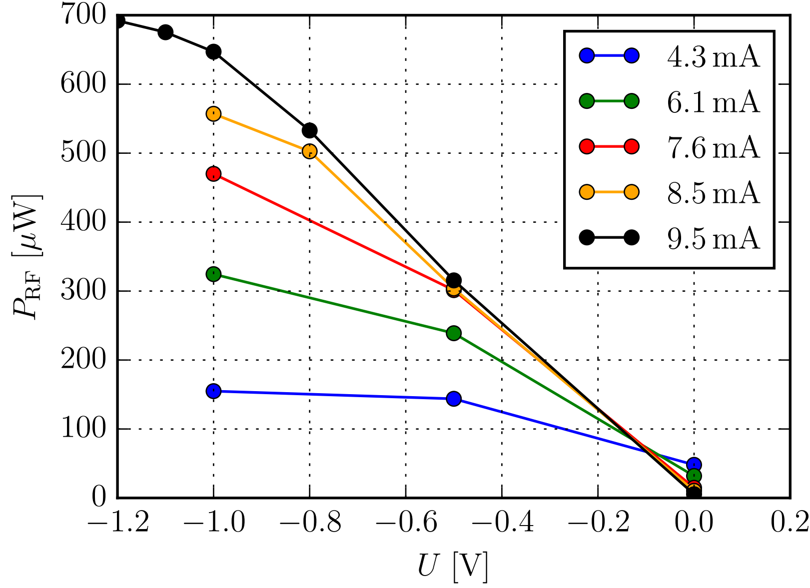


Figure 4.26: RF power at 300 GHz generated by a B3 type device at several photocurrents. The highest output power, $P_{RF} = 692\,\mu W$ at $U = -1.2\,V$, $I = 9.5\,mA$ and $P_{opt} = 91\,mW$, was measured shortly before device destruction.

is between ≈ 11.5 dB per decade for the 3 μm devices and ≈ 23 dB per decade for the 6 μm devices. Calculating the expected roll-off from equations 1.18 and 1.19 using the estimated time constants $\tau_a = 0.32\,ps$, $\tau_{tr} = 0.5\,ps$, and $\tau_{RC} = R_L C$, yields average roll-offs in the WR-3 band of 22.9 dB/dec, 17.3 dB/dec, and 12.4 dB/dec for 6 μm, 4 μm, and 3 μm devices. These values are close to those measured, and show that the devices behave as expected from the basic model for broad-band UTC photodiodes. Of the calculated frequency roll-off, 5.7 dB/dec is from the electron transport time constants $\tau_a$ and $\tau_{tr}$. This shows that even for the 3 μm devices, the RC time constant is dominating in this frequency range.

Due to the good agreement between measured frequency roll-off and the expected one in the measured frequency range, the frequency dependence of the RF power can be extrapolated to a larger frequency range. In particular, the 3 dB frequency can be estimated: it is approximately 98, 196, and 260 GHz for 6, 4, and 3 μm devices.

### 4.2.4 Comparison with the state of the art and outlook

The measured responsivities of the best (B type) devices are comparable to those obtained on vertically integrated LTG-GaAs photoconductors (140 mA/W for a 6 μm diameter device) [8]. Significantly higher responsivities are obtained by optical waveguide coupled de-

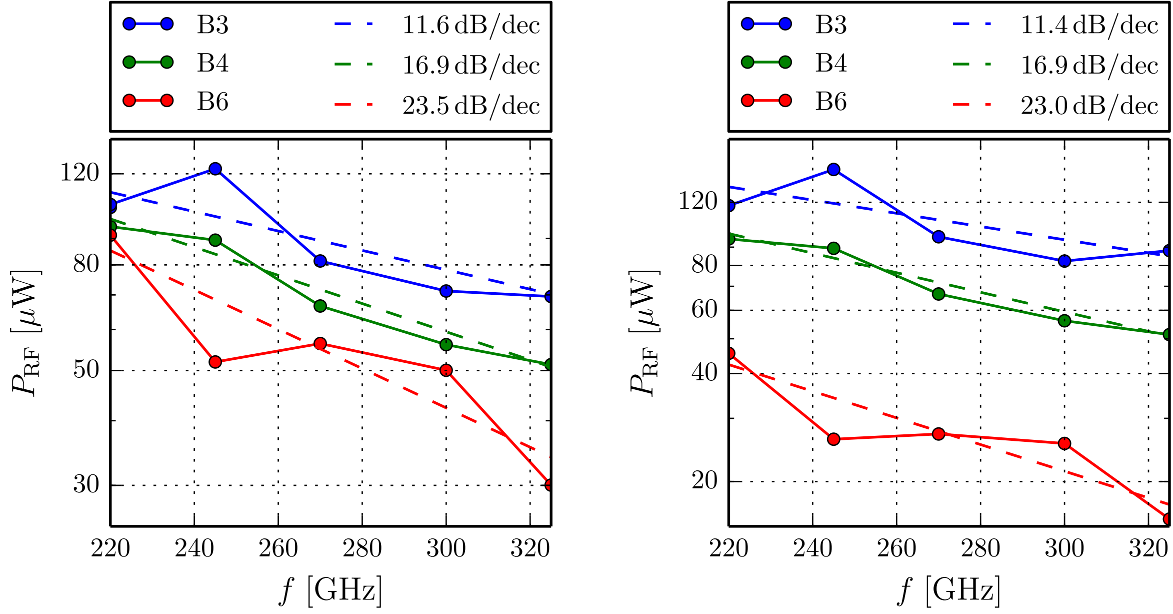


Figure 4.27: RF power generated at $U = -1$ V in small-signal mode in the WR-3 band. Left image: $P_{\mathrm{opt}} = 28.8$ mW (Photocurrents of 3.0 mA, 3.4 mA, and 4.6 mA for the B3, B4, and B6 device). Right image: $I = 3.4$ mA. The B4 device is the same in both images, the curves for the B6 and B3 types have been measured on different devices. The B3 device in the right image is in field 1,3.

vices (530 mA/W [19]), by side illuminated devices using a 45° mirror (210 mA/W [20]) and by devices with thicker absorption regions working at lower frequencies (550 mA/W for a device with 600 nm absorption layer and a bandwidth of 29 GHz [21]). However, the responsivities are higher than that of some other high-power vertically illuminated UTCs [22].

The maximum measured output power of 692 $\mu$W at 300 GHz is very close to that obtained with near-ballistic UTC photodiodes flip-chip bonded to AlN substrate, which have also been characterized by on-wafer measurements [22], and is the highest ever reported for broadband devices in this frequency range.

Due to the vertical structure with thick anode metallization and efficient charge extraction in the cathode without series resistance due to transport in the InGaAs contact layer, the diodes presented here show the highest efficiency of broad band photomixers around 300 GHz ever reported. The THz figure of merit, $S = P_{\mathrm{RF}}/P_{\mathrm{opt}}^2$, is slightly higher than the best values obtained by traveling-wave UTC photodiodes with efficient waveguide coupling of the optical power. The optical efficiency $\eta_{\mathrm{opt}} = P_{\mathrm{RF}}/P_{\mathrm{opt}}$ is improved by more than a factor of 2.5, and thanks to the low bias voltage and low current, the total efficiency $\eta_{\mathrm{tot}} = P_{\mathrm{RF}}/(P_{\mathrm{opt}} + P_{\mathrm{el}})$ is improved by a factor of 2.8. Table 4.5 lists the broadband photomixers from table 1.1

together with the figures of merit of the best device (B3) measured in this work.

| Device | $P_{\mathrm{RF}}$ [$\mu$W] | $R$ [A/W] | $\eta_{\mathrm{opt}}$ [%] | $\eta_{\mathrm{tot}}$ [%] | $S$ [1/W] |
|---|---|---|---|---|---|
| UCL TW-UTC (300 GHz) [19] | 110 | **0.31** | *0.28* | *0.13* | *0.069* |
| IEMN UTC (300 GHz) [1] | 400 | 0.046 | 0.2 | 0.18 | *0.01* |
| IEMN vertical PC (288 GHz) [23] | **650** | 0.07 | 0.29 | 0.24 | 0.0128 |
| NCU NB-UTC (325 GHz) [22] | **661** | 0.015 | *0.062* | *0.06* | *0.00058* |
| IEMN this work (300 GHz) | **692** | 0.10 | **0.76** | **0.67** | **0.083** |

Table 4.5: Comparison of figures of merit of wide-band continuous wave photomixers working around 300 GHz. Entries in italics are not given directly in the publication, but have been calculated from the published data. The highest value of each figure of merit is in bold characters. The TW-UTC is the only device integrated with an antenna, all other devices are characterized by on-wafer measurements. TW-UTC: traveling-wave UTC, PC: photoconductor, NB-UTC: near-ballistic UTC.

The UTC photodiodes transferred to Si substrate with semitransparent cathode contact presented here are a first demonstration of the concept. Even though the devices already compare favorably to the state of the art, some improvements can still be envisaged.

Due to the higher responsivity of the devices compared to non-transferred devices without metallic mirror, a thinner absorption region could be employed in future devices while still maintaining a reasonable responsivity. The overall effects of a thinner absorption region are difficult to assess: The frequency roll-off is not yet very pronounced at 300 GHz, with a factor of 0.73 estimated for the present 150 nm region, but might be improved to about 0.86 with a 100 nm thick absorption region. Also, the power handling capabilities of the device should be increased, due to a thinner InGaAs region with low thermal conductivity. On the other hand, a larger fraction of the optical power would be absorbed in the contacts, making better heat-sinking capabilities necessary for the same photocurrents.

The In–Au bonding layer has a lower effective thermal conductance than the Au mirror and the Si substrate. By increasing the Au mirror height from 75 nm to 300 nm or more, the heat could be better dissipated laterally, reducing the total thermal resistance of the device. The second main factor limiting heat transfer is the low thermal conductance of the InGaAs absorption layer, which is located between the substrate and the transport layer, in which the electrical power is dissipated. Growing the epitaxy in inversed order would put the transport layer in contact with the heat-spreading metallic mirror, and result in a large improvement of the heat-sinking capabilities of the devices.

Even for the smallest diodes, the RC cut-off frequency is the lowest and the dominant one

in the measured frequency range. A thicker collector layer would reduce the capacitance at the cost of a longer transit time $\tau_{\mathrm{tr}}$. From the frequency roll-offs $\gamma_{\mathrm{tr}} = \left(\frac{\sin(\pi f \tau_{\mathrm{tr}})}{\pi f \tau_{\mathrm{tr}}}\right)^2$ and $\gamma_{\mathrm{RC}} = 1/(1 + (2\pi f \tau_{\mathrm{RC}})^2)$ associated to the time constants $\tau_{\mathrm{tr}}$ and $\tau_{\mathrm{RC}}$, it is expected that at 300 GHz for a 3 $\mu$m device, $\gamma_{\mathrm{tr}}\gamma_{\mathrm{RC}} \approx 0.56$ for the present devices, which would increase by more than 10% to $\gamma_{\mathrm{tr}}\gamma_{\mathrm{RC}} \approx 0.63$ for a 50 nm thicker transport layer.

A saturation of the RF power can be observed at high photocurrents (figure 4.22). As already mentioned, a light transport region doping in the order of $n = 1 \cdot 10^{16}\,\mathrm{cm}^{-3}$ is expected to reduce the saturation due to the space charges. Ideally, if the saturation could be completely avoided, output powers of 785 $\mu$W at bias of $-1$ V would be expected from the B3 device at 300 GHz.

In the transferred diodes, the Au on InGaAs anode contact has proven to be stable over the period of 9 months between the flip-chip bonding of the diode epitaxy and the characterization of the devices, despite the diffusion expected to be taking place between Au and InGaAs. Comparison of the different cathode contacts has shown that the cathode contact resistance still limits the output power, and the model has shown good agreement when neglecting the anode contact resistance. Therefore, the cathode contact should be optimized, possibly by replacing the Pt contact of the A type devices with Ti or Mo. Specific contact resistances below $1 \cdot 10^{-7}\,\Omega\mathrm{cm}^2$ have been obtained by Ti/Pt/Au contacts on highly doped n-InGaAs [24], although the contact did not remain stable above 400 °C. Very low resistance and thermally stable contacts ($1.3 \cdot 10^{-8}\,\Omega\mathrm{cm}^2$) have been obtained by depositing Mo directly in the same vacuum cycle as material growth by MBE, to avoid any surface contamination [25, 26]. Deposition in the same vacuum cycle as material growth is not possible for the flip-chip bonded devices, but Mo is still an interesting candidate as contact metal due to its thermal stability and work function ($\sim 4.6$ eV) close to the electron affinity ($\sim 4.5$ eV) of InGaAs [26]. Very low contact resistances of non-alloyed contacts to n-InGaAs ($1.7 \cdot 10^{-8}\,\Omega\mathrm{cm}^2$) have also been shown using an n-InAs contact layer [27]. However, such a contact layer would be absorbing at 1.55 $\mu$m wavelength, and would therefore have to be very thin.

Further improvements could potentially be made by the geometric design of the cathode metallization. The slit structure employed currently has been obtained by optimizing the transmittance of an infinite surface of such slits. Simulations have shown that for the small devices with only 3 metal strips, the contact behaves differently than the infinite surface [1]. An improved design would maximize the absorption in the absorption layer instead of maximizing the transmittance of the contact, and would take into account the finite dimensions of the contact. However, this is difficult as analytic calculations would

become very complex, and design by simulation alone is time consuming and difficult to verify until after device fabrication.

Finally, if all of the proposed improvements (thicker transit layer, collector doping to avoid space charge effects, ultra-low cathode contact resistance) can be combined, ideally just over 1 mW RF power is expected at 300 GHz from a wideband device. This demonstrates the potential of the presented UTC photodiode structure.

## 4.3 Summary

In this chapter, two types of high efficiency UTC photodiodes have been presented. Double-collector UTC photodiodes for high frequency operation have been fabricated. The devices have not yet been characterized due to difficulties in the measurement setup with coplanar probes on the front side of the wafer and illumination from the back side.

UTC photodiodes flip chip wafer bonded to a Si substrate and exploiting a semitransparent top contact recently developed in the THz photonics group of the IEMN have been designed and fabricated. Characterization through on-wafer measurement in the WR3.4 band (220–325 GHz) has been performed, and state of the art maximum output powers close to 700 $\mu$W at 300 GHz have been reached, while simultaneously achieving the highest efficiency ever reported for photomixers in this frequency range, making this device very interesting for high-data-rate communication systems or mobile spectroscopy systems in the sub-THz range.

Several improvements for future devices are suggested, such as a thicker transport region to reduce the capacitance, and doping of the transport layer to avoid saturation due to space charge effects. It has also been shown that a cathode contact with lower contact resistivity should improve the output power of the device. If all these improvements can be implemented successfully, an RF power of 1 mW at 300 GHz could be achievable from a single device in broadband configuration. More than 1 mW output power is also expected from narrow-band devices with an impedance matching circuit.

# Bibliography


[1] F. Pavanello, *Uni-travelling carrier photodiodes and metal mesh filters based on sub-wavelength apertures for THz applications*, PhD thesis, Université Lille 1 (2013)

[2] M. Achouche, M. Chtioui, *A double-collector uni-travelling-carrier photodiode,* European patent application EP 2 466 649 A1 (2010)

[3] D. Streit, R. Lai, A. Gutierrez-Aitken, M. Siddiqui, B. Allen, A. Chau, W. Beale, A. Oki, *InP and GaAs components for 40 Gbps applications*, in *Gallium Arsenide Integrated Circuit (GaAs IC) Symposium, 2001. 23rd Annual Technical Digest*, 247–250 (2001)

[4] T. Shi, B. Xionig, C. Sun, Y. Luo, *Back-to-Back UTC-PDs with high responsivity, high saturation current and wide bandwidth*, IEEE Photonics Technology Letters **25**, 136 (2013)

[5] A. Beck, G. Ducournau, M. Zaknoune, E. Peytavit, T. Akalin, J.-F. Lampin, F. Mollot, F. Hindle, C. Yang, G. Mouret, *High-efficiency uni-travelling-carrier photomixer at 1.55 $\mu$m and spectroscopy application up to 1.4 THz*, Electronics Letters **44**, 1320 (2008)

[6] M. Zaknoune, E. Mairiaux, Y. Roelens, N. Waldhoff, U. Rouchy, P. Frijlink, M. Rocchi, H. Maher, *480-GHz $f_{\mathrm{max}}$ in InP/GaAsSb/InP DHBT With New Base Isolation $\mu$-Airbridge Design*, IEEE Electron Device Letters **33**, 1381 (2012)

[7] E. Peytavit, S. Lepilliet, F. Hindle, C. Coinon, T. Akalin, G. Ducournau, G. Mouret, J.-F. Lampin, *Milliwatt-level output power in the sub-terahertz range generated by photomixing in a GaAs photoconductor*, Appl. Phys. Lett. **99**, 223508 (2011)

[8] E. Peytavit, P. Latzel, F. Pavanello, G. Ducournau, J.-F. Lampin, *CW Source Based on Photomixing With Output Power Reaching 1.8 mW at 250 GHz*, IEEE electron device letters **34**, 1277 (2013)

[9] A. Beck, *Réalisation et caractérisation de photodiodes à transport unipolaire pour la génération d'ondes térahertz*, PhD thesis, Université Lille 1 (2008)

[10] S. Sze, *Semiconductor device physics* (Wiley, 2002)

[11] J. Vandenberg, H. Temkin, R. Hamm, M. DiGiuseppe, *Structural study of alloyed gold metallization contacts on InGaAsP/InP layers*, Journal of applied physics **53**, 7385 (1982)

[12] J. Vandenberg, H. Temkin, *An in situ x-ray study of gold/barrier-metal interactions with InGaAsP/lnP layers*, Journal of Applied Physics **55**, 3676 (1984)

[13] E. Peytavit, J.-F. Lampin, F. Hindle, C. Yang, G. Mouret, *Wide-band continuous-wave terahertz source with a vertically integrated photomixer*, Appl. Phys. Lett. **95**, 161102 (2009)

[14] E. Peytavit, C. Coinon, J.-F. Lampin, *A metal-metal Fabry-Pérot cavity photoconductor for efficient GaAs terahertz photomixers*, Journal of Applied Physics **109**, 016101 (2011)

[15] H. Ito, S. Kodama, Y. Muramoto, T. Furuta, T. Nagatsuma, T. Ishibashi, *High-Speed and High-output InP-InGaAs Unitraveling-Carrier Photodiodes*, IEEE Journal of selected topics in quantum electronics **10**, 709 (2004)

[16] C. Kirk, *A theory of transistor cutoff frequency ($f_T$) falloff at high current densities*, IRE transactions on Electron Devices **9**, 164 (1962)

[17] N. Li, X. Li, S. Demiguel, X. Zheng, J. Campbell, D. Tulchinsky, K. Williams, T. Isshiki, G. Kinsey, R. Sudharsansan, *High-Saturation-current charge-compensated InGaAs-InP Uni-traveling-carrier photodiode*, IEEE Photonics Technology Letters **16**, 864 (2004)

[18] T. Ishibashi, T. Furuta, H. Fushimi, S. Kodama, H. Ito, T. Nagatsuma, N. Shimizu, Y. Miyamoto, *InP/InGaAs Uni-Traveling-Carrier Photodiodes*, IEICE Trans. Electron. **E83-C**, 938 (2000)

[19] E. Rouvalis, C. C. Renaud, D. Moodie, M. Robertson, A. J. Seeds, *Continuous wave Terahertz Generation from Ultra-fast InP-based Photodiodes*, IEEE Transactions on microwave theory and techniques **60**, 509 (2012)

[20] H. Ito, T. Yoshimatsu, H. Yamamoto, T. Ishibashi, *Widely Frequency Tunable Terahertz-Wave Emitter Integrating Uni-Traveling-Carrier Photodiode and Extended Bowtie Antenna*, Applied physics express **6**, 064101 (2013)

[21] M. Chtioui, A. Enard, D. Carpentier, S. Bernard, B. Rousseau, F. Lelarge, F. Pommereau, M. Achouche, *High-Performance Uni-Traveling-Carrier Photodiodes With a New Collector Design*, IEEE Photonics Technology Letters **20**, 1163 (2008)

[22] J-W Shi, J-M Wun, F-W Lin, J. Bowers, *Ultra-Fast (325GHz) near-ballistic uni-*

*traveling-carrier photodiodes with high sub-THz output power under a 50 Ω load*, in *IEEE Photonics Conference* (2013)

[23] E. Peytavit, *private communication*

[24] T. Nittono, H. Ito, O. Nakajima, T. Ishibashi, *Non-alloyed ohmic contacts to n-GaAs using compositionally graded* $\mathrm{In_xGa_{1-x}As}$ *layers*, Japanese Journal of Applied Physics **27**, 1718 (1988)

[25] U. Singisetti, M. Wistey, J. Zimmerman, B. Thibeault, M. Rodwell, A. Gossard, S. Bank, *Ultralow resistance in situ Ohmic contacts to InGaAs/InP*, Applied Physics Letters **93**, 183502 (2008)

[26] A. Baraskar, M. Wistey, V. Jain, U. Singisetti, G. Burek, B. Thibeault, Y. Lee, A. Gossard, M. Rodwell, *Ultralow resistance, nonalloyed Ohmic contacts to n-InGaAs*, Journal of Vacuum Science & Technology B **27**, 2036 (2009)

[27] G. Stareev, H. Künzel, *Tunneling behaviour of extremely low resistance nonalloyed Ti/Pt/Au contacts to n(p)-InGaAs and n-InAs/InGaAs*, Journal of applied physics **74**, 7592 (1993)

# Conclusion and perspectives

In this thesis, a low temperature metallic wafer bonding process based on indium has been developed and optimized, and its application for high efficiency THz photomixers has been investigated. Increasing the efficiency of photomixers allows to employ lower power lasers and voltage sources, reducing the cooling requirement of THz emitter systems and the wall-plug power consumption. This is interesting especially for widespread application outside of the laboratory, such as wireless THz communication and spectroscopic systems.

Low temperature wafer bonding is useful for transferring epitaxial layers to a substrate with higher thermal conductivity than the growth substrate, which potentially increases the output power of photomixers before thermal failure. The low temperature of the bonding process avoids diffusion between metals and semiconductors and of dopants in the epitaxy, and reduces wafer bowing due to different coefficients of thermal expansion of the substrates. Bonding based on indium has been investigated as indium seems particularly suitable due to its softness at room temperature and its low melting point.

It has been shown that In–In wafer bonding can be performed at room temperature through the application of uniform pressure. However, bonds purely made from indium are not thermally stable above 156 °C and are etched by acids used for wet etching of the InP/InGaAs material system, limiting the possible fabrication steps after bonding. Therefore, solid-liquid interdiffusion bonding using the In–Au system has been investigated. The bonding parameters have been optimized, and good quality bonds have been obtained at bonding temperatures as low as 180 °C. The main factors important for good quality bonding using the In–Au system are the composition of the bond, indium evaporation speed, and the bonding temperature.

Characterization of the thermal conductance of various In–Au bonds has been performed in a configuration similar to that of vertical photoconductors. Metallic strips on a thin LTG-GaAs layer transferred to a high conductivity substrate such as silicon or diamond coated silicon have been heated electrically, and the temperature has been measured using an infrared camera. The thermal resistance associated to the bonding layer and the contact resistance was found to be lower than that of similar bonds reported in the literature.

The feasibility of vertical photoconductors based on Fe-implanted $In_{0.53}Ga_{0.47}As$ using the wafer bonding technique has been explored. The advantage of a vertical photoconductor is that only a thin active layer is necessary for a high responsivity. Moreover, the implantation profile can be more homogeneous in a thin layer ($\sim$ 150 nm) than in the thicker layers used for planar interdigitated finger photoconductors ($> 1\,\mu$m). Lifetime measurements of $In_{0.53}Ga_{0.47}As$ samples implanted with Fe at different concentrations using a pump-probe setup showed that sub-picosecond lifetimes suitable for THz generation have been achieved. However, the dark resistivity of the samples ($< 1\,\Omega$cm) was too low for efficient photomixer operation. The attention was instead focused on uni-traveling-carrier (UTC) photodiodes.

The fabrication of double-collector UTC photodiodes using the InP/InGaAs material system has been presented. A self-alignment process was used to place the anode contact close to the etched diode without causing a short circuit. The devices are designed for on-wafer measurements and backside illumination, which makes the characterization setup complicated. The characterization of these devices has been delayed due to experimental difficulties, but is foreseen for the near future.

The In–Au bonding developed in this thesis has been combined with a semitransparent top contact from a previous thesis in the THz photonics group to fabricate UTC photodiodes on a silicon substrate and allow on-wafer characterization using front-side illumination. Different cathode contact geometries and metallizations have been compared. The responsivity has been doubled compared to the non-transferred devices of the previous thesis, thanks to the mirror included with the metallic bonding layer. Responsivities of 0.10 A/W have been reached for $3\,\mu$m devices, and 0.16 A/W for diodes with $6\,\mu$m sidelength.

The best devices, which exploit extraordinary transmission of the semitransparent contact to simultaneously achieve low contact and series resistance and high transmission of the laser signal, have shown high output powers and very high efficiencies. State of the art output power for broadband photomixers, reaching $692\,\mu$W at 300 GHz at a bias of $-1.2$ V and a photocurrent of 9.5 mA, has been achieved. The optical efficiency $\eta_{\text{opt}} = 0.76\%$ and total efficiency $\eta_{\text{tot}} = 0.67\%$ present an improvement of the state of the art by a factor of 2.5 and 2.8, respectively. The state of the art performance of this first demonstrator shows the potential of the new photodiode structure. Moreover, the top illuminated devices need no anti-reflection coating, and are easier to fabricate in large quantities than side illuminated devices such as refracting facet or waveguide fed photodiodes and avoid the necessity of backside polishing and possibly wafer thinning of backside illuminated devices.

Potential improvements for future devices are discussed, such as a thicker transport layer, doping of the transport layer, and lower cathode contact resistance. Antenna integration

for free space applications and device characterization above 325 GHz as well as impedance matching to optimize performance around a frequency of interest are possible topics for future photodiodes. Also, packaging of the photomixer with aligned fiber, antenna and possibly silicon lens in a module would be useful for applications like spectroscopy and data transmission, especially outside of the laboratory environment.